BRNO UNIVERSITY OF TECHNOLOGY

Faculty of Mechanical Engineering

MASTER'S THESIS

Brno, 2023   Bc. Pavel Klok

BRNO UNIVERSITY OF TECHNOLOGY

VYSOKÉ UČENÍ TECHNICKÉ V BRNĚ

FACULTY OF MECHANICAL ENGINEERING

FAKULTA STROJNÍHO INŽENÝRSTVÍ

INSTITUTE OF PHYSICAL ENGINEERING

ÚSTAV FYZIKÁLNÍHO INŽENÝRSTVÍ

NEAR-FIELD EXCITED PHOTOLUMINESCENCE MAPPING

MAPOVÁNÍ FOTOLUMINISCENCE EXCITOVANÉ V BLÍZKÉM POLI

MASTER'S THESIS
DIPLOMOVÁ PRÁCE

AUTHOR   Bc. Pavel Klok
AUTOR PRÁCE

SUPERVISOR   Ing. Petr Dvořák, Ph.D.
VEDOUCÍ PRÁCE

BRNO 2023

Assignment Master's Thesis

Institut:	Institute of Physical Engineering
Student:	**Bc. Pavel Klok**
Degree programm:	Physical Engineering and Nanotechnology
Branch:	no specialisation
Supervisor:	**Ing. Petr Dvořák, Ph.D.**
Academic year:	2022/23

As provided for by the Act No. 111/98 Coll. on higher education institutions and the BUT Study and Examination Regulations, the director of the Institute hereby assigns the following topic of Master's Thesis:

Near–field excited photoluminescence mapping

Brief Description:

Photoluminescence can be used to characterize the optoelectronic properties of advanced materials and nanostructures. For a better understanding of photoluminescence in nanostructures, it is useful to use microscopic methods with high lateral resolution, where we can study dynamic phenomena in addition to the kinematics of the intrinsic optoelectronic processes. Therefore, it is desirable to develop time–resolved photoluminescence spectroscopy excited by near–field scanning optical microscopy (SNOM).

Master's Thesis goals:

1) Conduct a research study on near–field excited photoluminescence mapping and time–resolved optical spectroscopy.
2) Assemble and verify the functionality of an experimental setup for near–field excited photoluminescence mapping.
3) Experimentally study near–field excited photoluminescence on advanced materials and nanostructures.
4) Attempt to measure near–field excited photoluminescence using time–resolved optical spectroscopy.

Recommended bibliography:

KUMAR, Challa. UV-VIS and Photoluminescence Spectroscopy for Nanomaterials Characterization. Berlin: Springer Berlin Heidelberg, 2013. ISBN 3642275931.

Deadline for submission Master's Thesis is given by the Schedule of the Academic year 2022/23

In Brno,

L. S.

_____   _____
prof. RNDr. Tomáš Šikola, CSc.   doc. Ing. Jiří Hlinka, Ph.D.
Director of the Institute   FME dean

ABSTRACT

This thesis explores the use of near-field (NF) excited photoluminescence (PL) mapping to investigate optoelectronic properties of advanced materials at the nanometer scale. By overcoming the limitations of traditional far-field optical techniques, it investigates phenomena on smaller length scales that would be previously inaccessible. The primary focus is on NF scanning optical microscopy, enabling the observation of subdiffraction phenomena for studied samples. A notable accomplishment of this thesis is the introduction of NF time-resolved PL mapping, a groundbreaking method for studying dynamic processes beyond the diffraction limit. Importantly, this approach represents a novel contribution to the field, as supported by the literature review presented in this thesis. Through meticulous evaluation and interpretation of PL measurements, this study enhances our understanding of the optical properties of lead halide perovskite materials and their potential applications, e.g. in solar cells. Moreover, it uncovers unexplored opportunities in NF time-resolved PL mapping, providing unprecedented insights into dynamic processes at the subdiffraction limit. By pushing the boundaries of nanoscale optical investigations, this diploma thesis establishes a good foundation for new research directions and advancements in the field.

KEYWORDS
near-field, photoluminescence, mapping, a-SNOM, TRPL, lead halide perovskite, pulsed laser

ABSTRAKT

Tato práce se zabývá mapováním fotoluminiscence (PL) pomocí buzení blízkého pole (NF), které slouží ke zkoumání optoelektronických vlastností pokročilých materiálů v nanometrovém měřítku. Díky překonání omezení tradičních optických technik v dalekém poli zkoumá jevy na menších rozměrech, které by jinak byly nedostupné. Hlavní důraz je kladen na NF rastrovací optickou mikroskopii, která umožňuje pozorování poddifrakčních jevů u studovaných vzorků. Významným přínosem této práce je zavedení časově rozlišitelného mapování PL v NF, tedy průlomové metody pro studium dynamických procesů pod hranicí difrakce. Tento přístup představuje nový přínos pro obor, což potvrzuje i přehled literatury uvedený v průběhu práce. Díky pečlivému vyhodnocení a interpretaci měření PL předložená práce rozšiřuje naše znalosti o optických vlastnostech olovnatých halogenidových perovskitů a jejich potenciálních aplikacích např. pro solární články. Dále odhaluje dosud neprozkoumané možnosti v oblasti časově rozlišitelného mapování PL v NF a poskytuje dosud nevídaný náhled do dynamických procesů pod difrakčním limitem. Posunutím hranic optického výzkumu na úrovni nanorozměrů vytváří tato diplomová práce solidní základ pro nové směry zkoumání v této oblasti.

KLÍČOVÁ SLOVA

blízké pole, fotoluminiscence, mapování, a-SNOM, TRPL, olovnaté halogenidové perovskity, pulzní laser

Author's Declaration

Author:	Bc. Pavel Klok
Author's ID:	208733
Paper type:	Master's Thesis
Academic year:	2023/24
Topic:	Near-field excited photoluminescence mapping

I declare that I have written this paper independently, under the guidance of the advisor and using exclusively the technical references and other sources of information cited in the paper and listed in the comprehensive bibliography at the end of the paper.

As the author, I furthermore declare that, with respect to the creation of this paper, I have not infringed any copyright or violated anyone's personal and/or ownership rights. In this context, I am fully aware of the consequences of breaking Regulation §11 of the Copyright Act No. 121/2000 Coll. of the Czech Republic, as amended, and of any breach of rights related to intellectual property or introduced within amendments to relevant Acts such as the Intellectual Property Act or the Criminal Code, Act No. 40/2009 Coll. of the Czech Republic, Section 2, Head VI, Part 4.

Brno ....
author's signature*

---

*The author signs only in the printed version.

Rád bych poděkoval svému vedoucímu Ing. Petru Dvořákovi, Ph.D. za odborné vedení práce a cenné rady a trpělivost v průběhu jejího vypracování. Jsem velmi rád za to, že už od bakalářského studiu jsem mohl pracovat pod tvým dohledem a vedením, jsi mi velkou inspirací a jsem velmi rád, že mám možnost s tebou spolupracovat i nadále.

Dále bych chtěl poděkovat hlavně Ing. Ondreji Černekovi, bez kterého by tato práce byla významně delší a bolestivější. Děkuji ti za pomoc na začátku při předání tipů a triků ohledně vyhotovení SNOM sond a následnou pomoc při napsání programu pro vyhodnocovní naměřených map. Také děkuji Ing. Mgr. Peterovi Kepičovi a Ing. Matouši Kratochvílovi, Ph.D. za poskytnutí vzorků. Moje další díky patří Ing. Zdeněku Nováčkovi, Ph.D., Bc. Janu Čecháčkovi, Ing. Martinu Konečnému, Ph.D. a Ing. Janu Novotnému, Ph.D. za celkovou pomoc při překonávání nástrah v průběhu měření. Za provedenou korekturu, rovněž konzultaci děkuji Ing. Petru Liškovi a prof. RNDr. Jiřímu Spoustovi, Ph.D., který má celkově největší podíl na mém akademickém vzdělání a zájmu. Velké díky patří celému Ústavu fyzikálního inženýrství, hlavně prof. RNDr. Tomáši Šikolovi, CSc. za rodinnou atmosféru a příjemné přátelské prostředí, které na celém ústavu panuje.

Velké díky patří Dannymu a Bei, v jejichž přítomnosti bylo psaní práce samá radost. V neposlední řadě děkuji mé rodině za poskytnuté zázemí a blizkým za všechnu nekončící podporu a trpělivost v průběhu celého studia. Největší díky patří mé přítelkyni Míši, která mi po dobu celého studia pomáhala a měla se mnou trpělivost i při velmi stresových situací. ChatGPT byl použit k uhlazení a korektuře textu, nikoliv k psaní textu, a sloužil pouze jako pomůcka při tvůrčím procesu.

Contents

Introduction

The understanding of materials has been significantly advanced through the application of optical characterization techniques, which provide valuable insights into their properties and behavior. Among these techniques, near-field (NF) excited photoluminescence (PL) mapping and time-resolved optical spectroscopy have emerged as powerful methods with exceptional spatial and temporal resolution. This diploma thesis aims to explore the potential of combining these techniques into a state-of-the-art setup and investigate their application to advanced materials and nanostructures.

To begin, Chapter 1 serves as an introduction to PL, a phenomenon where materials emit light after absorbing photons. PL measurements offer unique optical signatures that provide valuable information about the electronic dynamics and optical properties of diverse materials. However, traditional optical characterization techniques face a limitation known as the diffraction limit, which hinders the investigation of spatial variations in PL beyond a certain resolution, typically limited to half the wavelength used for imaging. To overcome this limitation, NF excited PL mapping employs a nanoscale light source scanned in close proximity to the sample, enabling precise probing of optical properties at the nanoscale. The advantages of the NF approach over conventional far-field methods will be discussed in detail in the last two sections of Chapter 2.

The objectives of this diploma thesis align with the overarching goals of conducting a research study on NF excited PL mapping and time-resolved optical spectroscopy. The first objective is to assemble and verify the functionality of an experimental setup specifically designed for NF excited PL mapping, as discussed in Chapter 3. By developing this setup, we can delve into the principles, methodologies, and various applications of this cutting-edge technique.

Our focus also extends to the experimental study of NF excited PL on advanced materials and nanostructures, particularly those with high quantum yield[1]. These materials possess unique optical properties that make them fascinating subjects for investigation. Our exploration encompasses the examination of spatial variations in PL at a resolution below the diffraction limit, including the study of carrier dynamics, exciton lifetime, and recombination processes. In doing so, we aim to unravel the underlying mechanisms governing photoluminescent behavior at the nanoscale and contribute to a comprehensive understanding of light-matter interactions in advanced materials.

A key aspect of this work involves the incorporation of time-resolved photoluminescence (TRPL) excited in the NF. By utilizing time-resolved measurements, we gain valuable information about the temporal processes of PL. Investigating exciton dynamics, emission lifetimes, and deactivation processes provides deeper insights into the fundamental aspects of light-matter interactions. Drawing upon the author's experience gained during the ERASMUS exchange, where TRPL of various perovskite materials was investigated, we further explore the dynamics of light-matter interactions in this thesis. The

---

[1]The number of photons emitted as a fraction of the number of photons absorbed.

PL lifetime, which is a characteristic of luminescent species, offers insights into excited state dynamics and can be influenced by the molecular environment. Hence, TRPL serves as a preferred tool for studying fast electronic deactivation processes. NF excited PL can be achieved using aperture-type scanning near-field optical microscopy (a-SNOM), which, when properly set up and fine-tuned, enables NF excited TRPL measurements.

The significance of this work lies in its contribution to the broader scientific community, particularly for the Institute of Physical Engineering (IPE). The development of an experimental setup for NF excited PL mapping, combined with time-resolved optical spectroscopy, represents a state-of-the-art method for investigating the optical properties of advanced materials. By unraveling the spatial and temporal aspects of PL, we enhance our understanding of material behavior at the nanoscale, paving the way for future advancements in nanoscale optical characterization.

In conclusion, this diploma thesis offers a comprehensive exploration of NF excited PL mapping and time-resolved optical spectroscopy. By addressing the fundamental objectives of this research study, we aim to expand the existing knowledge base in this field. Through the assembly of an experimental setup, experimental investigations, and analysis of time-resolved measurements, we strive to provide a holistic understanding of the optical properties and dynamics of advanced materials at the nanoscale.

1 Theoretical background

In this thesis, photoluminescence measurements are described in detail, and this chapter aims to provide the necessary theoretical background for understanding these measurements. The chapter begins with an overview of electromagnetic field theory, which is essential for understanding light-matter interactions. This section includes an explanation of polarization in linear and nonlinear dielectrics and the concept of light-matter interaction. The following section explores the electronic structures of multielectron atoms, including energy levels and transitions, which are critical to understanding the photoluminescence and nonlinear processes. Finally, the chapter concludes with a detailed discussion of photoluminescence, including the Jablonski diagram, which describes the excited states involved in the photoluminescence process. This theoretical background will serve as the foundation for the subsequent chapters that detail the experimental methods and results of the photoluminescence measurements.

1.1 Electromagnetic field theory

The electromagnetic field theory encompasses the phenomenon of light as an electromagnetic wave, following the same theoretical principles governing all types of electromagnetic radiation. The frequency of optical radiation lies within the electromagnetic spectrum range, which spans from infrared through visible to ultraviolet radiation. In this section, the most important concepts of the theory of electromagnetic fields are summarized, which were processed using literature [1–4].
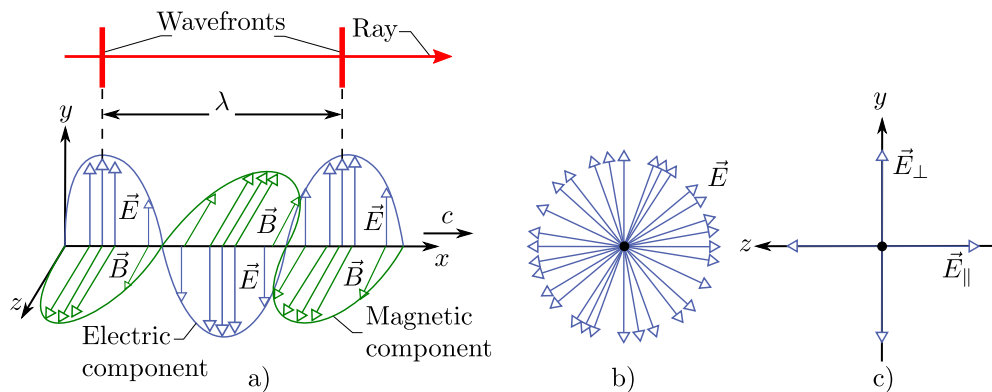

Fig. 1.1: Illustration of electromagnetic waves and polarization. a) An electromagnetic wave is depicted as a ray and two wavefronts separated by one wavelength λ. A "snapshot" of its electric field $\vec{E}$ and magnetic field $\vec{B}$ is shown along the x axis, along which the wave travels at speed c. b) Unpolarized light is represented as waves with randomly directed electric fields, all traveling along the same axis and with the same amplitude E. c) An alternative representation of unpolarized light shows that it is the superposition of two polarized waves whose planes of oscillation are perpendicular to each other [3].

Electromagnetic radiation is made up of two interdependent vector waves (shown in Figure 1.1a): the electric field wave and the magnetic field wave. The electric field wave, responsible for light polarization, determines the direction and orientation of polarization (which can be linear, circular, or elliptical). In general, light sources emit unpolarized electromagnetic waves (shown in Figure 1.1b) that rapidly and randomly change their polarization, meaning that the direction of the electric field at any point changes randomly, remaining perpendicular to the direction of wave propagation.

The fundamental interrelation between the electric and magnetic field is delineated by the Maxwell equations, a set of coupled partial differential equations that together with the Lorentz force law[1], form the foundation of classical electromagnetism and classical optics[2]. However, the behavior of these fields is strongly influenced by the properties of the medium through which electromagnetic radiation travels. When working with a material medium, two additional vector fields must be defined: electric induction ($\vec{D}$) and magnetic induction ($\vec{B}$) [4]. The Maxwell equations establish a relationship between four fields, namely $\vec{E}$ (electric intensity), $\vec{H}$ (magnetic intensity), $\vec{D}$, and $\vec{B}$ in the following manner:

$$\vec{\nabla} \cdot \vec{D} = \rho_{\text{f}}, \tag{1.1}$$

$$\vec{\nabla} \cdot \vec{B} = 0, \tag{1.2}$$

$$\vec{\nabla} \times \vec{E} = -\frac{\partial \vec{B}}{\partial t}, \tag{1.3}$$

$$\vec{\nabla} \times \vec{H} = \frac{\partial \vec{D}}{\partial t} + \vec{j}_{\text{f}}, \tag{1.4}$$

where ρ_{f} is volume density of free electric charge and $\vec{j}_{\text{f}}$ is current density of free currents. The use of hybrid notation, which includes both electric and magnetic field variables, is a common approach to describe these fields. However, this approach has the disadvantage of requiring appropriate constitutive relations to be included in order to express $\vec{D}$ and $\vec{H}$ in terms of $\vec{E}$ and $\vec{H}$. These constitutive relations depend on the nature of the material being considered. For linear, isotropic and homogeneous media, the constitutive relations are simple and well-known [2].

$$\vec{D} = \varepsilon_0 \vec{E} + \vec{P} = \varepsilon_0 \varepsilon_{\text{r}}(\omega)\, \vec{E}, \tag{1.5}$$

$$\vec{B} = \mu_0 \vec{H} + \mu_0 \vec{M} = \mu_0 \mu_{\text{r}}(\omega)\, \vec{H}. \tag{1.6}$$

The medium's relative permittivity and relative permeability are denoted as ε_{r} and μ_{r}, respectively. These values are related to the permittivity and permeability of vacuum,

---

[1]Charged particle experiences a force in the presence of an electric field and a magnetic field.

[2]Light as an electromagnetic wave according to classical laws like reflection, refraction, and diffraction.

represented by the constants ε_0 and μ_0, which correspond to the polarization vector $\vec{P}$ and magnetization vector $\vec{M}$, respectively. The speed of light in vacuum, given by $c = 1/\sqrt{\varepsilon_0 \mu_0}$, also serves as a crucial link between these constants.

1.1.1 Polarization in linear and nonlinear dielectrics

The behavior of materials under the influence of an electric field is essential to understand in optical applications, and polarization plays a vital role in this regard. The polarization vector, represented by $\vec{P}$, is defined as

$$\vec{P} = \varepsilon_0 \chi_e \vec{E}. \tag{1.7}$$

The electric susceptibility χ_e is a constant of proportionality that relates to the relative permittivity and refractive index of the material, given by

$$n^2 = 1 + \chi_e. \tag{1.8}$$

Materials that follow this relationship are known as linear dielectrics, which are insulators that can be polarized by an electric field. However, most dielectric media behave approximately linearly, unless exposed to high optical intensities, such as those produced by focused laser beams.
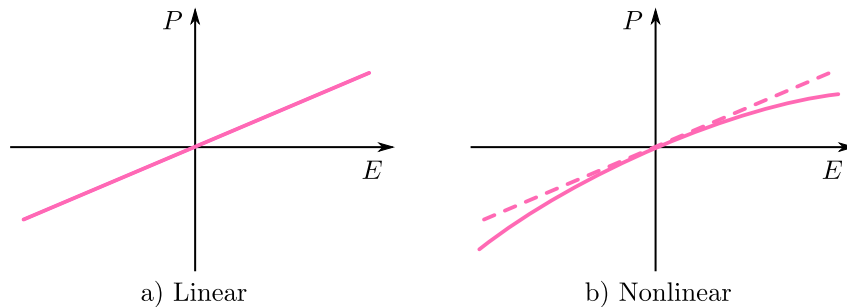

a) Linear   b) Nonlinear

Fig. 1.2: Illustration of the a) linear relationship between P and E in a dielectric medium and b) the nonlinear relationship between P and E. Taken from [4].

The linear effects of polarization are shown in Figure 1.2a. However, nonlinear dielectric media, shown in Figure 1.2b, exhibit a nonlinear relation between P and E, which may be of microscopic or macroscopic origin. Therefore, the function that relates P to E can be expanded as [4]

$$P = \varepsilon_0 \chi_e E + \varepsilon_0 \chi_e^{(2)} E^2. \tag{1.9}$$

The first term, which is linear, dominates at small E, while the second term represents a quadratic or second-order nonlinearity. Materials that exhibit this nonlinearity are called chi-two medium. The optical properties of a nonlinear medium are discussed in the

subsection 1.2.4, where the focus is on the second-order nonlinearity as nonlinearities of order higher than the second are negligible[3].

1.2 Light-matter interaction

Light-matter interaction is a fundamental concept that arises from the presence of electric charges within matter. When light passes through matter, the time-varying electric field of the light interacts with the electric charges and dipoles of atoms, molecules, and solids. This interaction is crucial to the understanding of electronic structure and the energy-level structures of matter. Systems of multiple particles obey a generalized form of an equation that provides the allowed values of the energy of the system, which can be discrete (as for an atom), continuous (as for a free particle), or comprise sets of densely packed discrete levels called bands (as for a semiconductor). The presence of thermal excitation or an external field, such as light illuminating the material, can induce the system to move from one of its energy levels to another, providing a means by which the system can exchange energy with the outside world. In certain cases, a photon can interact with an atom or ion if the energy of the photon matches the difference between two atomic energy levels, according to the rules of quantum mechanics that determine the allowed energy levels and energy bands of matter. During light-matter interaction, energy and momentum are transferred via photons. However, when light is in transit, we interpret the light wave as a probability wave, in which the probability (per unit time) that a photon can be detected is proportional to the amplitude of the oscillating electric field of the light wave at the detector. Some electromagnetic waves, including X rays, gamma rays, and visible light, are radiated (emitted) from sources that are of atomic or nuclear size, where quantum physics rules. In the following sections, we will explore the electronic structure and energy-level structures of selected atoms, ions, molecules, and solids, and their interaction with light [4, 6].

1.2.1 Electronic structures

Quantum mechanics concepts, such as matter waves, Schrödinger equation, and the wave function, are necessary to fully explain the electronic structure. To determine the matter wave of a moving particle in a region with potential energy, we utilize the Schrödinger equation. For example, a particle with mass m moving in the r direction with constant total energy E through a region with potential energy $U(r)$ can be described by a wave function $\psi(r)$, obtained by solving the simplified stationary Schrödinger equation:

$$\frac{d^2\psi}{dr^2} + \frac{8\pi^2 m}{h^2}[E - U(r)]\psi = 0. \tag{1.10}$$

---

[3]Third order nonlinearity has been the subject of extensive academic discussion and analysis in the literature, as stated in Khurgin's 2023 publication [5].

It is important to mention that the Schrödinger equation typically relies on the position vector, which results in three differential equations under rotational symmetry[4]. Specifically, two equations are dependent on angles while the other equation relies on the radial distance r.

The wave function characterizes the matter wave and can be separated into a time-dependent part and a space-dependent part.

Matter waves describe moving particles, such as electrons, as waves with a de Broglie wavelength λ_{dB} related to the magnitude of the atom's momentum p by $\lambda_{dB} = h/p$, where $h = 6.626 \cdot 10^{-34}\,\mathrm{J \cdot s}$ is Planck's constant. In the case of a hydrogen atom assuming a circular orbit for the electron, the wave function can be used to calculate the probability of locating the electron at a specific position around the nucleus. Additionally, the total energy of the electron is the sum of its kinetic and potential energies [3].
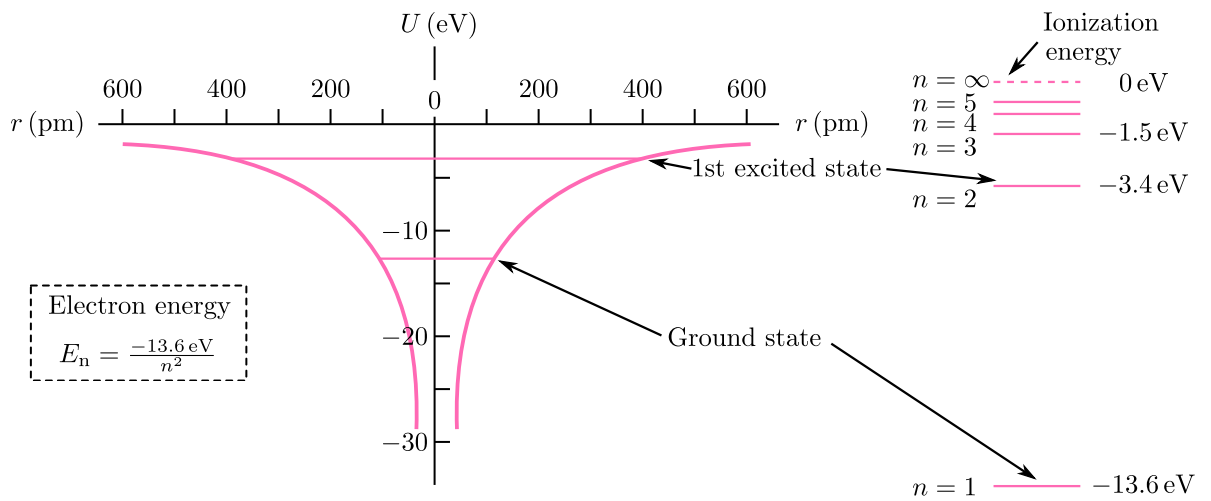

Fig. 1.3: The potential energy U of a hydrogen atom as a function of the separation r between the electron and the central proton with electron energy E_n. Adapted from [3].

In Schrödinger's model of the hydrogen atom, the electron is in a potential energy trap caused by its electrical attraction to the proton at the center of the atom, as shown in Figure 1.3. The potential energy as a function of r can be written as $U(r) = -\frac{e^2}{4\pi\varepsilon_0 r}$, where $e = 1.602 \cdot 10^{-19}\,\mathrm{C}$ is the elementary charge. To determine the allowed energies and wave functions for an electron trapped in the potential well, we apply Schrödinger's equation 1.10, which depends only on the radial distance r. The solution of the latter equation requires a quantum number n and produces the energy values E_n of the electron, which are quantized according to

$$E_n = -\frac{m_e e^4}{8\varepsilon_0^2 h^2}\frac{1}{n^2}, \tag{1.11}$$

---

[4]Utilizing the Laplacian operator, which depends on the position vector, we can simplify those three differential equations into a single equation.

where $m_e = 9.109 \cdot 10^{-31}$ kg is the electron mass, n is a positive integer. This equation shows that the energy E_n of the hydrogen atom is quantized, which means that E_n is limited by its dependence on the quantum number n. When we evaluate the constants in Eq. 1.11, we obtain the energy levels shown in Figure 1.3.

The quantum number n identifies the orbit[5], with the lowest energy level E_1 referred to as the ground state, and higher levels E_2, E_3, etc. being excited states. As n increases, the corresponding energy E_n approaches 0 and when $n \to \infty$, $E_n \to 0$, the electron is no longer bound to the nucleus to form an atom. A positive energy indicates that the electron is free and has no quantum conditions to satisfy [6].

The ionization energy represented by the dashed line in Figure 1.3 is defined as the amount of work required to remove an electron from an atom in its ground state. For hydrogen, the ionization energy is 13.6 eV, since the ground-state energy of the hydrogen atom is -13.6 eV, and the ionization energy is accordingly equal to $-E_1$. Since the nucleus is assumed to be fixed in place and only the electron has motion, we can assign the energy values of Eq. 1.11 to either the atom as a whole or the electron alone [6].

1.2.2   Energy levels in multielectron atoms

The energy levels of multielectron atoms can be accurately determined using Schrödinger theory (Eq. 1.10), provided that relativistic effects are negligible. The Schrödinger equation for Z electrons can be decomposed into Z single-electron Schrödinger equations, with a total energy that is the sum of the energies of the individual electrons, and an overall eigenfunction that is a product of the individual-electron eigenfunctions. Perturbation theory is employed to account for deviations from spherical symmetry in the repulsive potential and interactions involving electron spin. The resulting single-electron eigenfunctions are closely related to those of the hydrogen atom and are expressed in a similar form [4].

In the context of semiconductor materials, the electronic energy levels are typically described using energy bands and the density of states, which represents the number of occupied states per unit volume within a given energy level range for a system in thermal equilibrium. This can be seen in Figure 1.4. Due to the dense spacing of atoms in a lattice, the discrete energy levels are broadened into a continuous range of energies, resulting in closely spaced energy levels that are indistinguishable from one another. The valence band and conduction band are the two essential energy bands in semiconductors, and the bandgap, denoted as E_g, represents the difference in energy between the maximum energy of the valence band (E_V) and the minimum energy of the conduction band (E_C).

When a photon with energy equal to or greater than the bandgap[6] energy interacts with a semiconductor, it can excite an electron from the valence band to the conduction band, leaving behind a hole in the valence band. Both valence band holes and conduction

---

[5]An electron circles a nucleus if its orbit contains an integral number of de Broglie wavelengths [6].

[6]Semiconductors have a bandgap energy ranging from about 0.1 eV to 4 eV [7].
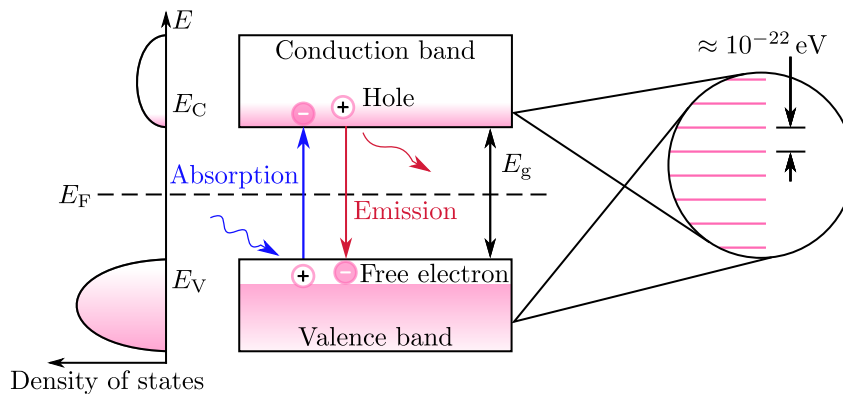
Fig. 1.4: On the left-hand side of the Figure is the density of states for a semiconductor, which shows the conduction and valence bands, as well as the density of states for each. The Fermi energy (E_F) is located in the middle of the bandgap (E_g), and the pink area indicates the fully occupied bands. When light is absorbed, a small number of electrons near the top of the valence band (E_V) can acquire enough energy to jump the bandgap and enter the conduction band (E_C), generating free electron and hole carriers. The energy levels within the bands are closely spaced, as illustrated in the detail on the right-hand side of the Figure. Adapted from [6].

band electrons are mobile within the material, enabling the conduction of charge. The motion of these free electrons and holes is determined by the material's band structure in k-space, which represents the momentum space of the electrons and describes their allowed energy states.

Molecules, on the other hand, are formed by the combination of two or more atoms, where the sharing of valence electrons by the constituent atoms results in the formation of a stable molecule with reduced overall energy. The bonding between atoms in a molecule can be covalent or ionic, and van der Waals bonding arises from the interaction of molecular dipoles. The energy levels of molecules are determined by the nature of the bonding and the potential energies associated with the interatomic forces. The highest occupied molecular orbital (HOMO) and the lowest unoccupied molecular orbital (LUMO) play key roles in determining molecular energy levels, and in organic semiconductors[7], they play analogous roles to the conduction and valence bands of inorganic semiconductors [4].

1.2.3 Energy level transitions

This section pertains to the phenomenon of energy level transitions in an isolated atom, which occurs when it is excited by light[8], which can exist in either its ground state or an excited state represented by the pink lines in Figure 1.5. The energy difference between the two states is denoted as $E_2 - E_1$, and if a photon with a frequency f matching this energy difference ($E = hf$) is present, it can interact with the atom. This interaction can result in

---

[7]Organic semiconductors are usually either small organic molecules or conjugated polymer chains [4].

[8]Thermal excitation can also serve as an external source of energy, resulting in the emission of light.

the emission or absorption of a photon, as the atom undergoes a transition between energy levels while conserving energy. There are three possible forms of interaction: absorption, spontaneous emission, and stimulated emission.
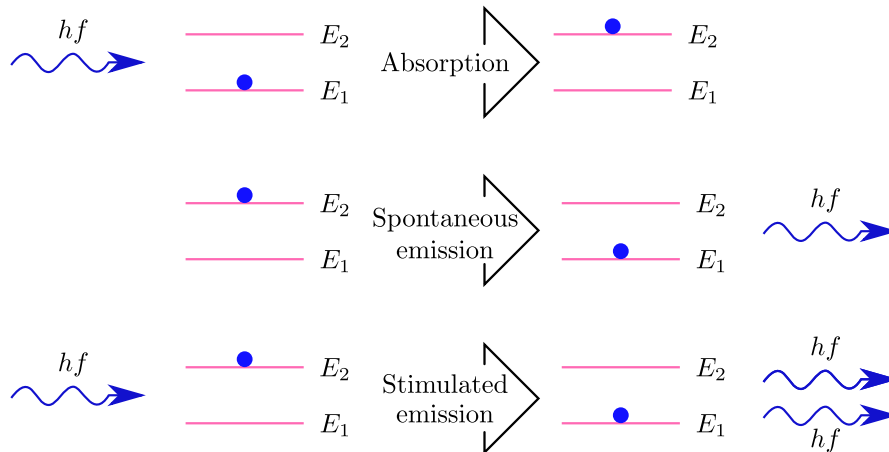

Fig. 1.5: The interaction of radiation and matter in the processes of absorption, spontaneous emission, and stimulated emission. Adapted from original [3].

In particular, absorption occurs when an electromagnetic field with frequency f is present, and the atom absorbs an amount of energy hf to transition to the higher-energy state. Conversely, spontaneous emission occurs when the atom is in an excited state and emits a photon of energy hf as it transitions to its ground state. Stimulated emission occurs when radiation with frequency f is present, and a photon of energy hf stimulates the excited atom to transition to its ground state and emit a second photon with identical properties. The purpose of this subsection is to introduce the laws responsible for the generation of laser and luminescence light [4].

Direct and indirect band gap

In energy transfer and light-matter interaction, the focus is on direct band gap transitions, where electrons and holes in the conduction and valence bands have the same crystal momentum. However, in indirect band gap semiconductors, the crystal momentum of electrons and holes differs, making it impossible for a photon to be emitted directly. Radiative recombination is possible in direct band gap semiconductors, but not in indirect ones, requiring the absorption or emission of a phonon. Direct band gap materials are preferred for light-emitting and laser diodes, as well as photovoltaics. Figure 1.6 shows the difference between direct and indirect optical band gaps. Direct transition can occur in some indirect band gap semiconductors, but for others, conservation laws[9] must be satisfied for electron transition to occur [8].

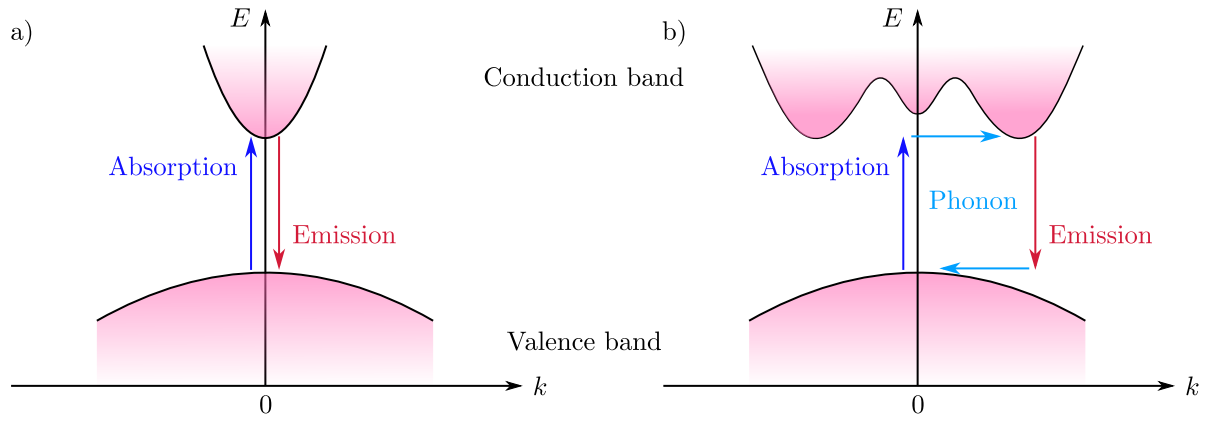[9]It must satisfy the conditions of conservation of energy and quasi-momentum.

Fig. 1.6: Direct and Indirect Optical Band Gaps. a) The direct band gap occurs when the minimum of the conduction band coincides with the maximum of the valence band. This type of band gap facilitates efficient emission and absorption processes, with photon energies close to the band gap energy. b) The indirect band gap requires additional phonons to assist in the momentum change of electrons during absorption and emission processes. Adapted from [8].

Excitons

Understanding the behavior of charge carriers in semiconductors and insulators is essential to comprehend the optoelectronic properties of these materials. In these materials, when a photon is absorbed, it can create an exciton (as shown in Figure 1.7), a quasi-particle consisting of an electron and a hole. The theoretical description of excitons considers two types: Wannier-Mott and Frenkel excitons, which have different radii and behaviors depending on the type of material. In semiconductors, when the electron and hole maintain a Coulombic attraction and enter a stable orbit, they form a weakly bound Wannier-Mott exciton ($\sim 10\,\text{meV}$), which can diffuse freely through the material, contributing to its electrical conductivity. On the other hand, tightly bound Frenkel excitons ($\sim 1\,\text{eV}$) form in insulators and molecular crystals, with a small radius localized to a few molecules [8].

Hot charge carriers are created when an electron is excited to an energy above the minimum of the conduction band. These hot carriers can lose energy through scattering processes and "cool" to the conduction band edge. When free electrons and holes recombine, they can emit a photon. The details of the band structure and carrier dynamics are commonly discussed in solid-state physics textbooks [6, 8].

Excitons have their own kinetic energy and quasi-momentum, allowing them to propagate through the crystal and act as carriers of excitonic energy. They can exist within the bandgap with bound energies lower than that of free electron-hole pairs due to the binding energy of the exciton E_{B}.

Excitons play a significant role in various optoelectronic devices, such as solar cells, LEDs, and lasers as will be discussed in chapter 2. Therefore, understanding the behavior of excitons and charge carriers in semiconductors and insulators is crucial for the design

and optimization of these devices, making it a crucial topic for the diploma thesis. In summary, the study of excitons and charge carriers in semiconductors and insulators is an essential area of research for the development of modern optoelectronic devices.
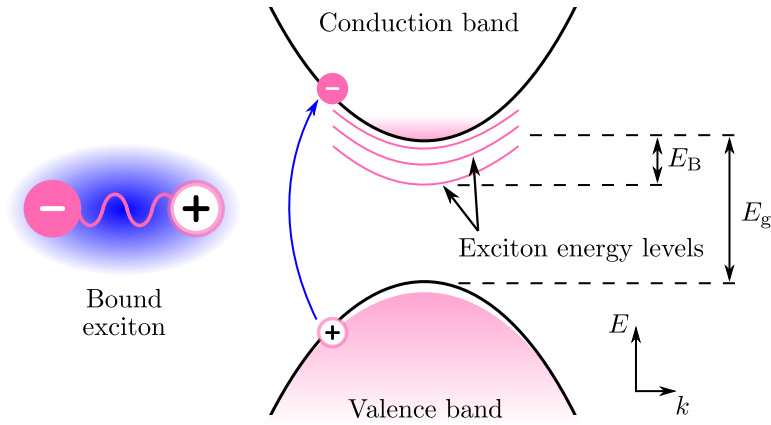

Fig. 1.7: An exciton is formed in a semiconductor when particle-hole excitations are bound together by the Coulomb interaction, resulting in a composite system with a binding energy of E_B. Adapted from [3, 9].

1.2.4 Nonlinear processes

As discussed in the previous subsection on energy level transitions, when light interacts with matter, it can undergo various processes, such as absorption and emission, that correspond to transitions between different energy levels. In addition to these linear processes, light can also undergo nonlinear processes when it passes through a nonlinear medium. These processes are described by the nonlinear wave equation [4], which accounts for the interaction of the electric field of light with the nonlinear polarization of the medium. One of the most significant characteristics of a nonlinear medium is its $\chi_e^{(2)}$ coefficient (see Eq. 1.9), which determines the magnitude of the nonlinear response of the crystal.
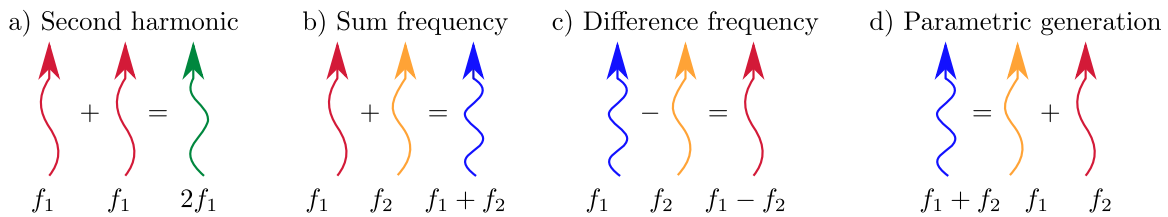

Fig. 1.8: Nonlinear processes of a) second harmonic generation (SHG), b) sum frequency generation (SFG), c) difference frequency generation (DFG), and d) parametric generation. Adapted from [10].

One of the most common second-order nonlinear processes is frequency doubling, or second harmonic generation (SHG) shown in Figure 1.8a, where two photons with the

same wavelength are combined through a nonlinear process to generate a third photon with twice the frequency. Other second-order processes include sum frequency generation (SFG) and difference frequency generation (DFG), where two input photons are combined to generate a new photon with a frequency determined by their sum or difference, respectively (Figure 1.8b-c) [11].

In contrast, parametric processes shown in Figure 1.8d involve the splitting of a single input photon into two generated photons, where the only requirement is that the combination of frequencies of the generated photons conserves energy. Phase matching is critical in these processes to ensure efficient generation of the desired frequency combination [10].

Phase matching is a group of techniques for achieving efficient nonlinear interactions between light and a medium. Nonlinear optical processes, such as SHG and parametric generation, rely on the interaction of two or more frequencies of light with a nonlinear medium. In these interactions, the frequencies mix, and new frequencies are generated by combining the input frequencies. However, the efficiency of these interactions depends on the phase relationship between the input and generated frequencies [10].
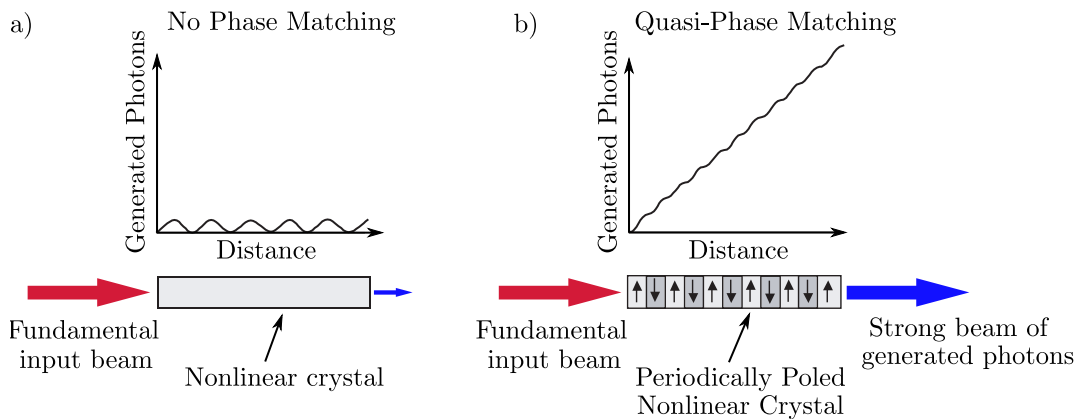

Fig. 1.9: Comparison of conversion efficiency between a) Nonphase matched materials and b) Quasi-phase matched materials using a periodical structure to offset the accumulated phase mismatch in a nonlinear optical crystal. Adapted from [10].

If the phase relationship between the input and generated frequencies changes as the light passes through the medium, the efficiency of the nonlinear interaction is reduced. This is because the generated frequencies will interfere destructively, and the number of photons that exit the medium will be reduced. Phase matching techniques ensure that the phase relationship between the input and generated frequencies is preserved throughout the interaction, resulting in efficient and effective nonlinear interactions. However, this technique has its drawbacks, such as a limited number of available materials and the range of wavelengths that can be phase-matched within these materials [12].

Quasi-phase matching (QPM) is a technique that overcomes some of the limitations of traditional phase matching by using a periodic structure to create a quasi-phase-matched (QPM) material. In QPM, the nonlinear medium is divided into a series of thin sections, each with a different orientation. The orientation of each section is chosen to compensate

for the phase mismatch between the input and generated frequencies, resulting in a net phase-matched interaction over the entire length of the material [10].

Figure 1.9 shows the difference between no phase matching and QPM. In Figure 1.9a, the input and generated frequencies have a significant phase mismatch, resulting in destructive interference and a reduction in the number of photons that exit the material. In Figure 1.9b, the QPM structure compensates for the phase mismatch, resulting in a net phase-matched interaction and an increase in the number of photons that exit the material.

QPM has several advantages over traditional phase matching, including a broader range of available materials and the ability to phase-match multiple wavelengths within the same material. It is widely used in applications such as frequency conversion, optical parametric amplification, and second-harmonic generation [13].

Materials such as beta-barium borate (BBO), lithium triborate (LBO), lithium niobate (LN), and potassium titanyl phosphate (KTP) are commonly used in practical applications, along with their periodically poled derivatives, periodically poled lithium niobate (PPLN) and periodically poled potassium titanyl phosphate (PPKTP). These materials are utilized in at least 75 % of all practical applications today [14]. Achieving efficient second-order nonlinear optical processes in these bulk materials requires high optical powers, as well as phase matching conditions and long interaction lengths L. The efficiency of second harmonic generation η_{SHG} can be expressed as

$$\eta_{\text{SHG}} = C^2 \frac{L^2}{A} P, \tag{1.12}$$

where C^2 is the empirical constant, P is the incident optical power at the fundamental frequency, and A is the effective area of the interaction.
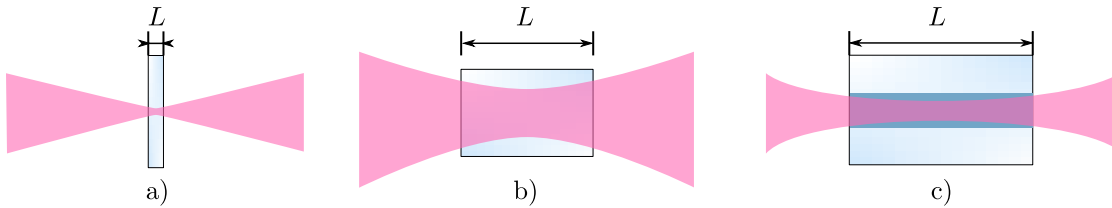

Fig. 1.10: SHG interaction volumes. a) For a thin crystal, minimize A. b) For a thick crystal, maximize A. c) For an optical waveguide, maximize L. Adapted from [4].

According to Eq. 1.12, the incident wave's power, P, plays a crucial role in maximizing SHG efficiency. Therefore, to achieve the highest η_{SHG}, it is necessary to use pulsed lasers that confine the energy in time, resulting in large peak powers [4].

In addition to maximizing the power of the incident wave, the wave's spatial properties also impact SHG efficiency. The ratio L^2/A needs to be maximized to achieve the highest efficiency. To achieve this, the wave should be focused to the smallest possible area A and the longest possible interaction length L.

For a thin crystal (Figure 1.10a), the length of the crystal determines the interaction length, which means that the beam should be focused to the smallest spot area A to maximize the efficiency. On the other hand, if the dimensions of the nonlinear medium are not limiting factors, the maximum value of L for a given area A is limited by beam diffraction. In such cases, a Gaussian beam focused to the largest spot size, corresponding to the largest depth of focus, results in the highest efficiency, and the efficiency is proportional to L.

For a thick crystal (Figure 1.10b), the beam should be focused to the largest spot that fits within the cross-sectional area of the crystal to maximize the efficiency. Therefore, the optimal beam size and focus position depend on the crystal's thickness and dimensions, as well as the beam properties.

Guided-wave structures (Figure 1.10c) provide the benefit of confining light in a small cross-sectional area for extended distances. The efficiency of this confinement is directly proportional to L^2, as the size of the guided mode A is determined by the length [4].

In summary, to maximize SHG efficiency, it is essential to use pulsed lasers to achieve high peak powers and focus the wave to the smallest possible area A and longest possible interaction length L. The optimal beam size and focus position depend on the crystal's thickness and dimensions, as well as the beam properties. In a later section 3.1.3, we will be utilizing the mentioned pulsed laser and thin crystal to achieve efficient SHG.

1.3 Photoluminescence

Luminescence, derived from the Latin word lumen meaning light, refers to the emission of electromagnetic radiation that has a decay time much longer than the period of light oscillations (10^{-15} s). The different ways of providing energy to a substance to convert it into luminescent light gives rise to different types of luminescent processes such as photoluminescence, electroluminescence, chemiluminescence, bioluminescence, cathodo-luminescence, mechanoluminescence, and thermoluminescence [15].

The term luminescence, encompassing both fluorescence and phosphorescence shown in Figure 1.11, was introduced in the late 19th century [15]. While organic matter and inorganic materials such as semiconductors exhibit luminescence, their origins differ fundamentally[10], as discussed in section 1.2.2.

Photoluminescence is the emission of a photon with lower frequency than the absorbed photon when an excited molecule returns to its ground state, known as Stokes emission. Anti-Stokes photoluminescence, in which a molecule emits a photon with higher frequency upon relaxation to the ground state, also exists [4]. The $CsPbBr_3$ sample analyzed in results 3.3.2 exhibits anti-Stokes photoluminescence [16]. Luminescence can be divided

---

[10]The anharmonic oscillator model should be used for accurate understanding of systems that undergo significant structural changes or exhibit large amplitude oscillations upon excitation or relaxation.
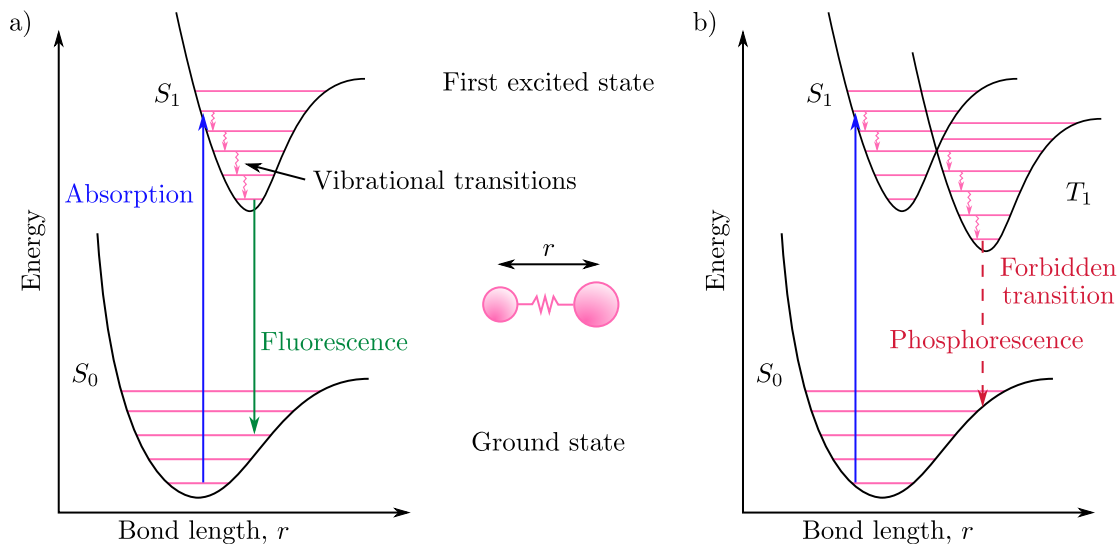
Fig. 1.11: a) Fluorescence: Absorbed radiation is emitted at a lower frequency. b) Phosphorescence: The final transition is delayed because it violates the selection rules for electronic transitions. Adapted from [6]

into intrinsic, which arises in an ideally clear and intact crystal lattice, and extrinsic, which arises in defects or impurities in the lattice [15].

Intersystem crossing is a crucial process in the field of molecular electronics, as it involves the nonradiative transition of a singlet state to a triplet state or vice versa as shown in Figure 1.11b. This process results in a reversal of the spin of the excited electron. The probability of intersystem crossing is higher when the vibrational levels of the two states overlap, which minimizes the energy gain or loss during the transition. Spin-orbit coupling, which involves the coupling of electron spin with the orbital angular momentum of non-circular orbits, is responsible for this process. Heavy-atom molecules, such as those containing iodine or bromine, have substantial spin-orbital interactions, and are more prone to intersystem crossing. Additionally, the presence of paramagnetic species in solution enhances this process [17].

Singlet and triplet states are electronic states in molecules that can be described by the spin quantum number[11]. In a singlet state, the total spin of the electrons is zero, meaning that all electron spins are paired, while in a triplet state, two unpaired electrons have parallel spins [6].

When an electron is excited from a molecule's ground state to a higher energy level, it can lead to either an excited singlet or an excited triplet state. Singlet and triplet states describe the electronic spin states of a molecule's excited state. The transition from singlet to triplet state involves a forbidden spin transition, making it less likely for a triplet state to form when the molecule absorbs radiation [4].

The schematic diagram presented in Figure 1.12 illustrates the singlet and triplet states that result from the absorption of radiation and the excitation of the electron to a higher

---

[11]It describes the intrinsic angular momentum of the electron and can have values of $\pm 1/2$.

energy level. The diagram features a red arrow to depict the spin-up state and a blue arrow to depict the spin-down state.
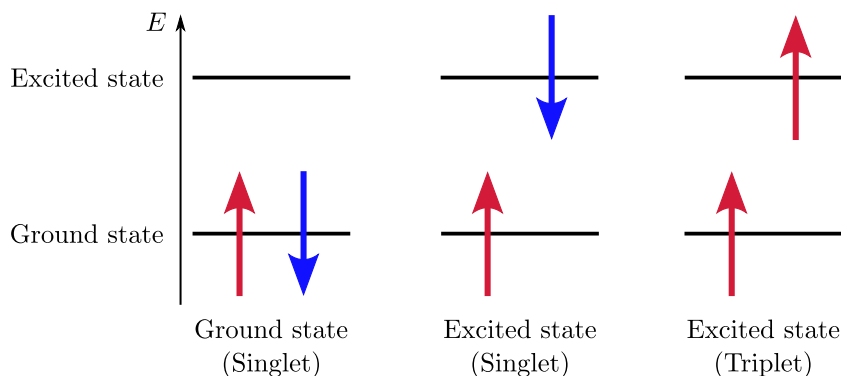

Fig. 1.12: Energy level diagram showing the transition of an electron in a molecule from the singlet ground state to a higher energy excited state, which can be either singlet or triplet. The lowest level of the one electron energy level diagram is occupied by two electrons (red spin-up, blue spin-down).

Molecules have multiple electronic states, and decay pathways can occur through radiative or non-radiative processes. The distinction between these processes is whether they involve the emission of a photon. The repopulation of the ground state or reaching a new equilibrium can involve both radiative and non-radiative processes. These processes differ in their time scales, such as rotational, vibrational, and electronic transitions [6], which will be discussed further in the following section.

1.3.1 Jablonski diagram

The Jablonski diagram is a representation of the energy levels of complex organic molecules that helps to deduce the basic features of luminescence in organic materials. In this diagram, the ground state of the molecule is the singlet state, denoted as S_0, and higher electronic states are primarily excited singlet states (S_1, S_2, S_3, etc.). Higher excited singlets S_2, S_3 relax non-radiatively to the state S_1, and the transition from S_1 to S_0 leads to the emission of luminescent photons, which is fluorescence [18].

In addition to singlet states, excited triplet states (T_1, T_2, T_3, etc.) can also exist. A radiative transition from a triplet to a singlet state is "forbidden," which means it has only a small likelihood of occurring, and resulting phosphorescent radiation may be emitted even seconds after the initial absorption (also see Figure 1.11).

A typical Jablonski diagram shown in Figure 1.13 consists of horizontal black lines representing the energy levels of a molecule, with the energy increasing along the vertical axis of the diagram. The vibrational levels become more closely spaced as energy increases and eventually form a continuum. The naming of the electronic states is based on the spin angular momentum configuration of each state. Singlet states, with a total spin angular momentum of zero, are denoted by an S, and triplet states, with a total spin

angular momentum of one, are denoted by a T. Radiative and non-radiative transitions are represented in a Jablonski diagram by straight arrows and wavy arrows, respectively.

The absorption of a photon moves the molecule from the S_0 to one of the vibrational levels of the singlet excited states (S_1, S_2, etc.). Vibrational relaxation occurs on a rapid time-scale of $(10^{-12} - 10^{-10})$ s and outcompetes all other transitions, and the molecule returns to the ground state through this process. Internal conversion is a non-radiative transition between two electronic states of the same spin multiplicity, and the rate of internal conversion is inversely proportional to the energy gap between the two electronic states. The closely spaced higher lying singlet excited states ($S_3 \to S_2$, $S_2 \to S_1$) undergo internal conversion to the lowest vibrational level of the electronic state, followed by vibrational relaxation to the lowest vibrational level of the electronic state [19].
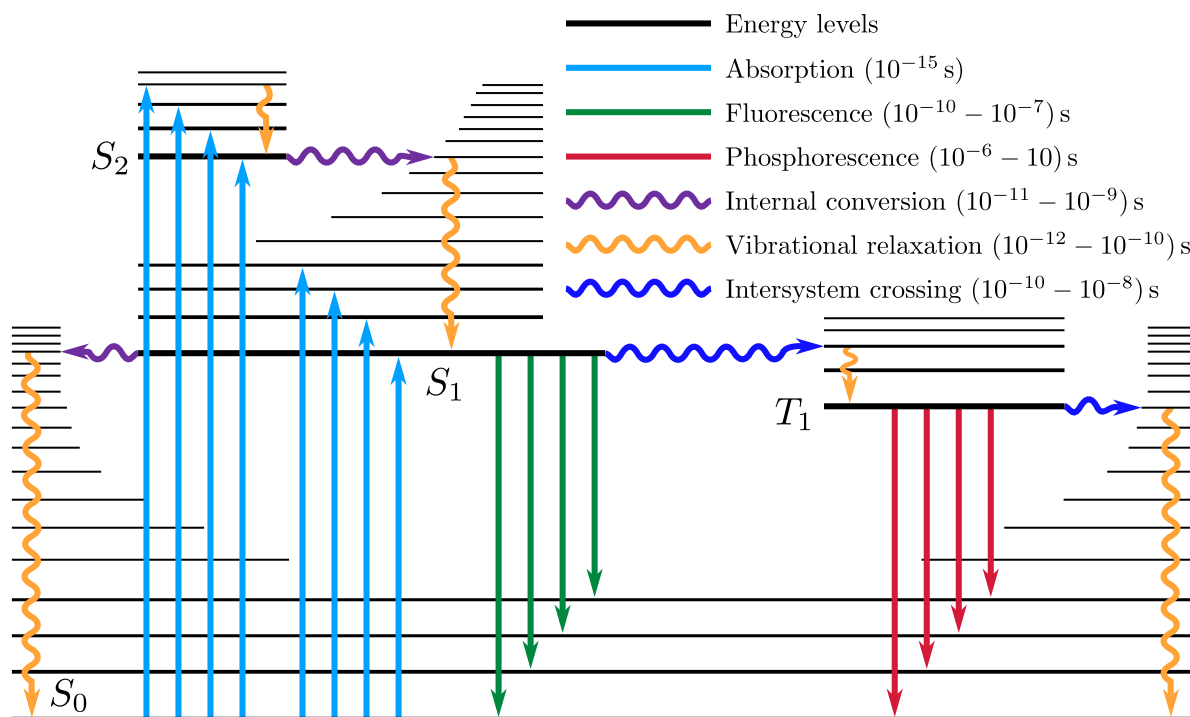

Fig. 1.13: A Jablonski diagram that presents the potential radiative and non-radiative transitions. Adapted from [19, 20].

The current chapter has established a strong understanding of the photoluminescence phenomenon by building upon the theoretical concepts covered in the previous sections. The discussion on electronic structures, energy levels in multielectron atoms, and energy level transitions has been particularly informative in this regard. We have also introduced the Jablonski diagram as a useful tool for visualizing the possible transitions after photoexcitation of a molecule. It is important to note that the methods discussed in subsequent chapters, including optical spectroscopy, luminescence spectroscopy, and time-resolved spectroscopy, will be essential for further studying and utilizing photoluminescence for various applications.

2 Experimental methods

This chapter describes the experimental methods used to investigate the photoluminescence properties of the samples. Optical and luminescence spectroscopy, as well as time-resolved spectroscopy, were utilized to obtain information on the energy levels, band structures, and carrier dynamics of the samples. The chapter also covers photoluminescence mapping and scanning near-field optical microscopy (SNOM) techniques used to visualize the spatial distribution of photoluminescence. This section provides an overview of the methods used in this study, including the instrumentation and techniques employed in optical and luminescence spectroscopy, and the principles underlying the various spectroscopic measurements.

To understand these techniques, it is important to have a clear understanding of the principles of optical spectroscopy, where the analysis of light is typically based on its wavelength, wavenumber, frequency, or energy. Figure 2.1 illustrates the comparison among the four types of abscissa commonly used in visible spectrometers.
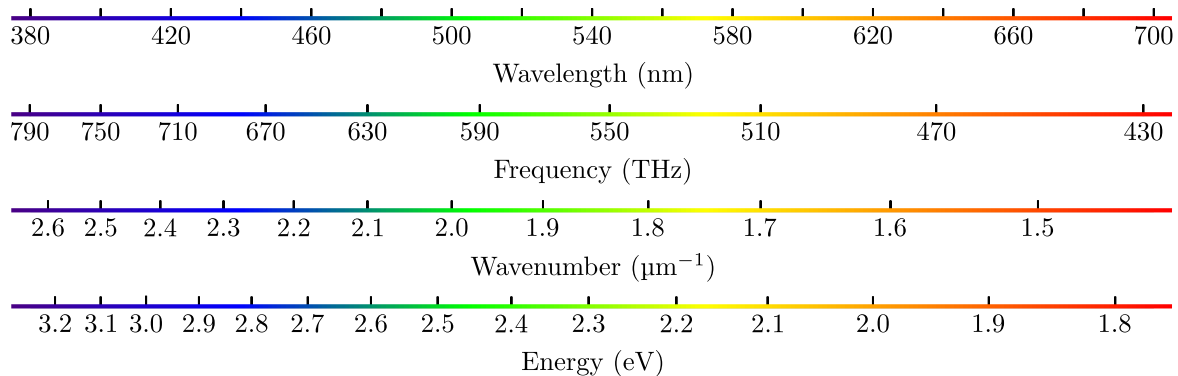

Fig. 2.1: A comparison of the four abscissa types typically used for visible spectrometers: wavelength, wavenumber, frequency, and energy.

The wavelength and frequency of electromagnetic radiation are related by the equation $\lambda = c/f$, where $c = 3 \cdot 10^8$ m/s is the speed of light in vacuum. The frequency is inversely proportional to the wavelength, and in spectroscopy, it is commonly expressed in terahertz (THz). The wavenumber, defined as the reciprocal of the wavelength (expressed in cm^{-1} or μm^{-1}) is directly proportional to frequency. The energy of a photon can be calculated using the equation $E = hf$, where h is Planck's constant, and is typically measured in electronvolts (eV) or joules (J).

2.1 Optical spectroscopy

Optical spectroscopy studies how light interacts with matter through absorption, transmission, reflection, and scattering. Spectrometers, including spectrographs and monochromators, are crucial for measuring light properties across the electromagnetic spectrum.

These devices rely on optical components like diffraction gratings, which split light into multiple beams through diffraction or dispersion prisms (see Figure 2.2a). Diffraction gratings are preferred due to their higher dispersion efficiency and precision [21].
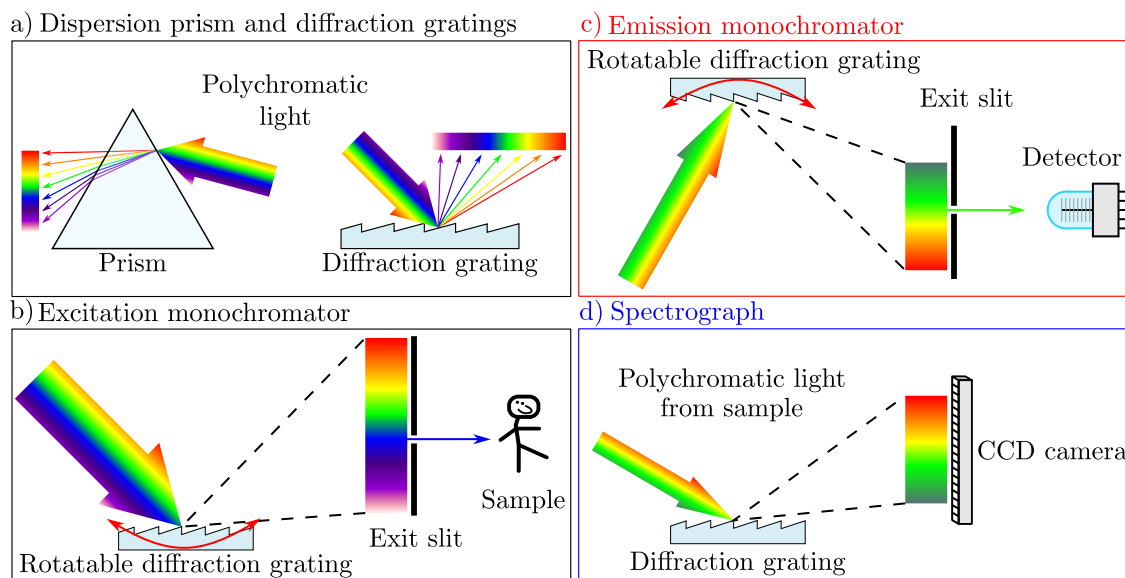

Fig. 2.2: Illustration of the operating principles of monochromators and spectrographs. (a) The dispersion prism and diffraction gratings are used for separating wavelengths. The dispersion prism separates wavelengths through wavelength-dependent refraction, while diffraction gratings separate wavelengths through diffraction due to their surface. (b) Excitation monochromators use rotatable diffraction gratings to select the desired excitation wavelength, while (c) emission monochromators measure the change in signal as a function of emission wavelength. (d) Spectrographs detect the spectrum of dispersed light all at once using an array detector, such as a CCD camera. Combining (b) excitation and (c) emission monochromators results in a spectrofluorometer. Adapted from [22].

Optical spectroscopy has become an indispensable tool in numerous fields, such as materials science, chemical analysis, and biomedicine. For example, ultraviolet-visible spectroscopy measures the bandgap energy of semiconductors and molecular absorption in the visible and ultraviolet spectrum [23, 24]. Infrared spectroscopy explores the vibration of molecules in the infrared range [25].

To obtain the most information, the interaction or emission of light should be measured as a function of wavelength or frequency, and the common feature of all optical spectrometers is therefore a mechanism for wavelength selection. Diffraction gratings, as shown in Figure 2.2a, spatially separate polychromatic light that is incident on the grating using constructive and destructive interference [4].

Spectrometers come in different types, including monochromators and spectrographs (see Figure 2.2b-d). Monochromators use diffraction gratings to select a specific wavelength of light from a polychromatic source. Excitation monochromators, pictured in Figure 2.2b, choose the desired excitation wavelength, while emission monochromators,

depicted in Figure 2.2c, select the wavelength of light emitted from a sample. The combination of excitation and emission monochromators results in a spectrofluorometer[1]. Spectrographs, illustrated in Figure 2.2d, split up wavelengths from a broadband source, and each wavelength is imaged to a different set of pixels on a detector array. They are commonly used when a quick analysis of a spectrum is needed. Modern spectroscopes generally use a movable diffraction grating or slit, and some kind of photodetector, all automated and controlled by a computer [22].

In section 3.1, the experimental setup will use a Czerny-Turner optical design which is a popular choice due to its ability to avoid spherical aberration by utilizing only two spherical mirrors and a plane grating in a coma-free geometry [26]. This design is depicted in Figure 2.2d and allows for a quick analysis of a spectrum without requiring the scanning of different wavelengths across the detector, making it highly advantageous for experimental work.

2.2 Laser spectroscopy

Laser[2] spectroscopy, unlike traditional optical spectroscopy, utilizes coherent and monochromatic laser light sources to study the interaction between matter and light [27]. Laser light is emitted through stimulated emission of electromagnetic radiation, as illustrated in Figure 1.5. In laser spectroscopy, the sample under investigation interacts with a beam of laser light, and the resulting spectrum is analyzed to determine the sample's properties.
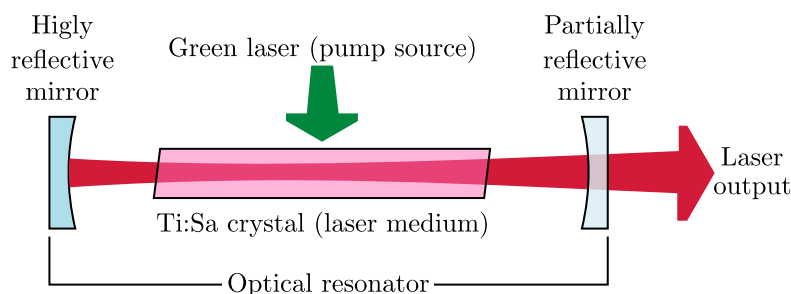

Fig. 2.3: Schematic diagram of a Titanium:Sapphire (Ti:Sa) laser, illustrating the three main components.

The components of a laser system include the pump source, the gain or laser medium, and an optical resonator, as shown in Figure 2.3. The pump source supplies energy to the laser system, and the type of pump source used depends on the gain medium. The gain medium determines the laser's wavelength of operation and other properties. Various types of gain media are available, including liquids, gases, solids, and semiconductors such as diode lasers. The optical resonator is formed by two mirrors around the gain medium,

---

[1]A spectrofluorometer measures a sample's fluorescence (generally, the photoluminescence) emission.

[2]An anacronym originating from acronym "Light Amplification by Stimulated Emission of Radiation".

which reflects the light back into the medium. Other optical devices, such as modulators, filters, and absorbers, can be used to alter the laser output [28].

Laser spectroscopy has a wide range of applications in various fields, including physics, chemistry, biology, medicine, and environmental science. There are many types of lasers used in laser spectroscopy, including gas lasers [29], chemical lasers [30], excimer lasers [31], fiber lasers [32], dye lasers [33], free electron lasers [34], quantum cascade lasers [35], mode-locked lasers [36], broadband tunable solid-state lasers, and fixed-wavelength solid-state lasers [37].

A laser is characterized by various parameters, including power, energy, pulse duration, repetition rate, and beam diameter. The power of a laser is measured in watts (W) and can describe the optical power output of a continuous wave (CW) laser or the average power P_{avg} of a pulsed laser, which is proportional to the pulse energy E and inversely proportional to the laser's period Δt

$$P_{\text{avg}} = \frac{E}{\Delta t}, \qquad\qquad P_{\text{peak}} \approx \frac{E}{\tau}. \tag{2.1}$$

The characteristics of laser pulses, including their period Δt, peak power P_{peak}, and pulse width τ, are described in Figure 2.4. The peak power P_{peak} is then often calculated from the full width at half-maximum (FWHM) pulse duration, which can be measured with an optical autocorrelator [38]. The pulse energy depends on the temporal shape of the pulse and its lifetime τ. Higher repetition rates result in less thermal relaxation time at the surfaces of the laser optics and at the final focused spot, leading to more rapid material heating.
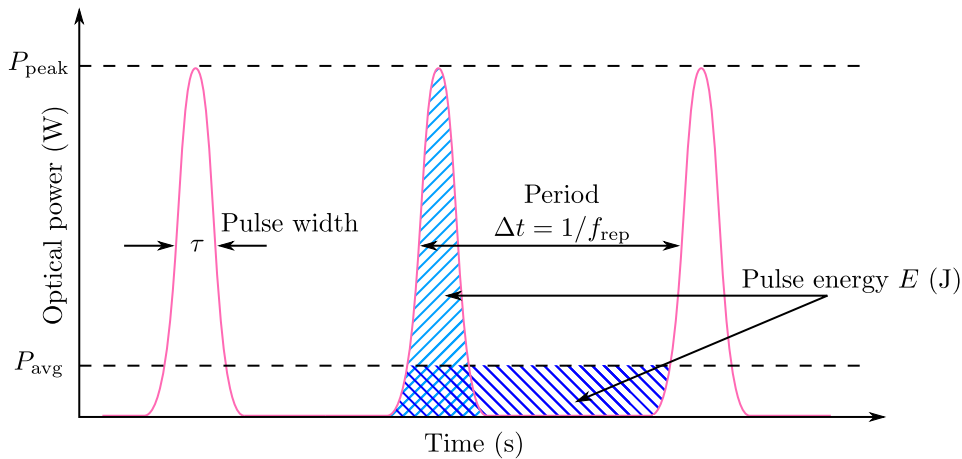

Fig. 2.4: The characteristics of laser pulses (pink) are described by their period Δt, peak power P_{peak}, and pulse width τ. Pulsed lasers emit bursts of light with a spacing in time determined by the period and peak power. The CW laser's output power equals the pulsed laser's average power P_{avg}. The laser pulses (light blue marks) and CW laser (dark blue marks) output provide same energy per period.

In this thesis, two specific types of lasers will be used in the experimental section 3.1: picosecond diode lasers and femtosecond Ti:Sa lasers.

2.2.1 Raman spectroscopy

Raman spectroscopy is an analytical technique used to investigate the vibrational energy modes of a sample by analyzing the scattered light. When light interacts with a molecule, the scattered photon can gain or lose energy, leading to a shift in its wavelength. This process is illustrated in the energy level diagram for Raman scattering in Figure 2.5a.

In Raman scattering, the molecule is excited into a virtual energy level and then decays to a lower energy level by emitting a photon of different energy and wavelength. Stokes Raman scattering is the process in which the molecule gains energy, and the scattered photon loses energy, resulting in a longer wavelength. In contrast, Anti-Stokes Raman scattering occurs when the molecule loses energy, and the scattered photon gains energy, resulting in a shorter wavelength. Stokes Raman scattering is more likely to occur since the majority of molecules are in the ground vibrational level [39].
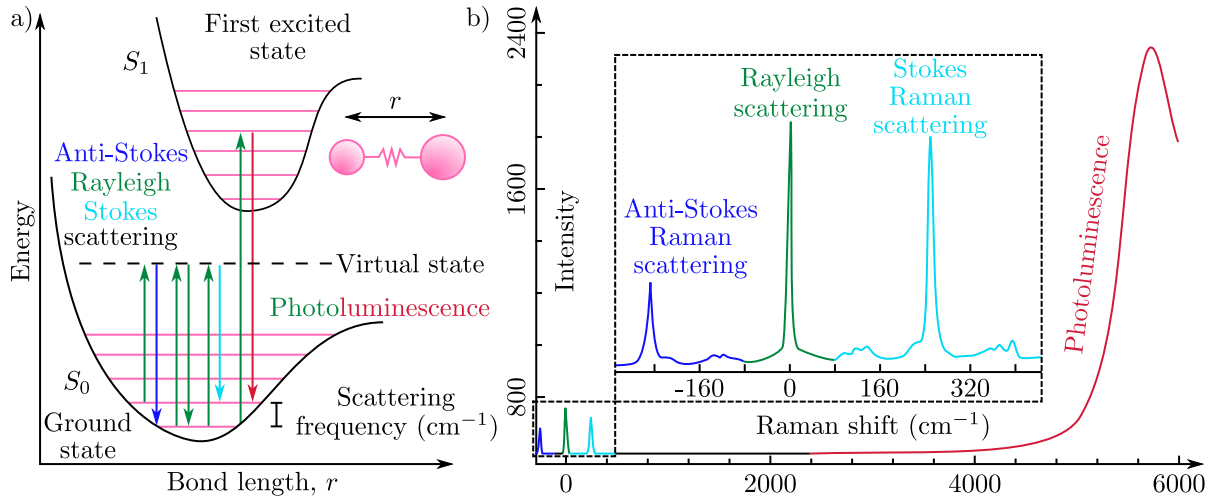

Fig. 2.5: a) Schematic diagram of the energy level diagram for a diatomic molecule, indicating the processes of Anti-Stokes, Rayleigh, and Stokes Raman scattering, as well as photoluminescence emission, respectivaly. b) Raman spectrum and PL emission obtained from a WSe_2 monolayer excited by a green laser (532 nm) and measured by the author.

Figure 2.5b shows the entire spectrum of a tungten diselenide (WSe_2) monolayer excited by a green laser (532 nm), including the different types of Raman scattering and photoluminescence spectrum. The dark blue peak corresponds to Anti-Stokes Raman scattering, the green peak represents Rayleigh scattering, and the light blue peak represents Stokes Raman scattering. The red peak indicates the photoluminescence (PL) emission. The Raman scatter position is converted to a Raman shift away from the excitation wavelength to enable practical comparison between spectrum obtained using different lasers.

Raman spectroscopy is a powerful tool for characterizing the vibrational modes of molecules and materials, with numerous applications in materials science, chemistry, physics, biology, medicine, and other fields [19, 39]. A typical Raman microscope comprises a fiber-coupled laser source and spectrometer, as depicted in Figure 2.6a. Raman spectroscopy allows for non-destructive and non-invasive mapping of molecular vibrations and provides spatial information about the distribution of molecular species in a sample. Figure 2.6b shows the concept of Raman spectroscopy mapping using point-by-point and line scan[3] imaging.
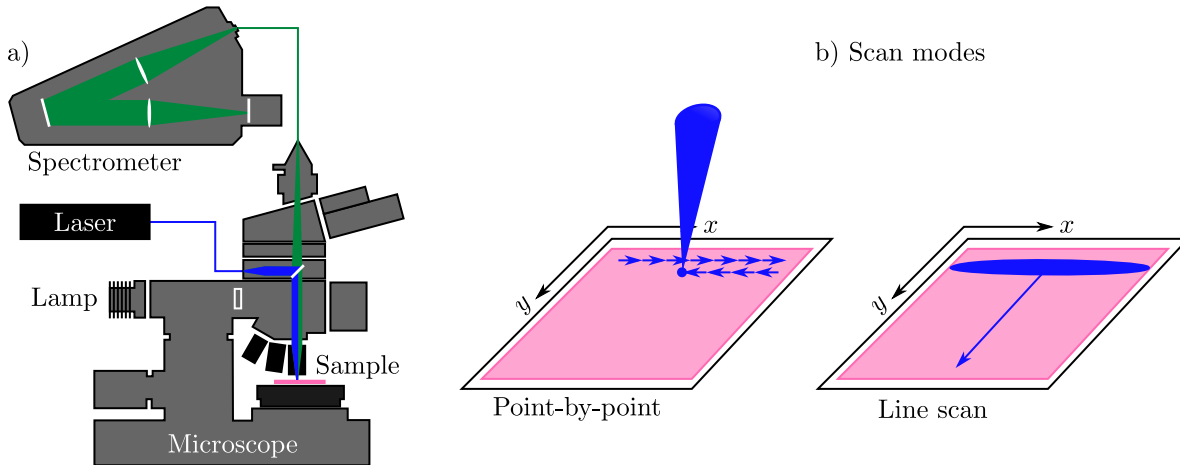

Fig. 2.6: a) Typical layout of a Raman microscope with a fiber-coupled laser source and spectrometer. b) Concept of laser spectroscopy mapping using point-by-point and line scan imaging.

2.2.2 Photoluminescence imaging

Photoluminescence (PL) imaging is a technique used to gather information about the sample being studied through the shape of its PL spectrum. The peaks in a PL spectrum are associated with recombination of excitons (as shown in Figure 1.7) or with band-to-defect level or band-to-band transitions. Figure 2.7a illustrates the PL spectrum of a WSe_2 monolayer excited by a green laser (532 nm), for which the peak can be described by its peak wavelength (λ_p), mass-center wavelength (λ_c), FWHM (which measures the broadness of the peak at half the maximum peak height), and intensity (which is the area under the PL spectrum). In case of a symmetric line spectrum, the λ_p and λ_c are identical, and only FWHM gives different information. However, PL spectrum tend to exhibit considerable asymmetry, indicating inhomogeneity of the system (even when the axis was changed from wavelength to energy).

The shape of a PL spectrum is characterized by its line shape, shown in Figure 2.7b, which can be Gaussian or Lorentzian, depending on the environment and the dynamics of

---

[3]It is an ideal tool for continuous inspection of flat panel displays, solar cells, or printed circuit boards that must have large, defect-free images.

the molecules involved. The Gaussian line shape is observed in solids where the excited molecule relaxes before incoherence becomes severe. The Lorentzian line shape, on the other hand, is observed in gases where rotation and collisions happen quickly. The line shape of liquids is a combination of both Gaussian and Lorentzian character, and can be modeled using a combination Gaussian-Lorentzian (G-L) profile or a more complex Voigt profile, each characterized by location, height, line width, and relative Lorentzian character [40].
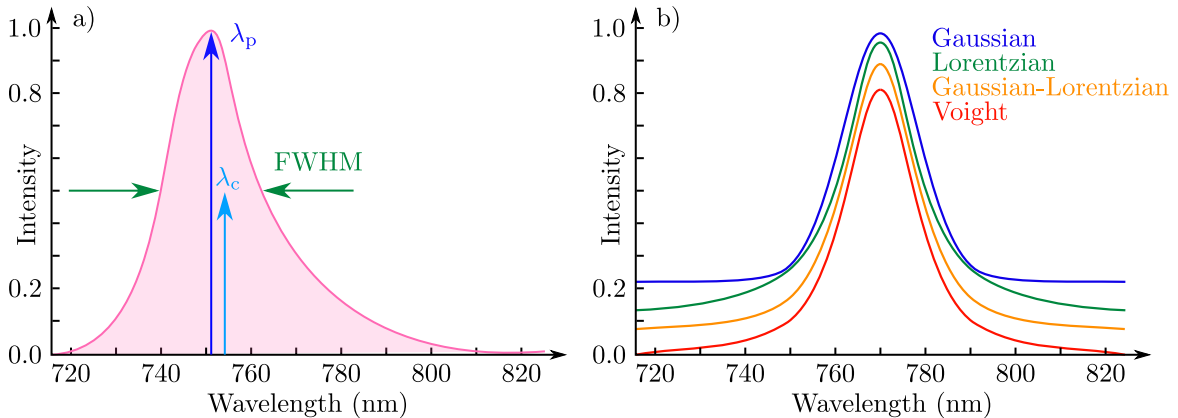

Fig. 2.7: a) Illustration of the PL spectrum of a WSe$_2$ monolayer measured by me with peak wavelength λ_p, mass-center wavelength λ_c, FWHM, and intensity (pink area under the curve). b) Comparison of the different types of lineshapes including Gaussian, Lorentzian, Gaussian-Lorentzian (G-L), and Voigt profiles with the same parameters.

In this diploma thesis, the experimental PL imaging will use a point-by-point scanning method (Figure 2.6b) to focus the laser light to a few-micrometer spot size and then scan it point-by-point in the x and y directions. The PL spectrum will be detected by an objective in the far-field. Moreover, the upcoming section will discuss the time-resolved photoluminescence mapping technique. Far-field PL imaging provides high spatial resolution that is limited only by the diffraction limit of the imaging system. On the other hand, near-field PL imaging provides sub-diffraction-limited spatial resolution, which enables the study of individual luminescent centers, but it requires specialized imaging probes and careful sample preparation to achieve high-quality images. More information on the near-field PL imaging method are in section 2.3.

2.2.3 Time-resolved photoluminescence imaging

Time-resolved photoluminescence (TRPL) imaging is an important technique for studying the kinetics of excitons and charge transfer in molecular processes, particularly in organic solar cells. Upon photon absorption, the primary excitation modes in organic solar cells are bound electron-hole pairs called excitons, which are localized to either the donor or acceptor phase [41], as shown in Figure 2.8b. The excitons need to move to the interface between the donor and acceptor phases of the bulk heterojunction (shown in Figure 2.8a)

to produce free-charge carriers. This process occurs after the excitons go through radiative and non-radiative decay. After reaching the interface, as shown in Figure 2.8c, an exciton in the donor (resp. acceptor) phase can dissociate into a charge-transfer (CT) state by transferring the electron (resp. hole) to the acceptor (resp. donor) phase, referred to as type I (resp. II) charge generation represented in Figure 2.8d [42]. The lifetime of the excited state, as measured by TRPL, is crucial for the efficiency of CT in organic solar cells. Increasing the lifetime of excitons increases the probability of dissociation into free-charge states, which enhances the charge generation yield of the cell. Therefore, TRPL imaging is an important technique to investigate the decay of excitons and charge transfer processes in organic solar cells, and to optimize their efficiency [43].
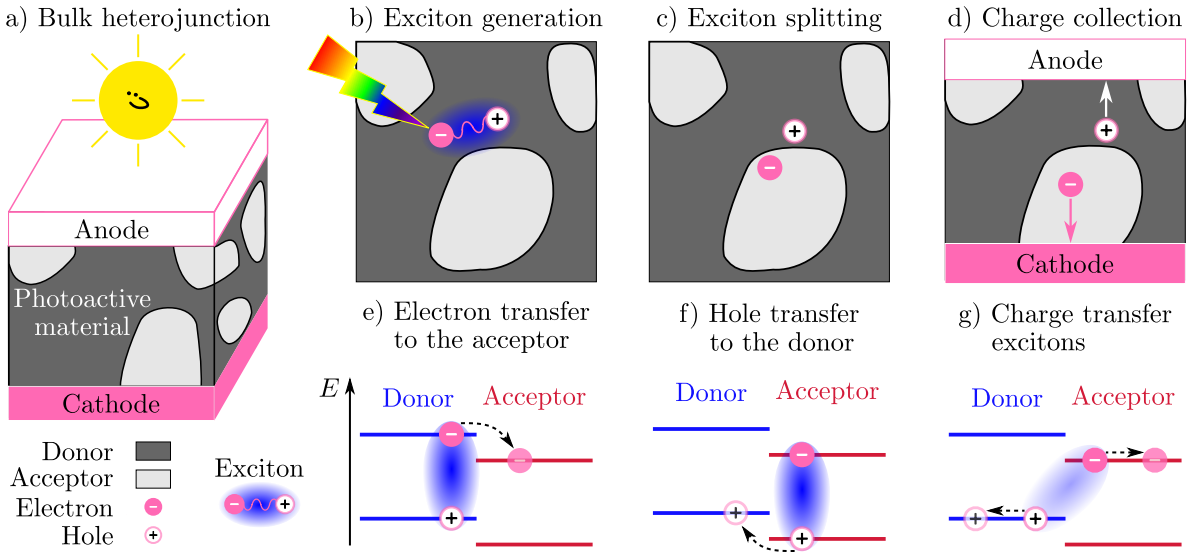

Fig. 2.8: a) Schematic diagram of bulk heterojunction structure, illustrating the processes involved in b) exciton generation process through photon absorption, c) exciton splitting to free charge carriers, and d) free charge transport toward electrodes. Simplified energy diagrams illustrate the photoexcitation of the e) donor and f) acceptor and g) the transfer of electrons and holes, respectively to generate CT excitons through both type I and type II charge generation processes in bulk heterojunction organic solar cells.

When an electron is excited, it remains in the excited state for a certain duration before recombination to the ground state through one of several possible decay pathways, including radiative and/or nonradiative processes. In an ensemble[4] description, the PL intensity decays over time according to the equation:

$$I(t) = I_0 \cdot \exp(-t/\tau), \tag{2.2}$$

where I_0 is the intensity at time $t = 0$ and t represents the time elapsed after the absorption process has ended. The lifetime τ of the excited state is determined by the the decay rates

---

[4]Ensemble is an idealization consisting of a large number of virtual copies of a system, considered all at once, each of which represents a possible state that the real system might be in [44].

of mean radiative (τ_{r}) and nonradiative (τ_{nr}) recombination times, given by the equation:

$$\frac{1}{\tau} = \frac{1}{\tau_{\mathrm{r}}} + \frac{1}{\tau_{\mathrm{nr}}}. \tag{2.3}$$

The values of $1/\tau_{\mathrm{r}}$ and $1/\tau_{\mathrm{nr}}$ represent the probabilities of the corresponding recombination pathways occurring per unit of time. The lifetime τ is therefore defined as the time required for the PL intensity to decrease to $1/e$ or $36.8\,\%$ of its initial value and is shown in Figure 2.9a [15, 19].
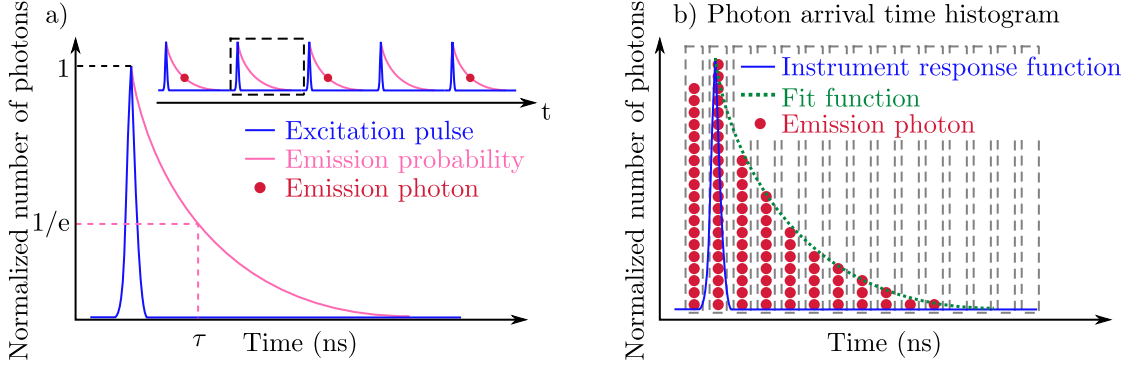

Fig. 2.9: a) TCSPC PL acquisition includes excitation pulse, single exponential decay curve, and lifetime τ defined at $1/e$ value. Inset shows detected PL photons at different time periods within multiple excitation pulses. b) Photon time of arrival histogram built from detection time of multiple PL photons; blue line represents IRF, and dotted green line represents fit function. Adapted from [45].

The photoluminescence lifetime of materials can be measured through various techniques such as time-correlated single photon counting (TCSPC), streak cameras, fluorescence upconversion, optical Kerr gate, phase fluorometry, and others. Among these, fluorescence lifetime imaging (FLIM) is the most commonly used technique for obtaining time-resolved fluorescence maps. FLIM is based on the decay of the fluorescence signal over time, and a short pulsed laser is used to excite the sample (short relative to the lifetime of the sample). Two microscopy imaging schemes used for FLIM are laser scanning microscopy (LSM) and wide-field illumination (WFI) microscopy, as shown in Figure 2.10. LSM systems offer higher contrast and spatial resolution, while WFI is often used for rapidly imaging large sample areas [45].

To measure the photoluminescence lifetime accurately at these time scales, high-speed electronics or nonlinear optical phenomena are required [46]. FLIM employs a commonly used method for TRPL mapping called TCSPC [47]. In TCSPC, a fast stopwatch measures the time between an excitation photon and the resulting emission photon, and this time defines each emission photon's time-of-arrival (Figure 2.9a). To measure this time accurately, a device called a time-amplitude converter (TAC) is used, which converts the photon time-of-arrival to an analog voltage that can be recorded. However, in conventional TCSPC, when photon count rates are high, the instrument's dead time causes most
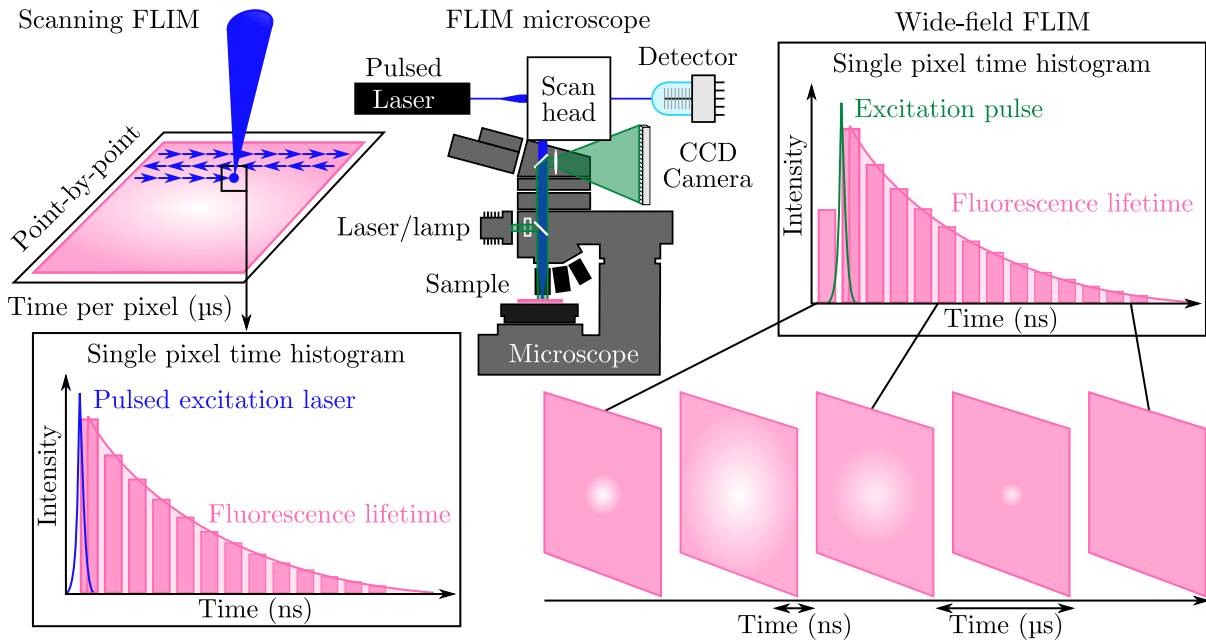
Fig. 2.10: Schematic of scanning and wide-field FLIM configurations with wide-field FLIM and scanning TCSPC FLIM imaging modalities. Scanning FLIM produces a photon arrival histogram for each pixel, limited by scanner speed, while wide-field FLIM requires repeated frame acquisitions to collect sufficient photons for a fluorescence decay histogram.

incoming photons to go unmeasured. This will lead to the pile-up effect where only the photons with shorter arrival times will be recorded per excitation pulse (see the inset in Figure 2.9a). This loss of photons with longer arrival times will create an incorrect photon histogram, leading to overall shortening of the measured fluorescence lifetime. To avoid these effects, a low photon count at the detector is desirable, ideally $< 10\%$ of the excitation repetition rate. This means the measurement needs many repetition times to build a complete picture of the fluorescence decay[5] [45].

However, one limitation of TCSPC is its slow acquisition speed, which motivates new techniques to speed up FLIM imaging, such as high-speed digitizers [48] (with subnanosecond sampling) and single-shot spectrally resolved ultrafast imaging, attaining 70 trillion frames per second [49]. These new techniques offer great promise for shorter FLIM acquisition times.

To improve the accuracy of FLIM data, a technique called curve fitting is used, which involves repeating the photon detection process thousands of times to create a distribution of fluorescence photon arrival times. This measured decay gives more accurate data to fit curves and analyze the fluorescence lifetime. The decay is calculated from the time-of-arrival of photons that are binned into a histogram, as shown in Figure 2.9b.

---

[5]TCSPC can also use reverse-TAC to measure the time between emission and the next excitation photon. Reverse-TAC is advantageous over forward-TAC in high repetition rate systems (50 to 100 MHz) with low photon count rates.

Time-domain FLIM measurements record the exponential decay of fluorescent molecules either directly (using gated detection or pulse sampling) or by calculating the decay from the time-of-arrival of photons that are binned into a histogram (Figure 2.9a-b). In contrast, frequency-domain FLIM represents each photon by its phase delay relative to the excitation photon. However, time-domain techniques have advantages over frequency-domain FLIM techniques, as they provide high accuracy of lifetime estimation and better signal-to-noise ratio (SNR) for weakly fluorescent samples [50].

FLIM is mainly used as an imaging technique in confocal microscopy for increasing optical resolution and contrast of a micrograph by means of using a spatial pinhole to block out-of-focus light in image formation [51]. It is advantageous for probing molecular environments of fluorophores[6] to inform on fluorophore behavior that cannot be elucidated with intensity measurements alone. However, recently it has found to be useful for imaging the dynamics of excitons in photovoltaics, mainly efficient perovskite (which are explained in section 3.3.2) solar cells. Figure 2.11a shows the basic principle of obtaining the lifetime from each pixel of the studied are, for which the expontential curve is fitted and the lifetime is calculated afterwards.

Cacovich *et al.* [52] (Figure 2.11b-d) investigated charge recombination and losses in inverted solar cells with conversion efficiency greater than $23\,\%$ using WFI FLIM. They achieved this by introducing two large organic A-site cations, namely 4-chloro-phenylethylammonium iodide (Cl-PEAI) and 4-fluoro-phenylethylammonium iodide (F-PEAI), at the interfaces of the perovskite absorber with both the hole transport layer (HTL) and electron transport layer (ETL). This significantly reduced non-radiative recombination, and WFI FLIM confirmed the uniformity of the deposited cations over the perovskite surface at the micrometer scale. The researchers studied three different types of cells, as shown in Figure 2.11b-d: a reference cell (Figure 2.11b) and devices with dual interfacial modification by F-PEAI (Figure 2.11c) and Cl-PEAI cations (Figure 2.11d). The histograms in Figure 2.11e indicate that the difference between the reference and modified samples in terms of non-radiative recombination is statistically significant. Notably, the time-resolved analysis also revealed that high non-radiative recombination is responsible for the fast decay of the reference cell.

Bu *et al.* [53] (Figure 2.11f-g) studied the grain boundaries effect in perovskite films and its defect passivation using LSM FLIM. They achieved this by introducing a suitable amount of methylammonium chloride (MACl) additive and excess of lead iodide (PbI_2), which improved the morphology and stabilized the phase of the FA-based perovskite. To visualize the defect passivation effect achieved, they used scanning electron microscope (SEM) images (insets in Figure 2.11f-g) and LSM FLIM, which showed that the excess PbI_2 passivated the grain boundaries effectively. The post-treatment of the perovskite film with organic salts (dodecylamine hydrobromide, DABr) greatly enhanced the PL lifetime and improved the morphology of the film. These results indicate that this series

---

[6]A fluorescent chemical compound that can re-emit light upon light excitation.

of processes can effectively passivate the perovskite grains and/or surface to reduce the trap-induced or non-radiative recombination in the films, which would be beneficial to improve the performance of the corresponding devices. The corresponding crystallinity and morphology changes are shown by SEM images in insets of the Figure 2.11f-g.
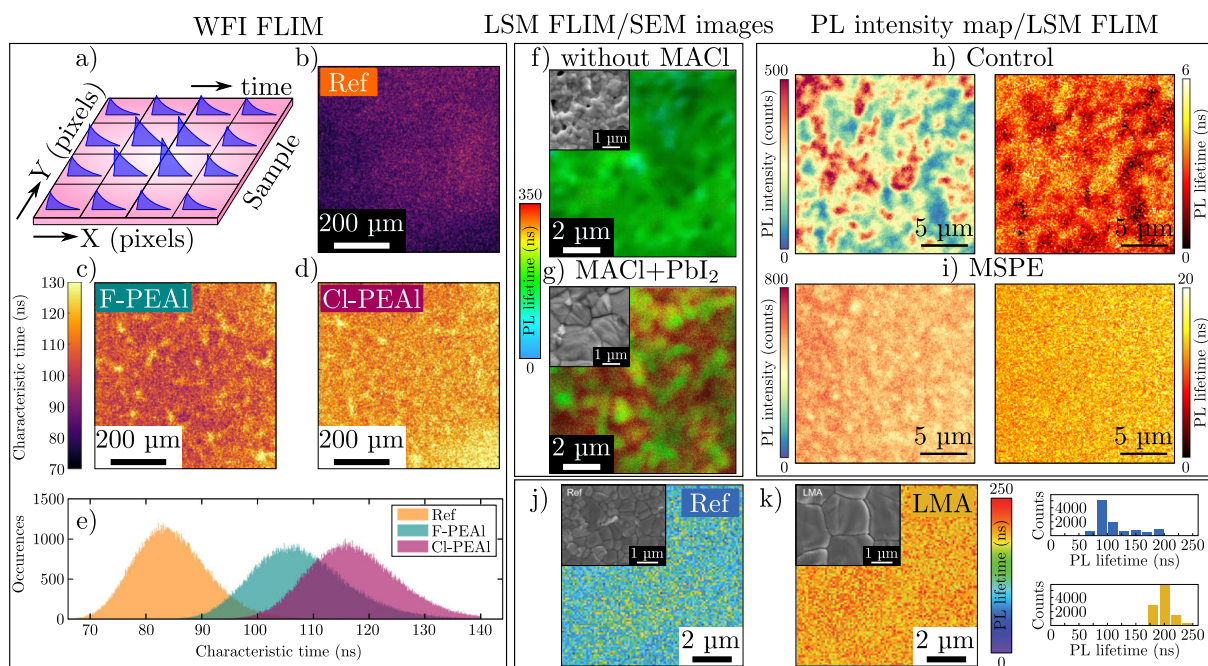

Fig. 2.11: Different studies on perovskite materials using various FLIM techniques. a) The basic principle for obtaining time-resolved photoluminescence maps, where each pixel is fitted with an exponential function to determine the lifetime of the exciton. b)-d) Cacovich *et al.* used WFI FLIM to investigate charge recombination and losses in inverted solar cells with conversion efficiency greater than 23 %, by introducing two large organic A-site cations (F and Cl) at the interfaces of the perovskite absorber. Reproduced from [52]. Copyright 2022 Springer Nature America, Inc. f)-g) Bu *et al.* investigated the impact of grain boundaries on perovskite films and demonstrated their successful passivation using LSM FLIM and SEM. Reproduced from [53]. Copyright 2022 Springer Nature America, Inc. h)-i) Sun *et al.* conducted a study on perovskite LEDs (mixed with multifunctional molecule MSPE) that exhibited exceptional performance at high brightness using confocal PL and LSM FLIM microscopy. Reproduced from [54]. Copyright 2023 Springer Nature America, Inc. j)-k) Li *et al.* used LSM FLIM to investigate the benefits of liquid medium annealing (LMA) technology in the development of high-quality hybrid perovskite materials for perovskite solar cells (PSCs). Reproduced from [55]. Copyright 2021 American Association for the Advancement of Science.

Sun *et al.* [54] (Figure 2.11h-i) conducted a study on perovskite LEDs that exhibited exceptional performance at high brightness. They achieved this by introducing a multifunctional molecule, which simultaneously removes non-radiative regions in the perovskite films and suppresses luminescence quenching of perovskites at the interface

with charge-transport layers. The multifunctional molecule used in this study is 2-(4-(methyl-sulfonyl)phenyl)ethylamine (MSPE), designed to manipulate the optoelectronic, crystal, and morphological properties of 3D cubic phase formamidinium lead triiodide ($FAPbI_3$) perovskites. The perovskite without MSPE is referred to as the "control", while the perovskite with MSPE is referred to as "MPSE". Confocal PL and LSM FLIM microscopy were used to demonstrate the improvements in the perovskite films. The left map in Figure 2.11h-i shows the PL intensity map, while the right map represents the PL lifetime map. MSPE improves the crystallinity and photoluminescence efficiency and induces homogeneous emission by removing non-radiative dark regions in the perovskite films. The control films have significant spatial variation in PL intensity on the length scale of micrometres, and the dark regions in the control samples correlate with reduced PL lifetime, indicating that these dark regions contain a higher concentration of defects serving as non-radiative centres. On the other hand, the MSPE films show much more homogeneous intensity and a uniformly long lifetime on the same length scale. The absence of defect-containing dark regions in MSPE films is consistent with the improved overall photoluminescence quantum efficiency and carrier lifetime relative to the control films.

Li *et al.* [55] (Figure 2.11j-k) used LSM FLIM to investigate the benefits of liquid medium annealing (LMA) technology in the development of high-quality hybrid perovskite materials for perovskite solar cells (PSCs). They found that LMA created a robust chemical environment and constant heating field to modulate crystal growth over the entire film, resulting in films with high crystallinity, fewer defects and overall film homogeneity. The resulting PSCs had a stabilized power output of certified 23.7 % and maintained 95 % of their initial power conversion efficiency (PCE) after 2000 hours of operation. Compared to traditional annealing methods (referred to as "Ref"), LMA resulted in a significantly higher overall lifetime of perovskite films (196.04 ns vs. 109.29 ns). The lifetime distribution of LMA films was concentrated in the range of $\sim$ 180 to 240 ns, while Ref exhibited a much broader distribution from 30 to 190 ns. Insets in the figures show SEM images of Ref and LMA samples, highlighting the differences in film morphology and quality (Figure 2.11j-k). SEM images showed that LMA-prepared perovskite films had a larger grain size of $2.25 \pm 0.66\,\mu m$, while Ref films had a smaller grain size of $0.85 \pm 0.25\,\mu m$.

In summary, TRPL imaging is a useful technique for studying the kinetics of excitons and charge transfer in organic solar cells. The lifetime of excited states, as measured by TRPL, is critical for the efficiency of charge transfer in organic solar cells. The decay of excitons and charge transfer processes can be investigated through TRPL imaging, which can help optimize their efficiency. The photoluminescence lifetime of materials can be measured using techniques such as time-correlated single photon counting (TCSPC), fluorescence upconversion, optical Kerr gate, phase fluorometry, and fluorescence lifetime imaging (FLIM). FLIM is the most commonly used technique for obtaining time-resolved fluorescence maps, and two microscopy imaging schemes used for FLIM are laser scanning microscopy (LSM) and wide-field illumination (WFI) microscopy.

2.3 Near-field optical microscopy

The diploma thesis centers around the application of near-field optical microscopy (NFOM) to explore nanoscale phenomena that exceed the diffraction limit of conventional optical microscopy. In conventional far-field spectroscopy and imaging, distinct and distinguishable Airy patterns are obtained from objects separated by distances larger than the Rayleigh criterion [56]. However, this diffraction limit, defined as $\lambda/2$NA (where λ represents the wavelength of light and NA denotes the numerical aperture of the lens), can be surpassed by employing NFOM techniques that leverage near-field (NF) effects.

The concept of high-resolution NF imaging was first proposed by E. H. Synge in 1928 [57], suggesting the use of a small aperture in a thin metal film to transmit light and illuminate a sample placed in close proximity. However, practical implementation of this idea faced technological challenges related to nano-fabrication, nano-precision positioning, and low detector sensitivity. It was not until the advent of scanning probe microscopy (SPM) techniques about 60 years later [58, 59] that the original concept of NF imaging became a reality.

One of the approaches within NFOM is near-field scanning optical microscopy (SNOM), which employs a metal-coated optical fiber probe with a nano-aperture (diameter of $\approx 100\,\text{nm}$) to detect and illuminate NF signals on sample surfaces [60]. With its high spatial resolution surpassing the diffraction limit, SNOM has enabled groundbreaking works across various disciplines, including physics [60], chemistry [61], biology [62], and materials sciences [63]. However, SNOM has limitations related low sensitivity, as the transmission intensity through the SNOM probe decreases inversely with the fourth power of the aperture size [64]. Additionally, problems associated with optical fibers, such as wavelength-selective optical loss, polarization modification, and dispersion, restricted the broad applications of SNOM.

To overcome these challenges, an inverse approach utilizing NF scattering, known as apertureless SNOM or scattering-type SNOM (s-SNOM), was proposed [65], utilizing NF scattering. This technique provided $< 10\,\text{nm}$ spatial resolution, but weak NF scattering signals remained a challenge, due to potential deterioration of image contrast and spatial resolution caused by the far-field background. The integration of plasmonic nano-materials (such as Au or Ag in the visible frequency range) and plasmonic tips in s-SNOM allowed for stronger NF signals, enabling various applications such as tip-enhanced Raman spectroscopy (TERS) [66, 67] and tip-enhanced photoluminescence (TEPL) spectroscopy. TEPL spectroscopy provides insights into the electronic properties of semiconducting materials at the nanoscale. Recently, TEPL approach further advanced to tip-enhanced strong coupling (TESC) spectroscopy using plasmonic tip-cavity at room temperature [68]. In brief, historical development in NF microscopy is summarized in Figure 2.12, for which the aim is on a-SNOM and its application.

Within the scope of this diploma thesis, the primary focus is on a-SNOM.This powerful NF technique allows for the investigation of nanoscale structures and the extraction of
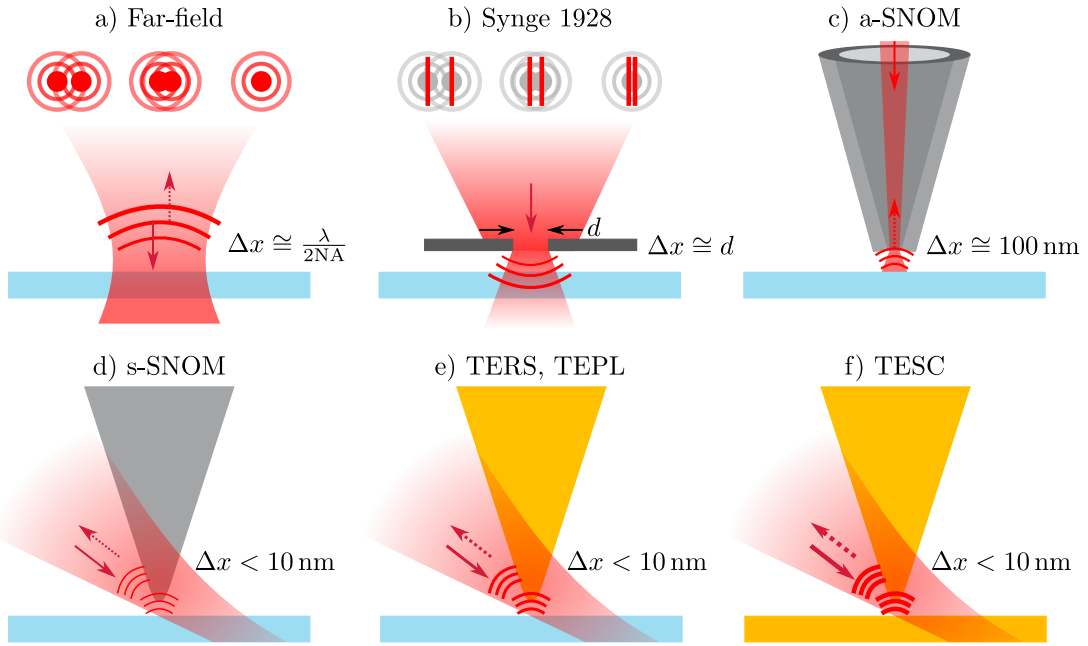
Fig. 2.12: Experimental schematic representations illustrating the spatial resolution (Δx) of different microscopy techniques: a) far-field optical microscope, b) Synge's theoretical proposal, and c) a-SNOM. Additionally, schematics demonstrating d) s-SNOM, e) TERS, TEPL, and f) TESC spectroscopy. Adapted from [69].

valuable information beyond the diffraction limit. In a-SNOM, a conical optical fiber with a sub-diffraction limit aperture is scanned relative to the sample surface, enabling highly detailed imaging of nanoscale structures and phenomena. The resolution of a-SNOM is determined by the size of the aperture on the optical fiber tip.

2.3.1 Aperture-type scanning near-field optical microscopy (a-SNOM)

A-SNOM is a powerful technique used in nanoscale imaging. It overcomes the limitations of conventional far-field microscopy by detecting the distribution of NF electromagnetic radiation. This is achieved by using a conical optical fiber with a small aperture, as shown in Figure 2.13a, which enables a-SNOM to achieve superior spatial resolution [70].

A-SNOM involves scanning the sample surface with a conical optical fiber that emits NF light, resulting in photon scattering. The resolution depends on the aperture diameter, NA, and collection optics, enabling detailed imaging of nanoscale structures [71]. It is a surface-selective technique, utilizing a highly confined aperture as a noise-free light source, unlike apertureless techniques with significant background noise [70]. A-SNOM employs contrast mechanisms like absorption, phase shifting, and local excitation of photoluminescence PL, and the collected light (filtered through a filter) can be directed to a suitable detector, using standard inverted optical microscopes for light collection.

Figure 2.13b illustrates the classical a-SNOM, for which a small area of the sample surface is illuminated using an aperture probe. The sample is placed on a substrate that

captures all the radiation emerging from the interaction zone between the probe and sample, directing it to the far-field. SNOM routinely achieves resolutions of $50 - 100\,\text{nm}$, which is at least 5 to 10 times better than a standard scanning confocal optical microscope with a $1.4\,\text{NA}$ [71].
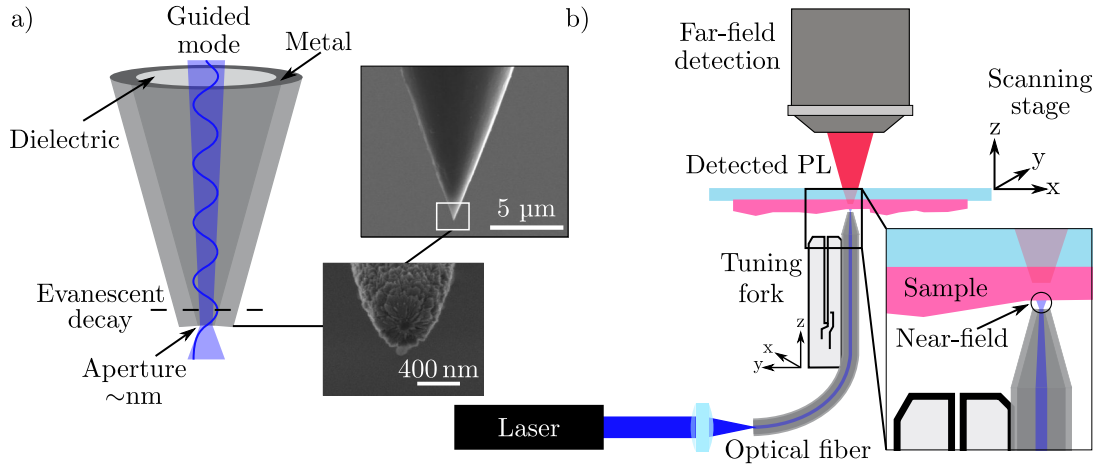

Fig. 2.13: a) Illustration of the successive cut-off of single guided mode and the exponential decay of the field towards the aperture in a conic, metal-coated waveguide known as a-SNOM probe. The inset shows detailed electron microscope image of such an a-SNOM probe, taken from [72]. b) Typical setup for NF optical microscope operating in illumination (transmission) mode. The probe is positioned within the NF distance of the sample using tuning fork shear force feedback. The light interacts with the sample, exciting the PL, collected by a microscope objective that is aligned with respect to the fiber axis.

Currently, most a-SNOM systems utilize a technique similar to non-contact atomic force microscopy (AFM) called shear force feedback. This method involves vibrating a fiber probe (through the tuning fork) at one of its mechanical resonances perpendicular to the sample surface, ideally at amplitudes below $1\,\text{nm}$. During the final approach ($0 - 20\,\text{nm}$), shear forces come into play, causing a detuning of the resonance frequency relative to the driving oscillator, resulting in decreased amplitude and a phase shift [71].

To achieve optimal performance in a-SNOM, it is essential to utilize an optical probe with a small aperture diameter and ensure sufficient light intensity. This can be accomplished by enhancing the overall light throughput and improving the damage threshold of the metal coating. Standard optical fibers are commonly employed for the convenient delivery of light in proximity to the aperture [71].

The transmission coefficient of an aperture probe, defined as the power of coupled light divided by emitted light power, depends on factors such as the material, tip diameter, and narrowing angle [70]. Novotny and Hafner's study [73] examined the influence of cone angle and aperture diameter on power transmission efficiency. Smaller apertures and specific taper angles resulted in lower transmission. Optimizing the metal coating improves the aperture probe's brightness [74, 75]. Moreover, depositing a thin layer of Al_2O_3 on metallic structures enhances thermal stability. Notably, reducing the aperture

size below $50 - 100\,\mathrm{nm}$ has disadvantageous effects, while larger cone angles significantly enhance the overall transmission coefficient of tapered waveguide structures [76].

Tugchin *et al.* [77] explored plasmonic and photonic modes in a-SNOM, revealing their roles in optical detection and excitation. Plasmonic modes reach the tip aperture without cutoff, and coupling between modes occurs for core radius below 600 nm. The fundamental plasmonic mode dominates NF interaction, highlighting the importance of plasmonic fields in confining light in subwavelength regions.

2.3.2   Near-field excited photoluminescence mapping

NF excited PL mapping using a-SNOM (shown in Figure 2.13b) enables high-resolution imaging of the local density of optical states and carrier recombination rate within a sample. This technique is valuable for studying the chemical composition, molecular structure, and dynamic properties of nanostructures. Metamaterial-based superlenses can further enhance resolution by bringing the objective lens close to the object [78].

Lee *et al.* [79] focused on visualizing structural defects in monolayered molybdenum disulfide (MoS_2) using optical methods, as shown in Figure 2.14a-c. They found that conventional (confocal) PL imaging had limitations in identifying nanosized defects and understanding the origin of PL signal variations at grain boundaries (GBs). Near-field PL imaging, however, allowed them to identify nanosized line defects and adlayer defects in chemically vapor-deposited (CVD) monolayered MoS_2. The study revealed that the reduced PL on GBs was attributed to local physical damage rather than localized states. This research highlights the potential of NF PL imaging for characterizing structural defects in monolayered MoS_2 and other two-dimensional materials.
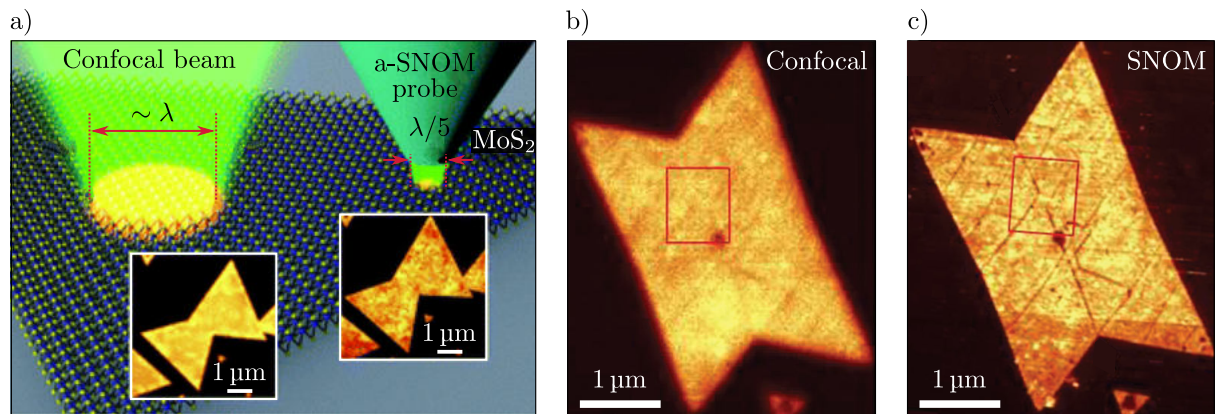

Fig. 2.14: a) Confocal and SNOM PL images of butterfly-shaped monolayered MoS_2. b) Confocal PL image and c) SNOM PL image of monolayered MoS_2. Reproduced from [79]. Copyright 2015 Royal Society of Chemistry.

Bao *et al.* [80] introduced the campanile probe (shown in Figure 2.15a), a nano-optical device with exceptional capabilities, for subwavelength nanospectroscopic imaging. This probe enables efficient far-field to NF coupling, ultralarge field enhancement,

nearly background-free imaging, and broadband operation. Using the campanile probe, they conducted hyperspectral imaging of local optoelectronic properties in indium phosphide nanowires (InP NWs), revealing PL heterogeneity and providing insights into charge recombination from trap states. Compared to conventional confocal microscopy, the campanile probe exhibited superior optical resolution, as demonstrated in Figure 2.15b-c, where the gap size of the campanile tip allowed for enhanced resolution along the nanowire. Cathodoluminescence[7] measurements on InP NWs offer comparable resolution but fail to detect spatial variation due to trap state filling [82]. The campanile probe overcomes this limitation, providing enhanced optical resolution for nanowire imaging.
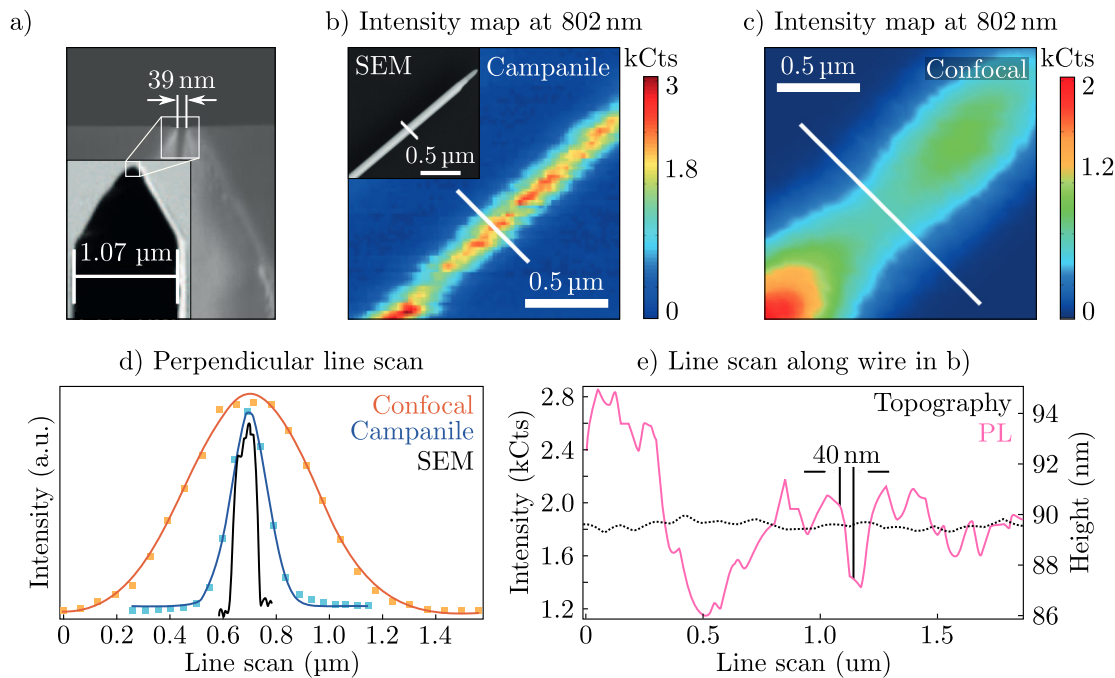

Fig. 2.15: Nano-optical hyperspectral PL mapping of InP NWs. a) SEM image displays the campanile probe with a 39 nm gap at its apex. The intensity maps obtained by the b) campanile tip and c) confocal microscopy, with the inset in b) showing SEM image of an InP NW. The NF map obtained by the campanile tip b) exhibits significantly higher spatial resolution compared to the confocal map, as demonstrated by the line scan across the wire shown in d). The units of intensity are arbitrary (a.u.). e) A line scan along the wire length in b) demonstrates a spatial resolution of approximately 40 nm, whereas the topographic line scan exhibits negligible variations. Reproduced from [80]. Copyright 2012 American Association for the Advancement of Science.

In summary, a-SNOM combines the strengths of scanned probe technology and optical microscopy, offering a promising approach for investigating nanostructures at the subwavelength scale.

---

[7]Cathodoluminescence is the emission of light by a luminescent material when it is struck by high-energy electrons, allowing to study optical properties and emission behavior at a nanoscale level [81].

3 Results and discussion

This chapter presents and discusses the experimental setup used in the study, with a primary focus on its development and the subsequent examination of samples. The first section provides a detailed overview of the equipment and instruments used in this work, including an analysis of the lasers and spectrometer employed in the setup. It specifically highlights the function of the spectrometer and avalanche photodiode. The section also covers the measurement of photoluminescence (PL) and time-resolved PL (TRPL) spectra using the far-field approach on a test sample. Subsequently, the final setup used for near-field (NF) excited PL mapping is presented. The second section, "Data analysis and interpretation," outlines the process of data collection using different software programs and the communication between the program and hardware. It also explains how the collected data was analyzed and interpreted. The third section, "Samples," provides thorough analysis of the samples used in the study. Lastly, the fourth section, "Near-field time-resolved photoluminescence measurements," outlines the attempt to obtain TRPL data or maps using the NF approach. In summary, this chapter offers a comprehensive overview of the experimental setup, the data collection and analysis process, and the results obtained from the study.

3.1 Experimental setup

The experimental setup utilized in the study consisted of various equipment and instruments. It involved the use of lasers, a spectrometer, an avalanche photodiode (Figure 3.1a-e), and other components for data collection and analysis. The lasers employed included picosecond diode lasers (PIL 040-FS and PIL 051-FS) and a femtosecond Ti:Sa laser (Chameleon Ultra II). The picosecond diode lasers from NKT Photonics [83] offered flexibility and ease of use, while the femtosecond Ti:Sa laser from Coherent [84] provided a wider range of tunability and higher power output. Technical specifications of the lasers, along with their advantages, are detailed in Table 3.1.

Tab. 3.1: Technical specifications of the lasers utilized in the experiment.

Model name	Wavelength (nm)	Pulse width	Peak power (W)	Average power (mW)	Repetition rate
PIL 040-FS	407	$100\,\mathrm{ps}$	3	$5^{1)}$	$1\,\mathrm{kHz} - 40\,\mathrm{MHz}$
PIL 051-FS	510	$100\,\mathrm{ps}$	3	$5^{1)}$	$1\,\mathrm{kHz} - 40\,\mathrm{MHz}$
Chameleon Ultra II	$680 - 1\,080$	$140\,\mathrm{fs}$	$> 300\,000^{2)}$	$> 3\,500^{2)}$	$80\,\mathrm{MHz}$

1) At maximum repetition rate.

2) Specified at peak tuning range.

The spectrograph used in the setup was the Shamrock 303i from Oxford Instruments, coupled with the iDus 420 charge coupled device (CCD) camera (Figure 3.1c). This spectrograph-camera system allowed quick analysis of spectra without the need for scanning across different wavelengths. The advantages of the CCD camera included its wide wavelength range, ranging from 395 nm to 950 nm, and high signal-to-noise ratio, achieved through low-temperature operation (approximately $-60\,°C$).

For TRPL measurements, the setup employed an avalanche photodiode SPCM-AQRH from Excelitas Technologies and a TimeTagger 20 voltage pulse counter from Swabian Instruments (Figure 3.1d-e). The avalanche photodiode is used to detect single photons over the wavelength range of 400 nm to 1064 nm, generating a TTL-level[1] pulse for each detection. This TTL signal was then recorded by the TimeTagger 20, enabling time-correlated photon counting measurements (see section 2.2.3 and Figure 2.9 for more details).
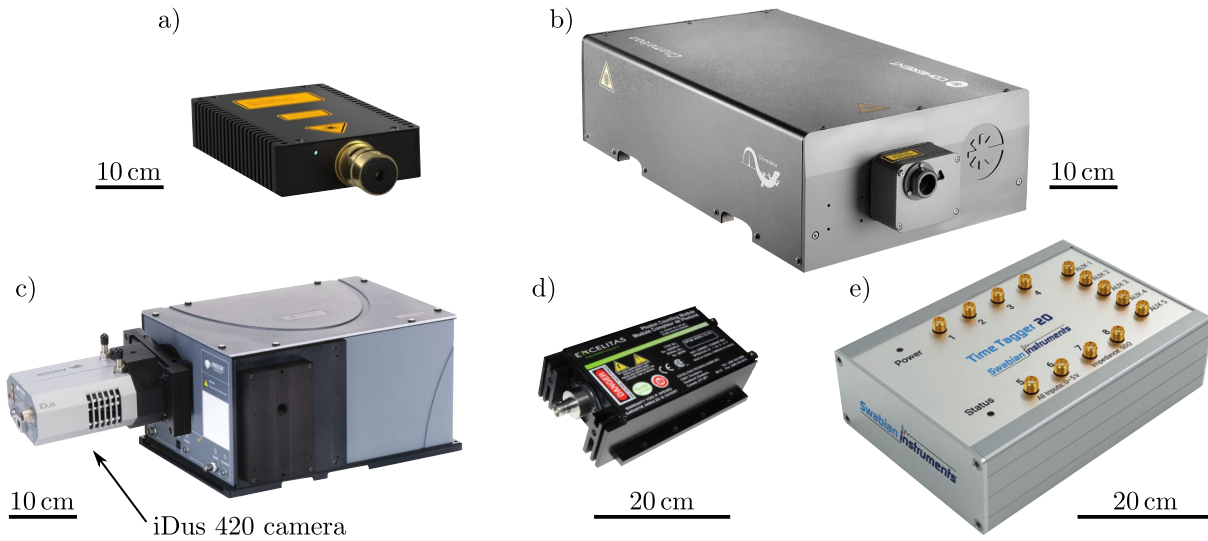

Fig. 3.1: Instruments used in the setup: a) Picosecond diode laser from company NKT Photonics and b) femtosecond Ti:Sa laser from company Coherent called Chameleon Ultra II. Taken from [83, 84]. c) Shamrock spectrograph 303i equipped with CCD camera iDus 420 from Oxford Instruments [85, 86]. d) Avalanche photodiode SPCM-AQRH-64 from Excelitas Technologies [87], and e) TimeTagger 20 from Swabian Instruments [88].

Time-correlated photon counting differs from pure photon counting in that the counter also receives a signal from the excitation laser triggered in pulsed mode. The laser signal arrives shortly before the excitation pulse emission, triggering the counter stopwatch and recording the incoming voltage pulses. These pulses are plotted on a time histogram according to the delay with which they arrived from the beginning of the measurement. The measurement is repeated until a sufficiently significant signal-to-noise ratio is obtained. For this model, the dead time is 42 ns, which limits the temporal resolution of

---

[1]TTL is a logical signal, which stands for "transistor-transistor logic", with voltage of 5 V for logic one and approximately 0 V for logic zero, used in digital circuits. In this experiment, the TTL signal is generated by the avalanche photodiode and represents the detection of a single photon.

the measurement. The dead time of the TimeTagger 20 is $6\,\text{ns}$. In the context of this experiment, the dead time refers to the minimum amount of time required for the voltage pulse counter to reset before it can record the next incoming pulse.

To facilitate communication between the instruments and control the experimental setup, a program was developed by Ing. Daniel Šimek and integrated into a single C# program. Additional functions related to PL and TRPL mapping were incorporated by Bc. Jan Čecháček into the program. Initially, a far-field setup was assembled to verify the communication and measure PL and TRPL spectrum. This setup involved a blue pulsed picosecond diode laser, mirrors, lenses, a dichroic mirror, and a fiber. The obtained PL and TRPL of $CsPbBr_3$ (further discussed in 3.3) are presented in Figure 3.2a-b, demonstrating agreement with the literature [89]. The TRPL data were fitted with a single exponential function according to equation 2.2, resulting in a calculated mean exciton lifetime of $\tau = 9.18\,\text{ns}$ and corresponding amplitude being $I_0 = 1830$.
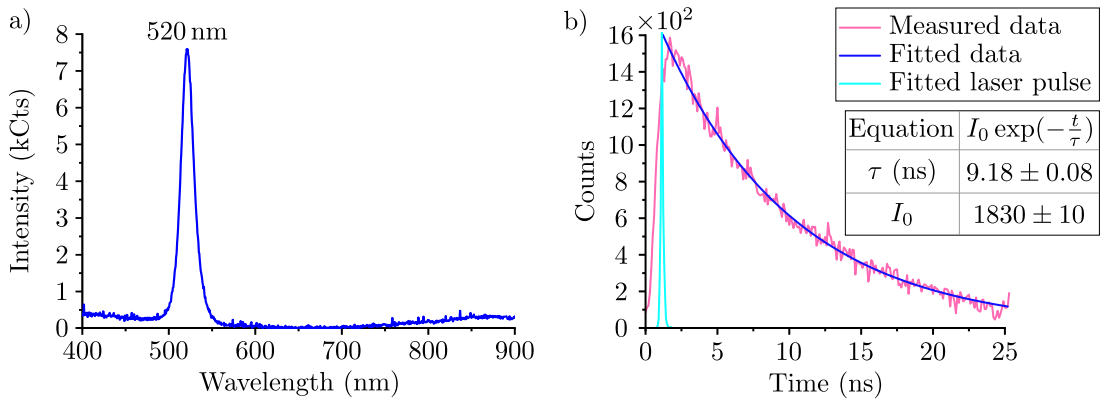

Fig. 3.2: Far-field excited a) PL and b) TRPL measurements of $CsPbBr_3$ sample, obtained using blue picosecond diode laser ($407\,\text{nm}$). The laser pulse was fitted into the graph using the data provided by the manufacturer [83].

The central focus of this thesis was to develop and assemble a new setup for NF excited PL mapping, with a particular emphasis on its versatility and modularity. The setup, depicted in Figure 3.3, was carefully designed and incorporated essential components such as interchangeable lasers (or other sources of light), single-mode optical fibers, mirrors, lenses, a tuning fork, and the Litescope AFM module from NenoVision [90].

To ensure reliable and efficient communication between the Litescope and the program, a collaborative experiment was conducted with Ing. Peter Kepič, focusing specifically on investigating the properties of antimony trisulfide (Sb_2S_3). Sb_2S_3 is a highly promising material with tunable nanophotonic applications due to its ability to undergo a non-volatile phase change between its amorphous and crystalline states. This material exhibits low absorption in the visible spectrum, enabling a significant refractive index contrast ($\Delta n \approx 1.1$ at 633 nm) during the phase transition [91]. Understanding the behavior of Sb_2S_3 is crucial for optimizing its performance in various applications.
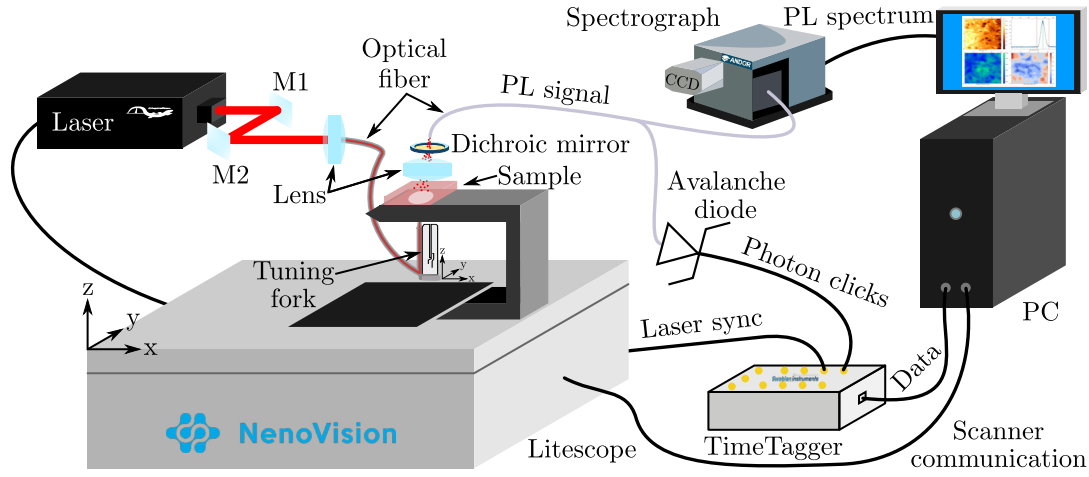
Fig. 3.3: Schematic of the modular setup used for NF excited PL measurements using the spectrograph fitted with CCD camera or TRPL measurements using avalanche photodiode connected to the TimeTagger.

The Sb_2S_3 sample, fabricated using pulsed laser deposition by Ing. Peter Kepič, was examined using a far-field approach and reflection geometry. Illumination was done using a halogen lamp, and a precise focusing and collection of the reflected light were achieved using a $50\times$ zoom objective lens. This setup allowed for obtaining a reflectivity map by dividing the collected signal at the desired wavelength (633 nm) by a reference signal. The reflectivity map, shown in Figure 3.4a, was obtained by scanning the sample (point-by-point) over a 50×50 µm^2 area with micron step size.
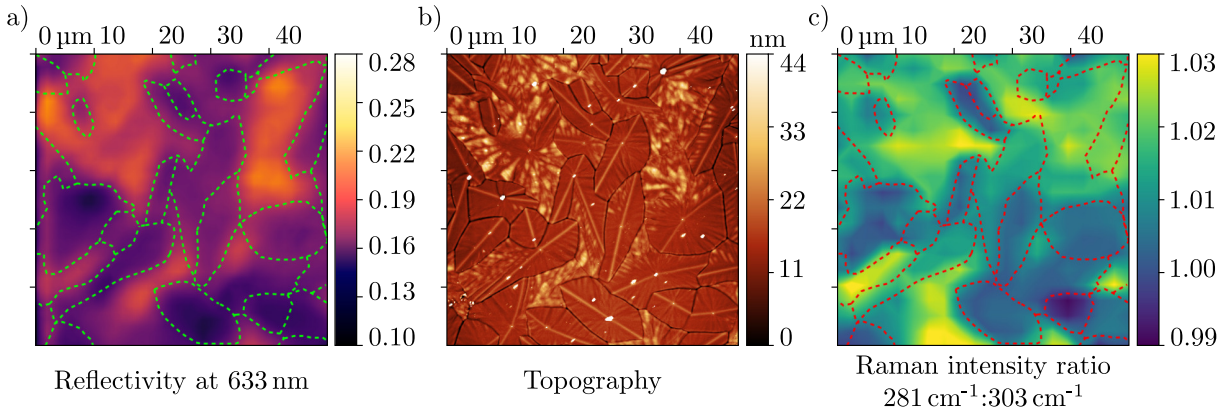

Fig. 3.4: Characterization of the Sb_2S_3 sample, showing a) reflectivity map at 633 nm, b) AFM image, and c) Raman intensity map for the ratio of 281 cm^{-1}:303 cm^{-1}. The correlation between the different phases is indicated by green dashed lines in a) and red dashed lines in c), which were extracted from map in b).

To gain further insights into the different phases of the Sb_2S_3 material observed in the reflectivity map, additional characterization techniques were employed. AFM imaging provided a detailed surface topography of the sample, while a Raman intensity map was generated using the ratio of 281 cm^{-1}:303 cm^{-1}, as proposed by Gutiérrez *et al.* [92]. These

complementary measurements, depicted in Figure 3.4b-c, allowed to establish correlations between different phases, as indicated by the green and red dashed lines. This comprehensive approach served to validate the seamless and accurate communication between the Litescope and the program, enabling to gain a better understanding of the properties of Sb_2S_3 for potential nanophotonic applications.

A noteworthy feature of the setup is the integration of a metal-coated conical tip, attached to the tuning fork, effectively transforming the Litescope into an aperture-type scanning near-field optical microscope (a-SNOM). This integration provides precise NF probing capabilities in both amplitude and frequency modes. By efficiently coupling the laser to the coated optical tip, it becomes possible to generate the NF excited PL signal. Subsequently, the collected PL signal is analyzed using either a spectrograph equipped with a CCD camera or an avalanche photodiode in conjunction with a time-correlated system. This unique configuration allows for simultaneous NF probing and PL excitation of the sample, enabling the creation of comprehensive in-situ maps that include topography, PL intensity, and TRPL maps. Notably, all of these maps can be obtained from a single scan, highlighting the remarkable capabilities of the setup.

3.1.1 Challenges of a-SNOM probes

The a-SNOM probes used in the measurements were commercially purchased. They were made using a Nufern 460HP single-mode optical fiber, and the probe tip was coated with a layer of Al (70 nm) and a sublayer of Cr (20 nm). The aperture, uncoated by Al, had a diameter of approximately 100 ± 30 nm. The fiber angle was around 20 degrees, and the the tip of the probe was formed through chemical etching. Its length without protective coating measured $7 - 8$ mm, with the overall fiber length measuring approximately 2 m.

However, the process of attaching the a-SNOM fiber to a tuning fork presented significant challenges, primarily due to the strict requirement of avoiding any contact with the fiber tip throughout the attaching and manipulation stages. To ensure the stability of the tip without compromising its integrity, the probe was connected to the tuning fork at two strategic points, as depicted in Figure 3.5a.

Additionally, several difficulties were encountered, resulting in substantial waste of time. Various types of glues and epoxy adhesives were tested following the attachment process. The most favorable outcome was achieved with a super glue [93], notable for its suitable viscosity to adhere to the desired location and rapid drying time, enabling subsequently covering the probe during the additional curing period. The curing process itself required at least half a day, ideally a full day, to ensure the tuning fork's mechanical resonance stability during the subsequent approach and measurements utilizing a-SNOM.

Once the initial setup procedures were completed, the probe connected to the tuning fork was carefully inserted into the SNOM head. Following these critical steps, a laser was coupled into the opposite end of the fiber, necessitating the alignment of the entire setup and initiating the approach process. After successfully approaching the sample in
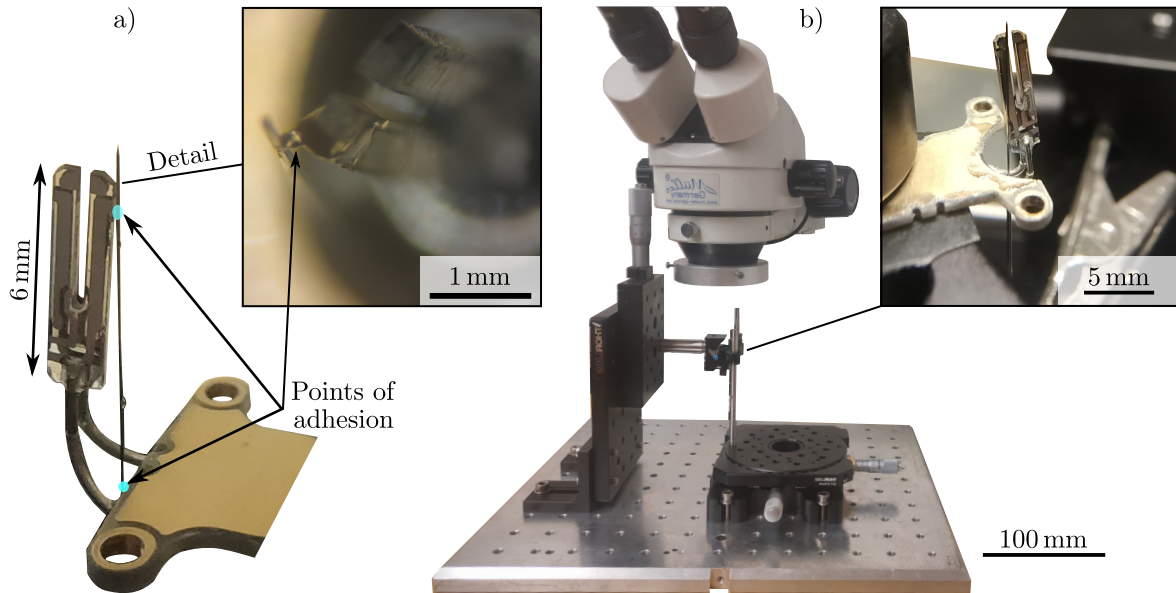
Fig. 3.5: a) The SNOM probe is attached to the tuning fork, with an illustration (blue circle) highlighting the two areas where the glue was applied to attach the probe. b) Dedicated station designed for attaching SNOM probes to the tuning fork.

the near-field region, realignment of the entire setup was performed, primarily involving movements with the detection fiber to optimize the signal strength. It is worth noting that the time-consuming nature of the overall process demanded a minimum of half a day for completion. This duration excludes the preparation of the SNOM probe, which entails tasks such as soldering the tuning forks onto the electrical contacts and gluing the probe onto the tuning fork. However, throughout these mentioned processes, the vulnerability of the probe tip to potential damage necessitated restarting the entire procedure, resulting in numerous setbacks that prolonged the measurement process and increased its time demands significantly.

To address these persistent challenges and enhance the success rate of fabricating a-SNOM probes, a specialized station, illustrated in Figure 3.5b was constructed exclusively dedicated to attaching the probe to the tuning fork. This station ingeniously utilized an unused component from ThorLabs, providing all three degrees of freedom required for optimal tuning fork and probe alignment. This innovative improvement greatly facilitated a higher number of successful attempts at fabricating a-SNOM probes, streamlining the overall fabrication process, and saving valuable time.

3.1.2   Laser characterization

This section focuses on characterizing the diode (PIL 040-FS and PIL 051-FS) and Ti:Sa laser (Chameleon Ultra II), as well as evaluating the suitability of the Nufern 460HP fiber [94] from ThorLabs for high-power laser transmission.

Firstly, the average power of the Ti:Sa laser was measured using its built-in power

meter. To ensure the accuracy of the measurement, a thermal power sensor [95] (S425C) from Thorlabs was used as a reliable reference, as shown in Figure 3.6a.

The characterization of the Ti:Sa laser involved measuring its average power at different wavelengths and comparing it to the manufacturer's specifications. Figure 3.6b presents the comparison, showing satisfactory agreement. However, certain factors such as imperfect calibration and slight resonator shift may contribute to discrepancies, which was identified by analyzing the positions of the mirrors within the resonator using the laser software.

The influence of the baseplate temperature was also considered, as it deviated slightly from the recommended temperature [84]. Although the temperature was maintained at approximately 29 °C, it deviated slightly from the manufacturer's recommended optimal temperature of 25 °C. This discrepancy resulted from insufficient cooling of the room, where the temperature sometimes reached 26 °C when the entire setup, including the laser, was in operation. Ideally, additional cooling measures such as an air conditioning unit should be implemented to maintain the room temperature at the desired 24 °C, ensuring compliance with the manufacturer's specified operating temperature.
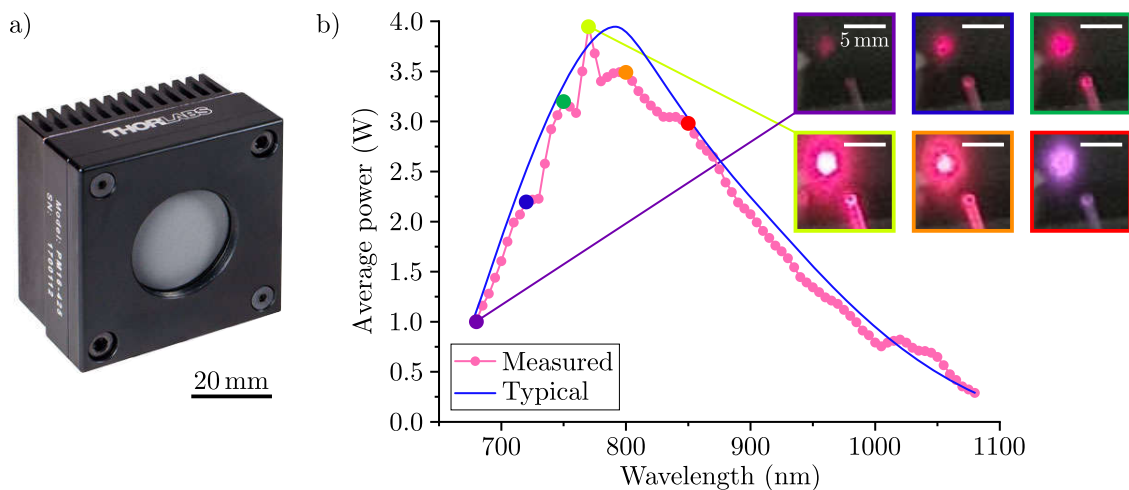

Fig. 3.6: a) Thermal power sensor head for measuring the average power of the Ti:Sa laser, taken from [95]. b) Comparison between the measured average power and the average power data provided by the manufacturer [84]. Graph insets showing snapshots of specific wavelengths illustrating laser transmission through the optical fiber.

The suitability of the Nufern 460HP fiber for high-power laser transmission was evaluated. The laser was coupled into the fiber, and video recordings were made to capture the laser's wavelength transmission through the optical fiber. Figure 3.6b includes insets showing snapshots of specific wavelengths extracted from the recordings, which demonstrate the capability of the optical fiber for efficient PL excitation within the range of $700 - 800$ nm.

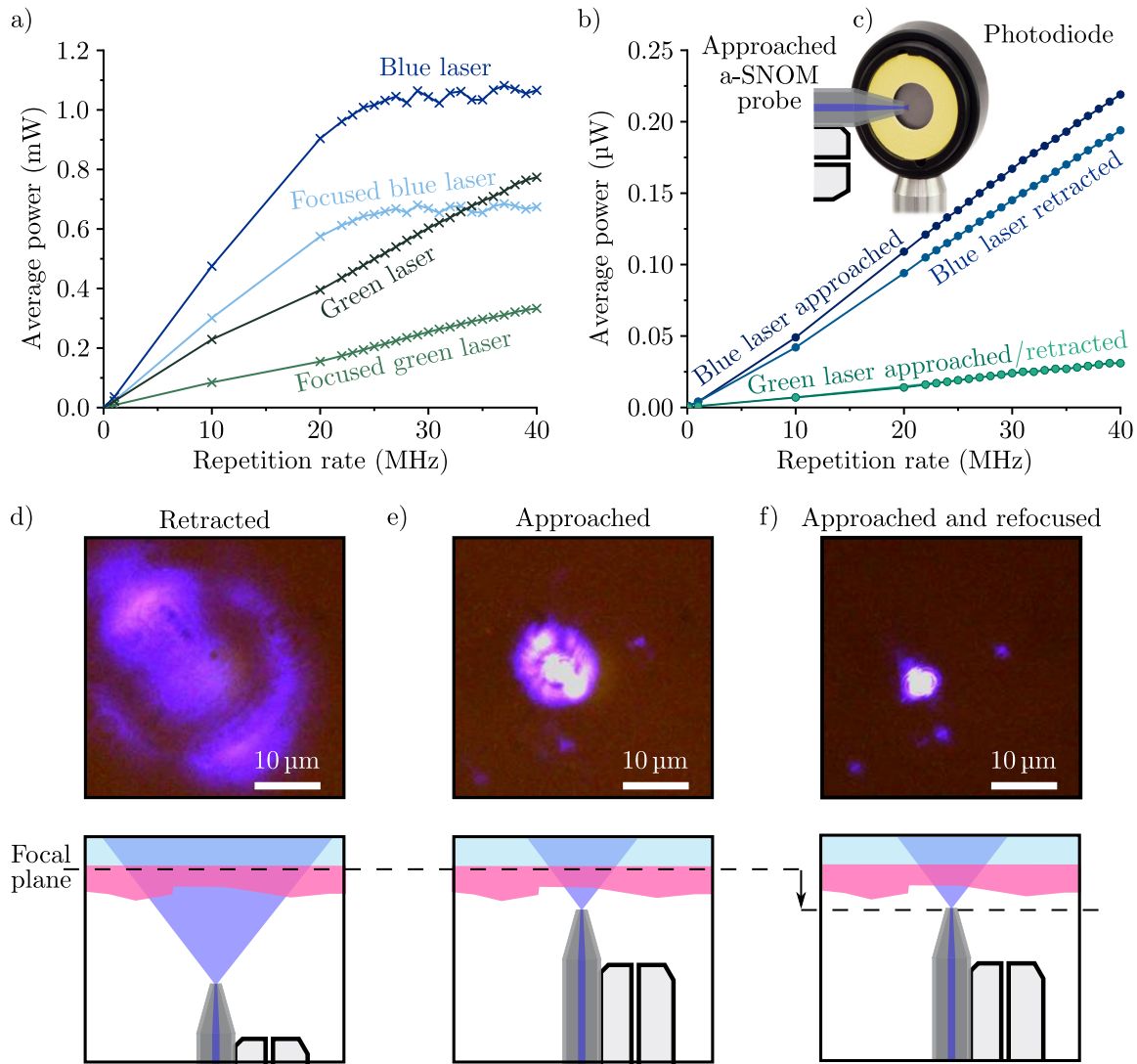Furthermore, the blue and green picosecond diode lasers were characterized. While

Fig. 3.7: Comparison of average power measurements for blue and green picosecond diode lasers at various repetition rates, measured at different positions. a) Dark and light blue represent the average power of the blue laser measured directly from the laser output and after alignment and focusing, respectively. The same process was applied to the green laser. b) Dark and light blue represent the average power of the blue laser measured in the far-field (approximately 50 µm above the sample) at the end of the metal-coated fiber tip after the laser was coupled into the optical fiber, and in the near-field (approximately a few nm above the sample), respectively. The same process was applied to the green laser. c) Standard photodiode power sensor (S120VC) from ThorLabs used for measuring the average power of the lasers [96]. Optical images of blue laser spots acquired from optical microscope for the fiber being: d) retracted, e) approached to the sample, and f) approached to the sample, showing different position of the focal plane. Illustration below the optical images show the different position of the fiber (relative to the sample) and focal plane, respectively to the image above.

these lasers are not wavelength-tunable, their repetition rate can be adjusted[2] (ranging from 1 kHz to 40 MHz). The average power was measured at various positions along the laser path using a standard photodiode power sensor (S120VC) from ThorLabs [96], as shown in Figure 3.7c.

Measurements were taken at the laser output (dark blue and green color in Figure 3.7a), after aligning mirrors and focusing the beam (light blue and green color in Figure 3.7a), at the far-field from the metal-coated fiber tip (light blue and green color in Figure 3.7b), and in the near-field by approaching the a-SNOM probe to the photodiode (dark blue and green color in Figure 3.7b). For better understanding, Figures 3.7d-f show optical images of the laser spot obtained from the microscope (with $\times 50$ zoom) with additional illustrations of the position of the probe relative to the focal plane.

In general, average power is directly proportional to the repetition rate (equation 2.1), which is in good agreement with the green laser. However, the blue laser in Figure 3.7a shows different character for the repetition rates above the 24 MHz range, likely due to the photodiode's maximum average power density limit ($20 \, \mathrm{W/cm^2}$). It is likely that the photodiode reached its maximum power limit at a repetition rate of approximately 24 MHz, and as a result, it was unable to measure higher powers. This observation is supported by the lower average power values obtained for the focused blue laser. The reduced average power is attributed to the smaller laser spot size, which maintains a similar average power density despite the lower overall average power.

Measurements of the blue laser in the near-field of the photodiode showed higher average power compared to the retracted probe, indicating a potential difference in power delivery. However, it is important to note that definitive conclusions could not be drawn due to the discrepancy in laser spot size.

Upon further investigation and discussions with the manufacturer (ThorLabs), it was revealed that the diameter of the laser spot size should ideally be larger than 1 mm for accurate measurements. In Figure 3.7e, it is evident that the diameter of the laser spot size when approached is approximately 10 µm, which falls significantly short of the recommended size. As a result, the data obtained from this particular measurement lacks sufficient validity and cannot be used to draw conclusive findings.

TRPL measurements were attempted using the picosecond diode lasers, but not with the femtosecond Ti:Sa laser due to technical limitations. The main issue encountered when trying to perform TRPL measurements with the Ti:Sa laser was its inability to communicate with the TimeTagger device, which requires a minimum pulse width of 1000 ps and a minimum pulse height of 100 mV for triggering and counting. The Ti:Sa laser incorporates a built-in PIN photodiode that sends a digital signal to the TimeTagger, exhibiting a sinusoidal waveform with varying amplitudes at different wavelengths.

To evaluate the pulse characteristics of the Ti:Sa laser, an oscilloscope was used to measure the voltage from the PIN[3] photodiode, generated by the incident laser pulse.

---

[2]In contrast, the Ti:Sa laser is solely wavelength-tunable and lacks frequency tunability.

[3]A diode with a wide, undoped intrinsic semiconductor region between a p-type and an n-type.

Figure 3.8a-b illustrates the difference between the pulses generated by the green diode laser (Figure 3.8a) operating at 40 MHz and the femtosecond Ti:Sa laser (Figure 3.8b) at specific wavelengths, namely 720 nm and 960 nm. These wavelengths were chosen for their relevance to the subsequent experimental measurements, specifically for exciting the PL of a specific sample and converting the wavelength through a nonlinear process to 480 nm, respectively.

From Figure 3.8b, it is evident that the built-in PIN photodiode of the Ti:Sa laser did not produce a sufficiently high pulse height. The pulse height for the 960 nm wavelength was approximately 60 mV, while for the 720 nm wavelength, it reached only 15 mV, falling below the 100 mV threshold required to trigger the TimeTagger. Consequently, the Ti:Sa laser was deemed suitable only for high-power excitation of the sample's PL and could not be utilized for TRPL measurements.
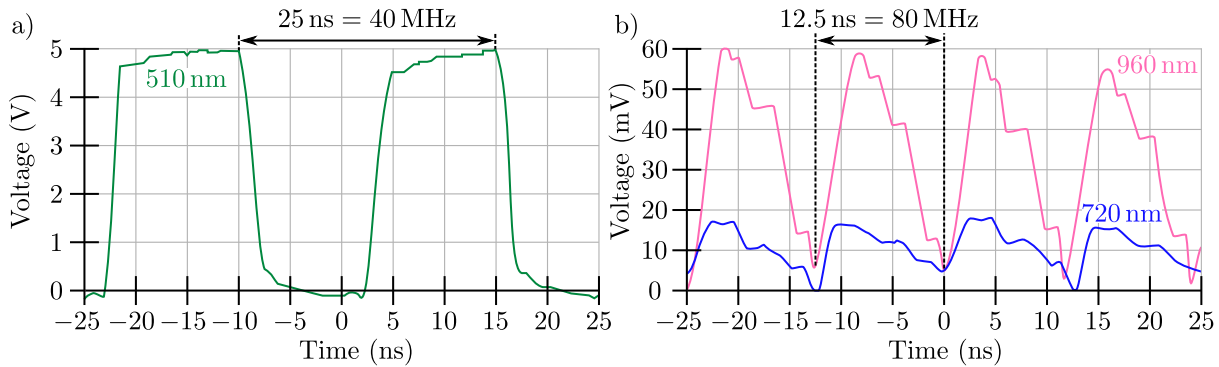

Fig. 3.8: The digital signals obtained from the a) pulsed picosecond green diode laser and the b) Ti:Sa femtosecond laser operating at wavelengths of 720 nm (pink) and 960 nm (blue). Captured and measured using an oscilloscope.

To address this issue, collaborative efforts with Ing. Zdeněk Nováček, Ph.D., focused on constructing a comparator to amplify the signal from the PIN photodiode. While successful in amplification, the high frequency of the 80 MHz range proved detrimental, leading to significant distortion of the pulse shape. In certain cases, the amplified pulse even obscured two original pulses.

The root cause of this problem can be attributed to the critical position of the mirror within the laser resonator, which hindered the reflection of pulse power onto the PIN photodiode. Consequently, the PIN photodiode generated a low-voltage digital signal, resulting in an insufficient pulse height to trigger the TimeTagger.

3.1.3 Second harmonic generation using PPLN nonlinear crystal

As discussed in the previous section 1.2.4 on nonlinear processes, second harmonic generation (SHG) is a significant second-order nonlinear process where two photons with the same wavelength interact to produce a photon with twice the frequency. In this section, the experimental result of utilizing a PPLN nonlinear crystal to generate femtosecond

pulses through second harmonic generation (SHG) at a wavelength of 480 nm. This approach offers the advantage of higher energy excitation laser, which broadens the variety of samples that can be studied, especially those with higher badngap energy. The PPLN crystal (MSHG960-0.5-1) from Covesion [97] was commercially obtained for this purpose, along with an additional oven for secure mounting and thermal stability within the range of 30 °C to 200 °C.

Figure 3.9a-c shows an image of the PPLN crystal, the oven used for secure mounting, and the SHG tuning curve provided by the manufacturer [97], respectively. The tuning curve consists of three curves representing different poling periods in the crystal, which refer to the distance between adjacent domains with opposite polarizations. Each curve corresponds to a specific poling period, resulting in different phase-matching conditions. The point of each curve indicates the combination of temperature and pump wavelength that achieves the highest conversion efficiency for a particular poling period.
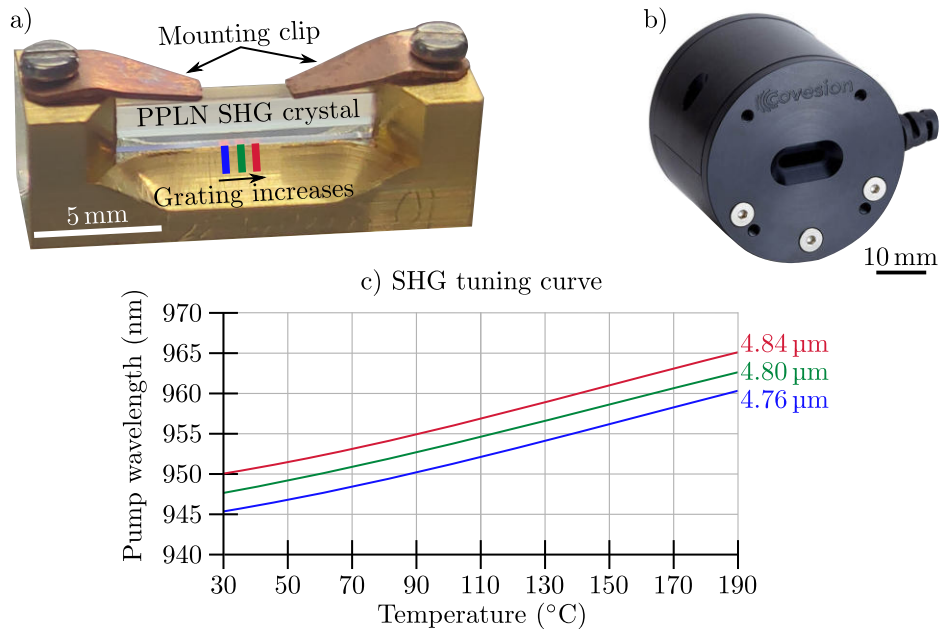

Fig. 3.9: a) Image of a MgO-doped PPLN crystal [97] used for SHG with a 960 nm pump wavelength, placed in the clip kit. b) Covesion oven designed to accommodate the PPLN crystal for enhanced stability and secure mounting, ensuring robust thermal conditions for optimal performance. c) SHG tuning curve provided by the manufacturer, showcasing the phase-matching characteristics of the nonlinear crystal. The curve highlights the temperature and pump wavelength settings that optimize the efficiency of second harmonic generation (SHG) for the specific poling periods of the crystal. Three distinct curves correspond to different poling periods, indicated by lines of the same color (the corresponding positions of varying grating periods are also highlighted in a))

Multiple curves are provided to showcase the crystal's versatility in phase-matching across various poling periods. By analyzing the curves, optimal temperature and pump

wavelength combinations can be easily identified for efficient SHG for each poling period. equation 1.12 describes the factors to consider for achieving efficient SHG, including incident power of the laser, interaction length, and effective area of the interaction.

The damage threshold for the PPLN crystal in the femtosecond regime, as provided by the manufacturer, is approximately $4\,\mathrm{GW/cm^2}$. This threshold applies when the crystal is pumped with a $140\,\mathrm{fs}$ laser having a repetition rate of $80\,\mathrm{MHz}$ and an average power of $P_{\mathrm{avg}} \approx 4\,\mathrm{W}$. Therefore, it is crucial to ensure that the power of the incident laser beam does not exceed this threshold to avoid damaging the crystal.

Nevertheless, accurately characterizing the pulse width and determining the power/area contained in the pulse prior to its focusing through the lens poses significant challenges. Typically, pulse width characterization relies on an autocorrelator, which offers valuable insights into the duration of the pulse. Unfortunately, neither the research groups at Brno University of Technology (BUT) nor CEITEC had access to an autocorrelator capable of providing precise measurements of pulse width. Despite extensive research and investigation, no relevant findings regarding the pulse width were discovered. The absence of this critical information complicates the optimization of laser focusing for efficient second harmonic generation conversion.

Considering these limitations, an alternative approach was attempted, where the PPLN crystal was illuminated directly with the femtosecond laser to avoid potential damage caused by focusing the laser beam. However, this method resulted in inefficient SHG conversion due to the lower intensity of the incident laser beam.

The experimental setup involved illuminating the PPLN crystal directly with the femtosecond laser at a pump wavelength of $960\,\mathrm{nm}$, as depicted in Figure 3.10a. The undepleted pump laser was then filtered to isolate the desired SHG wavelength. The resulting SHG generation was observed as a blue laser spot, as shown in Figure 3.10b.
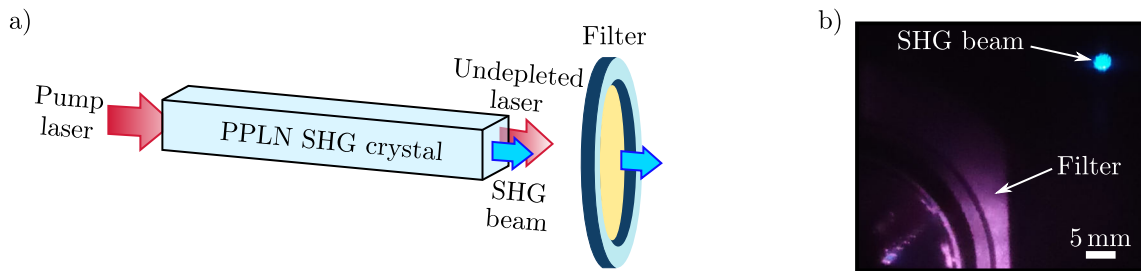

Fig. 3.10: a) Schematic representation of the experimental setup for SHG using a MgO-doped PPLN crystal and a Ti:Sa femtosecond laser with a pump wavelength of 960 nm. b) Photograph capturing the laser spot generated by the SHG process, with the incident laser beam originating from the bottom left corner.

In summary, the experimental setup utilized a PPLN nonlinear crystal illuminated directly with a femtosecond laser. Despite the limitations in precisely characterizing the pulse width and optimizing the laser focusing, the generated SHG femtosecond pulses at a wavelength of $480\,\mathrm{nm}$ were observed. However, the efficiency of the SHG process was

lower than expected due to the inability to precisely determine the pulse characteristics and the lower intensity of the incident laser beam.

The findings from this study highlight the importance of considering various factors, such as pulse characteristics, crystal damage threshold, and interaction length, when designing and implementing efficient SHG processes. These factors play a crucial role in optimizing the efficiency of SHG. Notably, the utilization of a multisegment oven, as proposed by Shahidani *et al.* [98], shows promise in further enhancing the SHG efficiency. By employing the multisegment oven scheme to control the temperature distribution within the crystal, it becomes possible to optimize the pulse characteristics for SHG.

To advance the efficiency of SHG using PPLN nonlinear crystals, further investigations and improvements in pulse characterization are necessary. The availability of an autocorrelator for precise pulse width measurements would be particularly valuable in this regard. By addressing the challenges associated with pulse characterization and laser focusing optimization, significant improvements in the efficiency of SHG processes can be achieved. This, in turn, opens up new possibilities for enhanced applications in various fields.

Moreover, the results of this study confirm that utilizing SHG provides an avenue for exciting PL in materials with a bandgap of approximately 2.6 eV (above 480 nm). This expansion of the wavelength range allows for the study of a broader range of materials, thereby tremendously enriching the portfolio of research opportunities.

In conclusion, addressing pulse characterization issues, optimizing laser focusing, and exploring innovative techniques are essential for further advancements in the field [99, 100]. These key areas of focus offer promising prospects for improving the efficiency of SHG processes using PPLN nonlinear crystals. Overcoming challenges in pulse characterization, optimizing laser focusing, and implementing innovative techniques such as the multisegment oven [98] can lead to significant advancements in SHG efficiency. These advancements not only expand the range of applications but also open up exciting possibilities for materials research.

3.2   Data analysis and interpretation

In this diploma thesis, a Python software program was created to analyze spectral data obtained from a spectrograph and generate topography and intensity maps (using Litescope). Developed in collaboration with Ing. Ondrej Černek, the program incorporates a user-friendly graphical user interface (GUI) that streamlines the process of loading, editing, and saving data in the ASCII file format[4]. The saved ASCII files can be further processed using software such as Gwyddion [101] (for topography and PL maps) or OriginPro [102] (for data analysis and fitting of TRPL data).

---

[4]ASCII files are text files that contain measurement data arranged in a specific tabular format, allowing easy access, manipulation, and analysis of the data using various software tools.

Before delving into the program's functionalities, it is essential to understand the data structure and storage. During experimental measurements, the scanning area (which is scanned point-by-point, as shown in Figure 2.6b, up to $100 \times 100\,\mu m^2$) and parameters such as exposure time and the number of accumulations for the CCD camera are specified. All measured data are then saved in a designated folder, with each text file representing a specific scanned pixel. These text files contain 1024 numbers, corresponding to the spectral resolution of the CCD camera ranging from 395 nm to 950 nm. The file names consist of three numbers: the first two indicate the x and y positions of the excited area, while the third number represents the z position (topography) of the a-SNOM probe relative to the sample. Additionally, a reference text file containing spectrum obtained with the spectrograph shutter closed is included in the folder. This reference file can be loaded into the program and subtracted from the other data.

Figure 3.11 illustrates the GUI program. In the top left corner, users can specify the path to the folder containing the stored data. As an example, a scan of MaPbI$_3$ on fused silica substrate is shown (more detailed analysis will be in section 3.3.1), with scanning parameters of $20 \times 20\,\mu m$ and a resolution of 155 nm per pixel (total of 128×128 pixels). The integration time (for each pixel) was set to 0.1 s, and two accumulations were performed. It is worth noting that this particular scan took approximately 6 hours to generate both the topography map (displayed in the top left corner of Figure 3.11) and the intensity map (shown in the bottom left corner). The extensive time required for data acquisition further emphasizes the necessity for automation and the development of additional software tools to streamline the evaluation process, reducing the reliance on manual user intervention.

The topography map is constructed using the first two numbers in the text file names as the x and y positions, respectively, while assigning the third number as the z position (topography) corresponding to the scanned sample. On the other hand, the intensity map is generated by summing all 1024 rows in each file, resulting in a single value assigned to each pixel (with x and y positions determined in the same manner as the topography map). Furthermore, users have the ability to select a specific wavelength for intensity calculation. The graph displayed in the top right corner of Figure 3.11 presents the spectrum obtained from the white dot in the intensity map, which is also represented by a white dot in the topography map. The red vertical lines highlight the selected wavelength range (from 680 nm to 880 nm), showcasing the PL of the given sample. By adjusting the vertical or horizontal line positions, users can navigate through the maps and analyse the spectrum for each pixel.

The program also includes additional features, such as the noise-reduction coefficient (NRcoeff). This feature was primarily implemented to eliminate muon peaks, which hindered the scaling of intesity maps due to their significantly higher intensity for certain pixels. The NRcoeff function scans through each wavelength and compares the intensity count for the given wavelength with a certain threshold. In the provided Figure 3.11, NRcoeff is set to 1.1, meaning that if the intensity count exceeds 1.1 times the previous
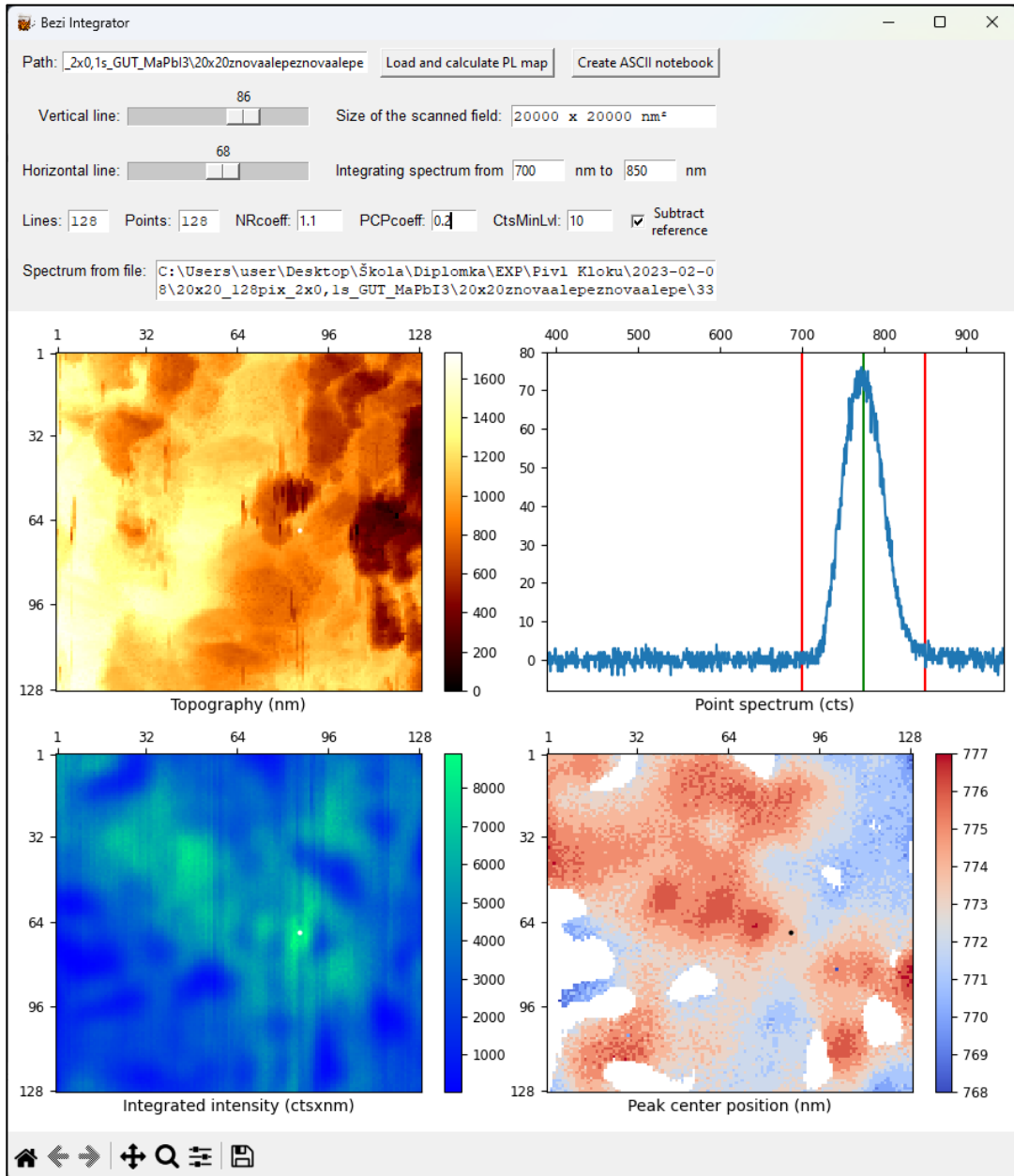
Fig. 3.11: GUI of the program developed in collaboration with Ing. Ondrej Černek for loading, editing, and analyzing topography and intensity maps, as well as individual spectra for each pixel. The program includes a map (bottom right corner) displaying the mass-center wavelength (λ_c) calculated from each pixel, enabling further analysis of the peak position.

intensity count, it is averaged with the two previous numbers (intensity counts).

In addition, the program evaluates the mass-center wavelength of the PL peak, depicted in Figure 3.11 as a green vertical line in the spectrum graph and as a map in the bottom right corner. This particular value is referred to as λ_c, which is illustrated in Figure 2.7a and represents the peak center position (PCPcoeff). Within Figure 3.11, PCPcoeff is designated as 0.20. The software compares the integrated intensity of each

pixel with the highest integrated intensity among all pixels. Pixels yielding a division result below 20 % are displayed as white pixels on the map. For pixels surpassing this threshold, the program employs additional information about the PL peak to calculate λ_c.

Lastly, the program utilizes the counts minimal level (CtsMinLvl) to integrate the intensity of the spectrum above a set threshold. In Figure 3.11, the threshold is set to 10 counts.

It is important to note that all presented results in the following section were interpreted and analyzed using the aforementioned program. Subsequently, the results were exported as ASCII files for further analysis in Gwyddion.

3.3   Samples

This section presents the results of NF excited PL mapping for two distinct perovskite samples: methylammonium lead iodide (MAPbI$_3$) and cesium lead bromide (CsPbBr$_3$). These samples, prepared by Ing. Matouš Kratochvíl, Ph.D., at the Faculty of Chemistry, BUT, were spin-coated onto thin (1 mm) fused silica substrates and subsequently annealed. They were chosen for their promising applications in optoelectronic devices [103], as perovskite materials offer a high degree of compositional engineering, allowing for the tunability of their direct bandgap through various composition engineering methods. This versatility makes perovskites highly promising candidates for the photoactive component in solar cells [104].

Perovskite materials, including lead halide perovskites (LHPs), exhibit a unique cubic APbX$_3$-type lattice structure. In this structure, the A component represents monovalent cations, such as cesium (Cs$^+$), methylammonium (MA$^+$), or formamidinium (FA$^+$), while the divalent cation lead (Pb^{2+}) can be substituted with tin (Sn^{2+}) or germanium (Ge^{2+}). The X component corresponds to halide anions, including iodide (I$^-$), bromide (Br$^-$), or chloride (Cl$^-$). These perovskite structures consist of interconnected [PbX$_6$]$^{4-}$ octa-
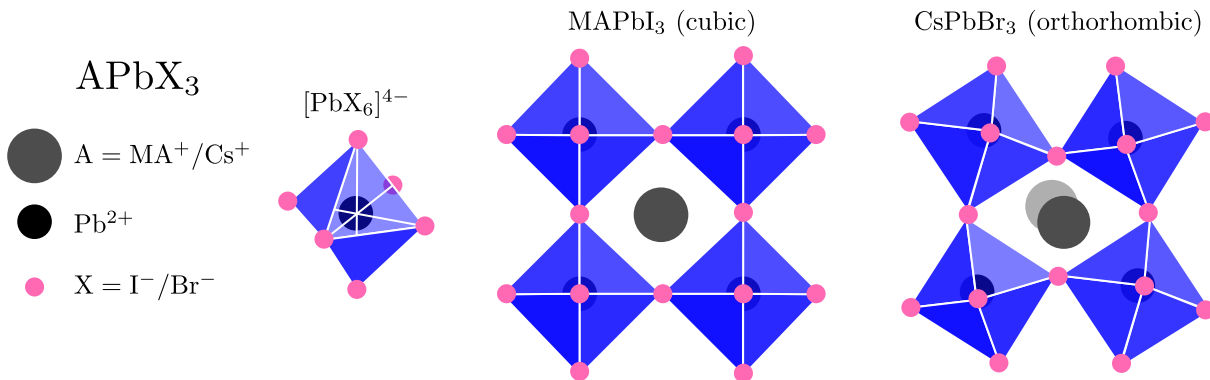

Fig. 3.12: The APbX$_3$ perovskite structure with 3D-corner-sharing octahedra [PbX$_6$]$^{4-}$. Two typical crystal structures of lead halide perovskites: cubic (MAPbI$_3$) in the middle and orthorhombic (CsPbBr$_3$) on the right. Adapted from [105].

hedra with A-site cations occupying the vacant spaces. Notably, MAPbI$_3$ and CsPbBr$_3$ exhibit cubic or orthorhombic symmetries and have cuboidal shapes in the form of LHP nanocrystals [105].

The objective of this study is to gain insights into the optical properties of these perovskite samples and understand the correlation between PL and sample topography. By performing NF excited PL mapping, we can investigate the spatial distribution of PL emission, visualize PL and topography maps, and analyze spectra from selected pixels. The obtained results can contribute to the advancement of perovskite-based devices and assist in optimizing their performance.

3.3.1 MAPbI$_3$

NF excited PL mapping was successfully performed on MAPbI$_3$ samples using a shear-force scanner (Litescope) with the a-SNOM probe coupled with a 685 nm laser, providing $P_{avg} \approx 1.2\,W$ of laser excitation power before fiber coupling. The NF spot was scanned across the sample to locally excite and collect PL from MAPbI$_3$. Using a-SNOM setup (shown in Figure 3.3) with PL collection in transmission geometry, allows for simultaneous measurements of topography and PL maps at each pixel. At each pixel, topography and a full emission spectrum (background corrected) ranging from 400 nm to 900 nm were recorded. The PL maps were generated by integrating the intensity spectrum, capturing both amplitude and spectral variations.

Figure 3.13 presents two different scans performed on two MAPbI$_3$ samples. The topography map of sample I reveals a homogeneous film, while sample II exhibits micron-sized needle-like structures with a rougher surface and a higher area of voids, consistent with previous studies by Williams *et al.* [106].

Spatially integrated emission spectra across the entire film exhibit PL peak at 770 nm, in good agreement with published spatially averaged film measurements [107], as well as with NF excited PL maps obtained by a-SNOM [108]. Notably, sample II exhibit "hot spots" with up to 15 times higher PL intensity compared to sample I "hot spots". This discrepancy can be attributed to various factors, including laser coupling, sample fabrication, and, significantly, the use of different probes for scanning. The smaller aperture diameter of the a-SNOM probe reduces the coupled laser transition [70], resulting in lower excitation power and consequently lower PL emission.

In addition, the study also identified the limited attempts in imaging and correlating perovskites using NF microscopy [109]. Green dashed lines are included in the maps as visual guides, highlighting the correlation between the topography and intensity map. These lines were created by selecting specific spots in the intensity map and then copying and shifting them onto the topography map. The observed shift between the intensity and topography maps can be attributed to the misalignment of the a-SNOM probe tip's end from the aperture, causing the excitation spot to deviate from the topography region. The imperfect correlation between the intensity maps and topography is influenced by
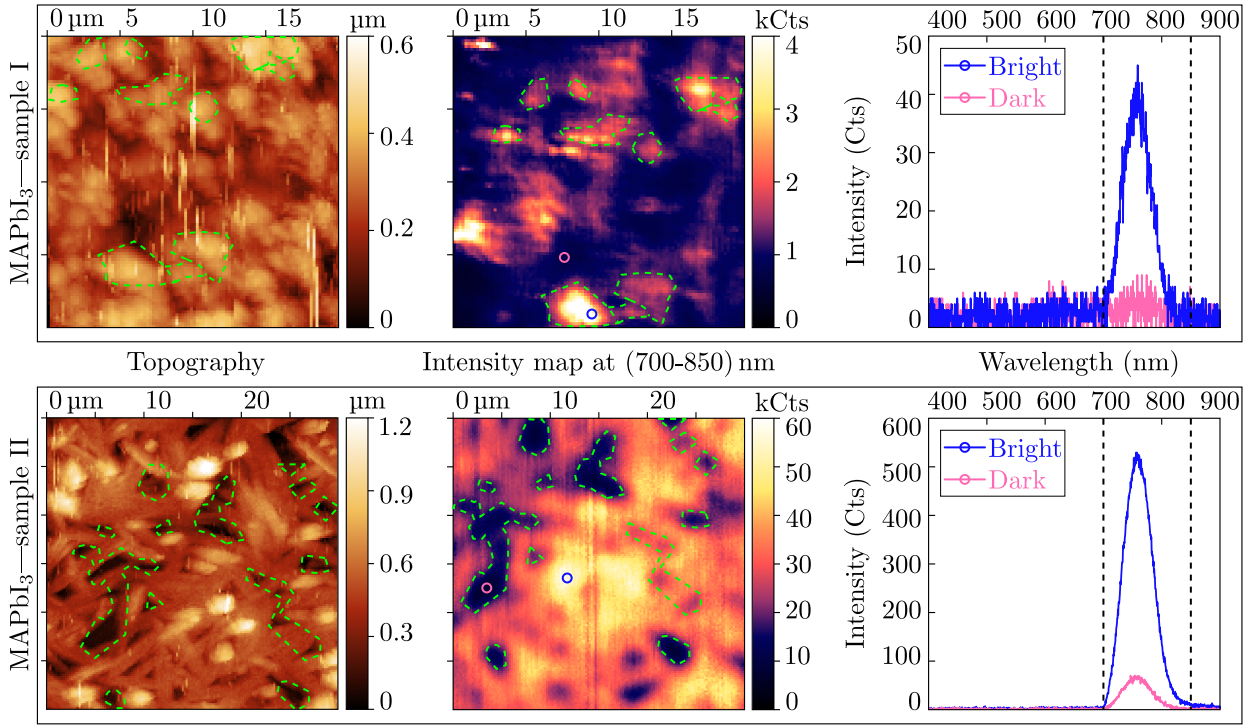
Fig. 3.13: Measured NF excited PL mapping of MAPbI$_3$. The upper row presents the maps obtained for sample I, including the topography map (left), intensity map (middle), and PL spectrum (right) extracted (and background corrected) from the highlighted pixels in the intensity map. The intensity map shows the PL intensity ranging from 700 nm to 850 nm, indicated by the vertical dashed lines in the graphs. The bright (blue circle) and dark (pink circle) spot pixels are plotted in the graph. The bottom row shows the same maps obtained for sample II. Both spectra exhibit PL peaks at 770 nm, excited by an a-SNOM probe coupled with a Ti:Sa laser ($\lambda = 685$ nm, $P_{avg} \approx 1.2$ W). The accumulation time was 4 s for sample I and 0.2 s for sample II. Observed localized spatial variations in PL intensity up to 60 kCts (kilocounts) show a correlation with features in topography, highlighted by green dashed lines. Both samples have resolution of 200 nm per pixel for each map.

the setup's geometry. The uneven and non-uniform topography of the films suggests that excitation can sometimes occur in the bulk of the sample, leading to a mismatch with the topography. Additionally, spatial modulation in the PL maps can be influenced by light scattering and reflection. To verify this, measurements taken in transmission and reflection at the same location could be compared to observe the PL patterns. Both samples have a resolution of 200 nm per pixel in each map. In the intensity map of sample I, the bright grains are limited by the pixel resolution, indicating the use of a sharper probe tip (resulting in higher resolution) but lower transmission efficiency (due to the smaller aperture size) for exciting PL from the sample.

Additionally, a higher-resolution scan (Figure 3.14) was performed using a 10×10 µm^2 scan size and 200×200 pixels, resulting in a 50 nm resolution per pixel. The correlation

between topography and intensity map was challenging to determine. To provide additional information, a mass-center (λ_c) map was calculated from the intensity map. Each spectrum had an integration time of 0.1 s. Five different PL peaks were chosen from λ_c map and determined from the intensity map, represented by green circles in both maps, indicating a shift in the λ_c peak position. Interestingly, the observed shift in λ_c wavelength is directly correlated with the intensity of the PL peak, suggesting that a higher intensity corresponds to a lower λ_c wavelength. Grain stress or size variations within the material can contribute to this phenomenon. Muscarella *et al.* [110] found that the crystallographic orientation of MAPbI$_3$ grains has no significant influence on the optical and local electronic properties, indicating other factors, such as grain stress or size variations, may be responsible for the observed correlation between the PL intensity and the λ_c wavelength.

Understanding these factors and their impact on optical and local electronic properties is crucial for optimizing halide perovskite materials in optoelectronic applications. The assessment by deQuilettes *et al.* [111] highlights photon recycling as a potential contributor to increased lifetime in samples with high photoluminescence quantum yields, while further investigation into polaron dynamics is emphasized.
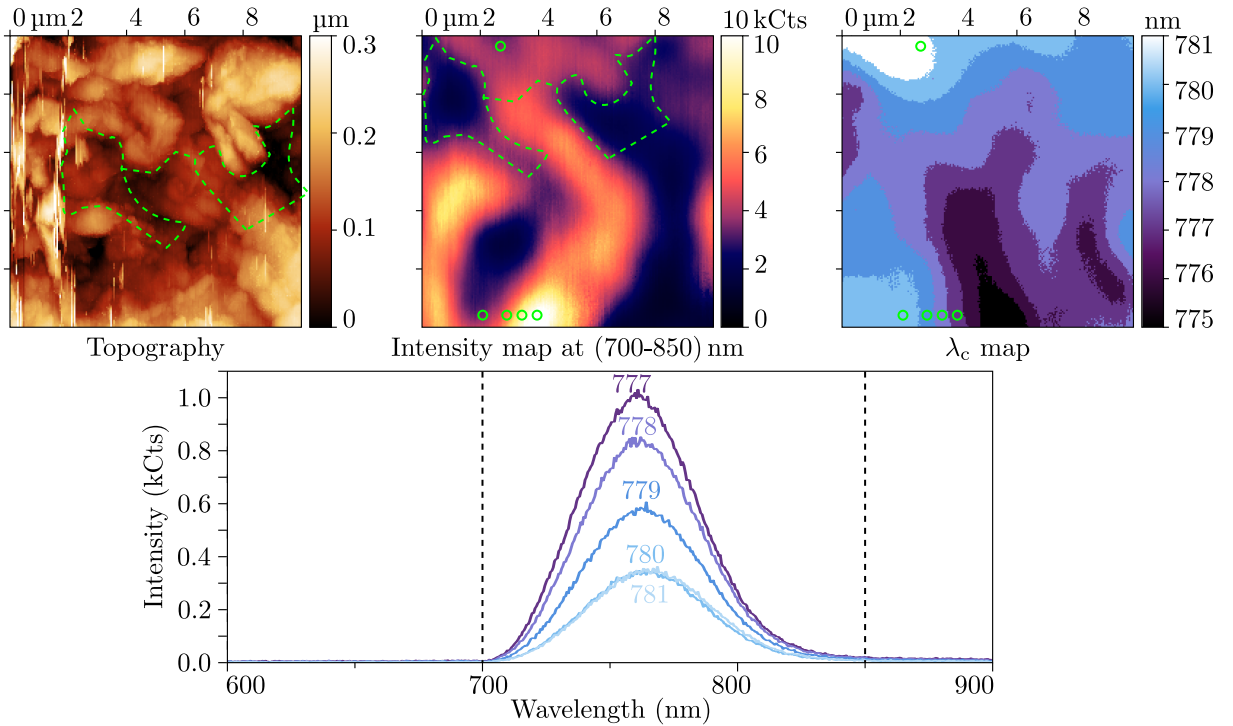

Fig. 3.14: Measured NF excited PL mapping of MAPbI$_3$, showcasing topography (left), intensity map (middle) integrated (and background corrected) from 700 nm to 850 nm, λ_c map (right), and PL spectrum (bottom) selected from five specific pixels denoted by green circles in the intensity and mass-center maps. The accumulation time was 0.1 s and the PL intensity ranged up to 100 kCts. A resolution of 50 nm per pixel was achieved.

3.3.2 CsPbBr₃

Further investigation of NF excited PL mapping was conducted on a CsPbBr$_3$ sample. The experimental setup (shown in Figure 3.3) utilized combined topography and intensity detection. However, in this case, a pulsed diode laser with a wavelength of 407 nm was employed as the excitation source, coupled into the a-SNOM probe. The obtained results, presented in Figure 3.15, reveal interesting characteristics of CsPbBr$_3$ as a fully inorganic material.

CsPbBr$_3$ generally forms nanocubes with sizes of approximately 12 nm, which tend to aggregate and form clusters or islands [112]. This unique morphology can explain the observed intensity (PL) map in Figure 3.15, where the bright spots correspond to these clustered regions. The nanocubes tendency to form aggregates provides valuable insights into the spatial distribution and arrangement of CsPbBr$_3$ within the sample.

Moreover, the fully inorganic nature of CsPbBr$_3$ suggests that it may exhibit higher stability against external factors such as humidity and temperature, compared to MAPbI$_3$. This enhanced stability further emphasizes the potential of CsPbBr$_3$ for various applications where environmental robustness is essential.

The presence of vertical black lines in the topography map during the vertical scan suggests that suboptimal feedback settings of the scanner may have caused a delayed response to sudden height changes. Although there is some correlation observed between the topography and intensity map (integrated from 480 nm to 580 nm), the remaining grain boundaries do not show strong agreement with the obtained topography. While a green dashed line in both maps indicates a potential shift, it is important to note that a definitive and conclusive correlation, similar to what was observed in Figure 3.3 for sample II, cannot be established.
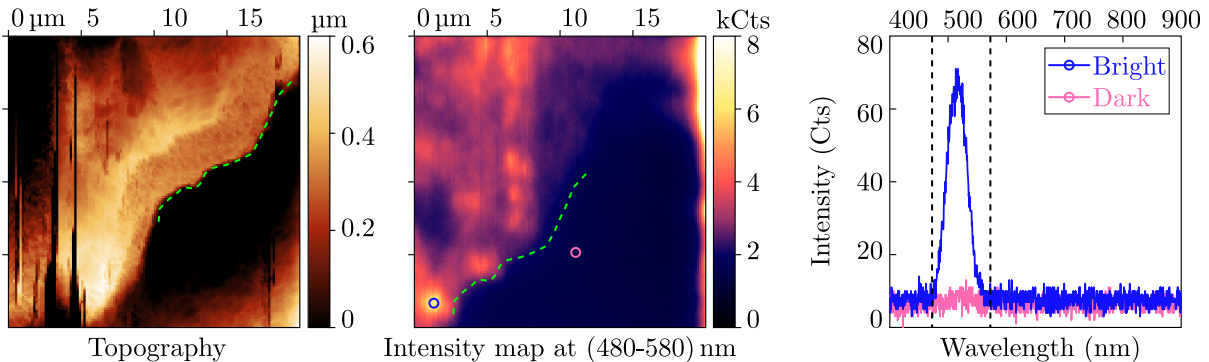

Fig. 3.15: NF excited PL mapping of CsPbBr$_3$, showcasing topography (left), intensity map (middle) integrated (and background corrected) from 480 nm to 580 nm, and PL spectrum (right) selected from bright (blue circle) and dark (pink circle) spot pixels. The spectrum of PL for bright pixel exhibits a peak at 515 nm, excited by an a-SNOM probe coupled with a pulsed diode laser ($\lambda = 407$ nm, $P_{\text{avg}} = 5$ mW). The accumulation time was 1 s and the PL intensity ranged up to 8 kCts. A resolution of 155 nm per pixel was achieved.

The PL spectrum obtained from the bright and dark spot, plotted in graph represented by blue and pink color, respectively, show again agreement with literature [89] as well as agreement with the far-field measurement presented in Figure 3.2a.

3.3.3   Near-field excited time-resolved photoluminescence

Time-resolved photoluminescence (TRPL) spectroscopy is a powerful technique used to investigate the recombination kinetics of PL materials, which is extensively studied in section 2.2.3. It provides valuable insights into the radiative and non-radiative recombination processes occurring in the system and its surroundings. TRPL involves periodically exciting the sample with pulsed lasers and measuring the emitted light at the desired wavelength using time-correlated single photon counting (TCSPC). This technique, motivated by the need to understand these processes, relies on a large number of excitation pulses, often ranging from millions to billions, to achieve a sufficient signal-to-noise ratio (SNR) [113]. The theoretical background and motivation behind utilizing TRPL are discussed in detail in section 2.2.3.

In the context of our study, we revisit the measurement of NF excited PL using an a-SNOM setup. Previously, all the PL emission was collected by a single fiber for analysis. However, to simultaneously measure both PL and TRPL, we split the collection fiber output into two channels with a 70:30 coupling ratio. The 30 % of collected PL was directed to a spectrograph for PL measurement, while the remaining 70 % was sent to an avalanche diode (coupled with a TimeTagger) for TRPL measurement.

This approach allows us to probe the sample while collecting the PL and TRPL signal for optoelectronic characterization. However, it introduces new challenges, particularly in terms of SNR for TRPL measurements. Experimental testing showed that the PL signal needed to exceed 100 counts (with a 70 % collection fiber output and 1-second accumulation) to surpass the avalanche diode threshold and enable TCSPC. Achieving this requirement involved extensive fine-tuning and adjustments to maximize the SNR. Additionally, it was challenging due to the lower excitation power of the pulsed diode lasers used for time-resolved measurements. Further details on laser characterization can be found in section 3.1.2.

By incorporating TRPL into our measurements, we gain deeper insights into the dynamics of light-matter interactions in the near-field regime. However, optimizing the experimental setup and overcoming SNR limitations are essential for obtaining reliable and accurate time-resolved data.

Figure 3.16 shows NF excited TRPL measurements of $CsPbBr_3$ sample, excited by a-SNOM coupled with blue (407 nm) pulsed diode laser. The accumulation time for the measurement was 30 minutes. To enhance the quality of the TRPL data obtained (shown in Figure 3.16a), an additional step was taken to average the data into a single exponential, as depicted in Figure 3.16b. This averaging process aimed to improve the exponential quality and subsequently enhance the fit quality. The averaged data were then analyzed

by fitting them with a single exponential function according to equation 2.2, resulting in a calculated mean exciton lifetime of $\tau = 1.85\,\text{ns}$ and corresponding amplitude of $I_0 = 93$.
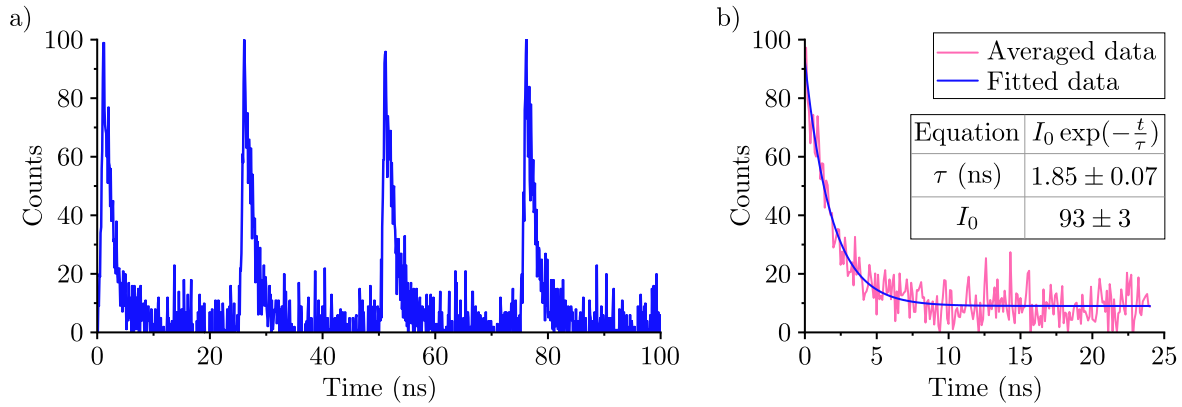

Fig. 3.16: Measured NF excited TRPL of CsPbBr$_3$ sample, under excitation by an a-SNOM probe coupled with a pulsed diode laser ($\lambda = 407\,\text{nm}$, $P_{\text{peak}} = 3\,\text{W}$). Graph a) displays the plot of the measured TRPL data, while graph b) demonstrates the averaged and fitted results from the four exponential decays.

The disparity between the two measured lifetimes in Figure 3.16b (1.85 ns) and Figure 3.2b (9.18 ns) can arise from various factors. As suggested by Jiang *et al.* [114], these factors may include variations in growth conditions, crystal quality, or presence of defects, such as dislocations, grain boundaries, or point defects. Such factors can significantly impact carrier dynamics and recombination processes, leading to differences in the observed lifetimes.

When analyzing and interpreting variations in the effective lifetime of excitons in CsPbBr$_3$, it is crucial to consider the growth technique employed, the quality of the samples, and the presence of structural defects. Further investigations and characterization techniques can provide deeper insights into the specific mechanisms behind the observed changes in carrier lifetime, thus offering a better understanding of the optoelectronic properties of CsPbBr$_3$ perovskite materials. This was the motivation behind the attempt to perform NF excited TRPL mapping, which has the potential to analyze recombination effects at the subdiffraction limit. To the best of author's knowledge and research, this has not been previously observed and published.

Figure 3.17 presents a proof-of-concept demonstration of NF excited TRPL mapping. The Figure 3.17a-c showcases topography, intensity scan (at 480-580 nm), and TRPL scan, respectively. In Figure 3.17c, the TRPL map represents the fitted mean exciton lifetime, which is dependent on the sample's x and y positions. The values obtained from the fit exhibit a similar lifetime of excitons as shown in Figure 3.16b. Notably, changes in position (pixel) induce variations in lifetime, ranging from 0.4 ns to 2.1 ns. The TRPL map provides valuable information about the spatial distribution of recombination kinetics occurring on the surface, which can be further correlated with the topography and intensity (PL) map.
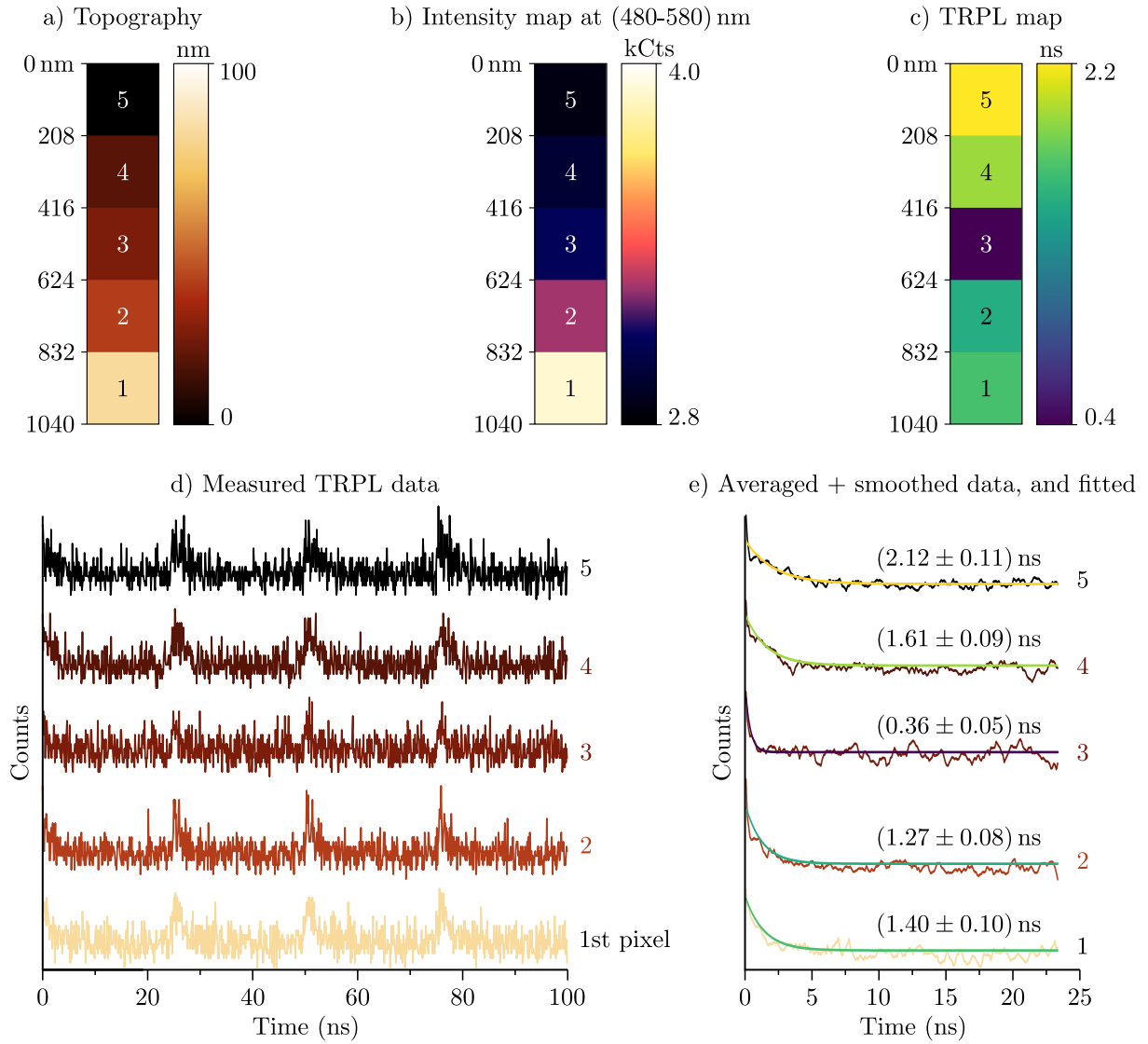
Fig. 3.17: Measured NF excited TRPL map of CsPbBr₃ sample. The accumulation time for the TRPL measurement was 3 minutes, and for PL measurement 10 s. a) Topography and b) Intensity map show strong correlation between the height and intesity of scanned sample. c) TRPL map shows for pixels 3-5 weird results which are proved with map b), showing that for those pixels, much worse PL signal was measured, achieving even lower SNR for the TRPL, resulting in higher error for the fit. d) Graph of measruerd TRPL for all 5 pixels, which were additionally processed and showed with the fit in e).

It is worth mentioning that the raw TRPL data obtained from the avalanche diode, as shown in Figure 3.17d, require additional data processing and fitting procedures to extract reliable lifetime information. Due to the low SNR, additional techniques such as averaging and smoothing (using adjacent averaging) were applied, following the literature [115], to enhance the data quality, as demonstrated in Figure 3.17e.

For more reliable data acquisition, a more powerful laser would be beneficial. Even achieving a modest 1 % conversion efficiency from a Ti:Sa laser coupled with a SHG PPLN

nonlinear crystal would provide a significant increase in average power, resulting in an improved SNR. Alternatively, extending the accumulation time could enhance the data quality, although this would prolong the measurement time considerably. Additionally, alternative approaches for PL [116] and TRPL measurements [117] below the optical diffraction limit are suggested as potential avenues for future exploration, offering further insights into spatial distribution and kinetics of recombination processes.

Conclusions

This thesis successfully achieved its goals by conducting a comprehensive research study on near-field (NF) excited photoluminescence (PL) mapping and time-resolved optical spectroscopy. The primary objectives, which were to conduct a research study, assemble and verify an experimental setup, experimentally study NF excited PL, and attempt to measure NF excited PL using time-resolved optical spectroscopy, were all successfully accomplished. Significant progress was made in understanding PL measurements, employing experimental techniques, and developing NF optical microscopy methods. The theoretical background provided a solid foundation for comprehending PL measurements, while the experimental methods section detailed the techniques employed, including optical spectroscopy, laser spectroscopy, PL imaging, and time-resolved photoluminescence (TRPL) imaging.

The results and discussion section presented the main findings, including the experimental setup, challenges encountered (during the development of the setup), laser characterization, second harmonic generation (SHG), and data analysis. Specific samples, such as $MAPbI_3$ and $CsPbBr_3$, were studied to gain insights into their PL properties, and although measuring TRPL using the NF approach posed challenges, valuable results were obtained.

To further enhance the acquisition of high-resolution maps, future developments should focus on hardware and software co-design to reduce acquisition time and achieve higher temporal, spectral, and spatial resolutions. Optimized algorithms for automated data evaluation are also recommended. The study confirmed the potential of using second harmonic generation (SHG) to excite PL in materials with a bandgap above $480\,nm$, expanding the range of study materials and presenting new research opportunities. Promising prospects lie in utilizing periodically poled lithium niobate (PPLN) nonlinear crystals to improve the efficiency of SHG processes. Areas for further advancements include addressing pulse characterization issues, optimizing laser focusing, and exploring innovative techniques for efficient SHG conversion. Exploring alternative approaches and measurement methods for further correlation, such as PL mapping in reflection geometry (e.g., WITec Raman at CEITEC), can provide valuable insights. Implementing these approaches may require additional steps, such as creating marks on the sample using focused ion beams for improved sample navigation.

This thesis introduced a proof-of-concept for NF excited TRPL mapping, demonstrating the potential of TRPL maps obtained through aperture-type scanning near-field optical microscopy (a-SNOM). The future prospects of studying exciton lifetimes beyond the diffraction limit and gaining a deeper understanding of PL dynamics hold great promise for further investigations in this emerging field.

In conclusion, this diploma thesis successfully conducted a comprehensive research study on NF excited PL mapping and time-resolved optical spectroscopy, contributing to the understanding of NF optical phenomena. The experimental setup was assembled and

verified, and NF excited PL was studied on advanced materials and nanostructures. Valuable insights were gained throughout the challenging process. The introduction of state-of-the-art TRPL mapping through a-SNOM opens up exciting possibilities for studying exciton lifetimes beyond the diffraction limit, deepening the understanding of PL dynamics in subdiffraction regimes.

Moving forward, the author plans to acquire TRPL maps with high lateral resolution, allowing for a more detailed exploration of dynamic processes in the studied materials. Additionally, the author aims to disseminate the findings by publishing the results in a high-impact journal. This valuable contribution will enhance the overall understanding of the subject and promote further advancements in the field.

Bibliography

[1] R. W. Boyd. "The nonlinear optical susceptibility". in *Nonlinear Optics*. Third Edition. Burlington: Elsevier, 2008, pp. 1–67. DOI: `10.1016/B978-0-12-369470-6.00001-0`.

[2] D. J. Griffiths. *Introduction to electrodynamics*. Fourth edition. Cambridge: Cambridge University Press, 2017.

[3] D. Halliday, R. Resnick, and J. Walker. *Fundamentals of Physics*. 11th Edition. Hoboken NJ: Wiley, 2018.

[4] B. E. A. Saleh and M. C. Teich. *Fundamentals of photonics*. 2nd ed. Hoboken: Wiley-Interscience, 2007.

[5] J. B. Khurgin. "Nonlinear optics from the viewpoint of interaction time". *Nature Photonics*. 2023. DOI: `10.1038/s41566-023-01191-3`.

[6] A. Beiser. *Concepts of Modern Physics*. 6th Edition. McGraw-Hill Science, 2002.

[7] B. V. Suresh. *Solid State Devices And Technology*. 3rd edition. India: Pearson Education, 2010.

[8] C. Kittel and P. McEuen. *Introduction to solid state physics*. 8th ed. Hoboken: Wiley, 2005.

[9] V. M. Pereira. "Topological excitons". *Nature Physics*. vol. 18. no. 1, pp. 6–7. 2022. DOI: `10.1038/s41567-021-01466-y`.

[10] "Periodically Poled Lithium Niobate (PPLN) - Tutorial". (2014). [Online]. Available: `https://www.thorlabs.com/catalogpages/693.pdf`.

[11] N. C. Panoiu, W. E. I. Sha, D. Y. Lei, and G.-C. Li. "Nonlinear optics in plasmonic nanostructures". *Journal of Optics*. vol. 20. no. 8, p. 083 001. 2018. DOI: `10.1088/2040-8986/aac8ed`.

[12] R. Eckardt and J. Reintjes. "Phase matching limitations of high efficiency second harmonic generation". *IEEE Journal of Quantum Electronics*. vol. 20. no. 10, pp. 1178–1187. 1984. DOI: `10.1109/JQE.1984.1072294`.

[13] X. Li et al. "Efficient second harmonic generation by harnessing bound states in the continuum in semi-nonlinear etchless lithium niobate waveguides". *Light: Science & Applications*. vol. 11. no. 1, pp. 1–8. 2022. DOI: `10.1038/s41377-022-01017-x`.

[14] D. Nikogosyan. *Nonlinear Optical Crystals: A Complete Survey*. 1st ed. Springer New York, 2006.

[15] I. Pelant and J. Valenta. *Luminiscenční spektroskopie. I., Objemové krystalické polovodiče*. Vyd. 1. Praha: Academia, 2006.

[16] Y. Kajino et al. "Anti-Stokes photoluminescence from $CsPbBr_3$ nanostructures embedded in a Cs_4PbBr_6 crystal". *Phys. Rev. Mater.*. vol. 6, p. L043001. 4 2022. DOI: `10.1103/PhysRevMaterials.6.L043001`.

[17] D. A. Skoog, F. J. Holler, and T. A. Nieman. *Principles of Instrumental Analysis*. 5th Edition. Belmont California: Brooks/Cole, 1998.

[18] J. R. Lakowicz. *Principles of fluorescence spectroscopy*. 3rd ed. New York: Springer, 2006.

[19] H. H. Telle and Á. G. Urena. *Laser spectroscopy and laser imaging. An introduction*. 1st Edition. Boca Raton: CRC Press, 2018.

[20] "How to interpret a Jablonski diagram". (2023). [Online]. Available: `https://www.edinst.com/us/blog/jablonski-diagram-2/`.

[21] R. Wyatt. "Comment on "on the dispersion of a prism used as a beam expander in a nitrogen-laser pumped dye laser"". *Optics Communications*. vol. 26. no. 1, pp. 9–11. 1978. DOI: `10.1016/0030-4018(78)90330-9`.

[22] "What is a spectrometer?" (2023). [Online]. Available: %5Curl%7Bhttps://www.edinst.com/us/blog/what-is-a-spectrometer/%7D.

[23] P. Makuła, M. Pacia, and W. Macyk. "How to correctly determine the band gap energy of modified semiconductor photocatalysts based on uv–vis spectra". *The Journal of Physical Chemistry Letters.* vol. 9. no. 23, pp. 6814–6817. 2018. DOI: `10.1021/acs.jpclett.8b02892`.

[24] H.-H. Perkampus. *UV-VIS Spectroscopy and Its Applications.* 1st ed. Berlin: Springer, 1992. DOI: `10.1007/978-3-642-77477-5`.

[25] Y. Chabal. "Surface infrared spectroscopy". *Surface Science Reports.* vol. 8. no. 5-7, pp. 211–357. 1988. DOI: `10.1016/0167-5729(88)90011-8`.

[26] M. Czerny and A. F. Turner. "Über den Astigmatismus bei Spiegelspektrometern". *Zeitschrift für Physik.* vol. 61. no. 11-12, pp. 792–797. 1930. DOI: `10.1007/BF01340206`.

[27] R. G. Gould et al. "The laser, light amplification by stimulated emission of radiation". in *The Ann Arbor conference on optical pumping, the University of Michigan.* vol. 15. 1959, p. 92.

[28] A. E. Siegman. *Lasers. Hardcover.* Revised ed. Sausalito, California: University Science Books, 1986.

[29] M. Endo and R. F. Walter. *Gas Lasers.* 1st Edition. Boca Raton: CRC Press, 2007.

[30] R. W. F. Gross and J. F. Bott. *Handbook of Chemical Lasers. Paperback.* First Edition. New York: John Wiley & Sons, 1976.

[31] C. K. Rhodes. *Excimer Lasers.* 1st ed. Berlin: Springer, 1979.

[32] D. J. Richardson, J. Nilsson, and W. A. Clarkson. "High power fiber lasers: Current status and future perspectives". *J. Opt. Soc. Am. B.* vol. 27. no. 11, B63–B92. 2010. DOI: `10.1364/JOSAB.27.000B63`.

[33] F. P. Schäfer. *Dye Lasers.* 1st ed. Berlin: Springer, 1973.

[34] D. A. G. Deacon, L. R. Elias, J. M. J. Madey, G. J. Ramian, H. A. Schwettman, and T. I. Smith. "First operation of a free-electron laser". *Phys. Rev. Lett..* vol. 38, pp. 892–894. 16 1977. DOI: `10.1103/PhysRevLett.38.892`.

[35] M. Asada, Y. Miyamoto, and Y. Suematsu. "Gain and the threshold of three-dimensional quantum-box lasers". *IEEE Journal of Quantum Electronics.* vol. 22. no. 9, pp. 1915–1921. 1986. DOI: `10.1109/JQE.1986.1073149`.

[36] D. J. Jones, S. A. Diddams, J. K. Ranka, A. Stentz, and Windeler. "Carrier-envelope phase control of femtosecond mode-locked lasers and direct optical frequency synthesis". *Science.* vol. 288. no. 5466, pp. 635–639. 2000. DOI: `10.1126/science.288.5466.635`.

[37] W. Koechner and M. Bass. *Solid-State Lasers. A Graduate Text.* 1st ed. New York: Springer, 2006.

[38] D. T. Reid, M. Padgett, C. McGowan, W. E. Sleat, and W. Sibbett. "Light-emitting diodes as measurement devices for femtosecond laser pulses". *Optics Letters.* vol. 22. no. 4, pp. 233–235. 1997. DOI: `10.1364/OL.22.000233`.

[39] J. Toporski, T. Dieing, and O. Hollricher. *Confocal Raman Microscopy.* 2nd ed. Germany: Springer, 2018. DOI: `10.1007/978-3-319-75380-5`.

[40] P. Pelikán, M. Ceppan, and M. Liška. *Applications of Numerical Methods in Molecular Spectroscopy. Fundamental & Applied Aspects of Chemometrics.* 1st Edition. Florida: CRC Press, 1994.

[41] Z. Fu, X. Zhang, H. Zhang, Y. Li, H. Zhou, and Y. Zhang. "On the understandings of dielectric constant and its impacts on the photovoltaic efficiency in organic solar cells". *Chinese Journal of Chemistry*. vol. 39. no. 2, pp. 381–390. 2021. DOI: `10.1002/cjoc.202000289`.

[42] D. M. Stoltzfus, J. E. Donaghey, A. Armin, P. E. Shaw, P. L. Burn, and P. Meredith. "Charge generation pathways in organic solar cells: Assessing the contribution from the electron acceptor". *Chemical Reviews*. vol. 116. no. 21, pp. 12 920–12 955. 2016. DOI: `10.1021/acs.chemrev.6b00126`.

[43] D. B. Riley, P. Meredith, A. Armin, and O. J. Sandberg. "Role of exciton diffusion and lifetime in organic solar cells with a low energy offset". *The Journal of Physical Chemistry Letters*. vol. 13. no. 20, pp. 4402–4409. 2022. DOI: `10.1021/acs.jpclett.2c00791`.

[44] R. Rennie and J. Law. *A Dictionary of Physics. Oxford Quick Reference*. 8th Edition. Oxford: Oxford University Press, 2019.

[45] R. Datta, T. M. Heaster, J. T. Sharick, A. A. Gillette, and M. C. Skala. "Fluorescence lifetime imaging microscopy: Fundamentals and advances in instrumentation, analysis, and applications. Fundamentals and advances in instrumentation, analysis, and applications". *Journal of Biomedical Optics*. vol. 25. no. 07, pp. 10–40. 2020. DOI: `10.1117/1.JBO.25.7.071203`.

[46] M. D. Levenson and S. S. Kano. *Introduction to Nonlinear Laser Spectroscopy. Optics & Photonics Series*. Hardcover. Portland: Academic Press Inc, 1989.

[47] W. Becker. *The bh TCSPC handbook*. 9th edition. Germany: Becker & Hickl GmbH, 2021.

[48] J. Ryu et al. "Real-time visualization of two-photon fluorescence lifetime imaging microscopy using a wavelength-tunable femtosecond pulsed laser". *Biomedical Optics Express*. vol. 9. no. 7. 2018. DOI: `10.1364/BOE.9.003449`.

[49] P. Wang, J. Liang, and L. V. Wang. "Single-shot ultrafast imaging attaining 70 trillion frames per second". *Nature Communications*. vol. 11. no. 1. 2020. DOI: `10.1038/s41467-020-15745-4`.

[50] X. Liu et al. "Fast fluorescence lifetime imaging techniques. A review on challenge and development". *Journal of Innovative Optical Health Sciences*. vol. 12. no. 05. 2019. DOI: `10.1142/S1793545819300039`.

[51] J. B. Pawley. *Handbook of Biological Confocal Microscopy. Foundations of Confocal Scanned Imaging in Light Microscopy*. 3rd ed. Berlin: Springer, 2006. DOI: `10.1007/978-0-387-45524-2_1`.

[52] S. Cacovich et al. "Imaging and quantifying non-radiative losses at 23% efficient inverted perovskite solar cells interfaces". *Nature Communications*. vol. 13. no. 1, p. 2868. 2022. DOI: `10.1038/s41467-022-30426-0`.

[53] T. Bu et al. "Modulating crystal growth of formamidinium–caesium perovskites for over 200 cm^2 photovoltaic sub-modules". *Nature Energy*. vol. 7. no. 6, pp. 528–536. 2022. DOI: `10.1038/s41560-022-01039-0`.

[54] Y. Sun et al. "Bright and stable perovskite light-emitting diodes in the near-infrared range". *Nature*. vol. 615. no. 7954, pp. 830–835. 2023. DOI: `10.1038/s41586-023-05792-4`.

[55] N. Li et al. "Liquid medium annealing for fabricating durable perovskite solar cells with improved reproducibility". *Science*. vol. 373. no. 6554, pp. 561–567. 2021. DOI: `10.1126/science.abh3884`.

[56] M. Born and E. Wolf. *Principles of optics: Electromagnetic theory of propagation, interference and diffraction of light*. 7th Edition. Amsterdam, Netherlands: Elsevier, 1999. DOI: `10.1017/CBO9781139644181`.

[57] E. Synge. "Xxxviii. a suggested method for extending microscopic resolution into the ultra-microscopic region". *The London, Edinburgh, and Dublin Philosophical Magazine and Journal of Science*. vol. 6. no. 35, pp. 356–362. 1928. DOI: `10.1080/14786440808564615`.

[58] A. Lewis, M. Isaacson, A. Harootunian, and A. Muray. "Development of a 500 Å spatial resolution light microscope". *Ultramicroscopy*. vol. 13. no. 3, pp. 227–231. 1984. DOI: 10.1016/0304-3991(84)90201-8.

[59] D. W. Pohl, W. Denk, and M. Lanz. "Optical stethoscopy. Image recording with resolution $\lambda/20$". *Applied Physics Letters*. vol. 44. no. 7, pp. 651–653. 1984. DOI: 10.1063/1.94865.

[60] E. Betzig, J. K. Trautman, T. D. Harris, J. S. Weiner, and R. L. Kostelak. "Breaking the diffraction barrier. Optical microscopy on a nanometric scale". *Science*. vol. 251. no. 5000, pp. 1468–1470. 1991. DOI: 10.1126/science.251.5000.1468.

[61] D. A. Higgins, P. J. Reid, and P. F. Barbara. "Structure and exciton dynamics in J-aggregates studied by polarization-dependent near-field scanning optical microscopy". *The Journal of Physical Chemistry*. vol. 100. no. 4, pp. 1174–1180. 1996. DOI: 10.1021/jp9518217.

[62] K.-D. Park et al. "Near-field imaging of cell membranes in liquid enabled by active scanning probe mechanical resonance control". *The Journal of Physical Chemistry C*. vol. 120. no. 37, pp. 21 138–21 144. 2016. DOI: 10.1021/acs.jpcc.6b06563.

[63] J. M. Atkin, S. Berweger, A. C. Jones, and M. B. Raschke. "Nano-optical imaging and spectroscopy of order, phases, and domains in complex solids". *Advances in Physics*. vol. 61. no. 6, pp. 745–842. 2012. DOI: 10.1080/00018732.2012.737982.

[64] H. A. Bethe. "Theory of diffraction by small holes". *Physical Review*. vol. 66. no. 7-8, pp. 163–182. 1944. DOI: 10.1103/PhysRev.66.163.

[65] Y. Inouye and S. Kawata. "Near-field scanning optical microscope with a metallic probe tip". *Optics Letters*. vol. 19. no. 3, pp. 159–161. 1994. DOI: 10.1364/OL.19.000159.

[66] Z. Zhang, S. Sheng, R. Wang, and M. Sun. "Tip-enhanced Raman spectroscopy". *Analytical Chemistry*. vol. 88. no. 19, pp. 9328–9346. 2016. DOI: 10.1021/acs.analchem.6b02093.

[67] W. Su, N. Kumar, S. Mignuzzi, J. Crain, and D. Roy. "Nanoscale mapping of excitonic processes in single-layer MoS_2 using tip-enhanced photoluminescence microscopy". *Nanoscale*. vol. 8. no. 20, pp. 10 564–10 569. 2016. DOI: 10.1039/C5NR07378B.

[68] K.-D. Park et al. "Tip-enhanced strong coupling spectroscopy, imaging, and control of a single quantum emitter". *Science Advances*. vol. 5. no. 7. 2019. DOI: 10.1126/sciadv.aav5931.

[69] H. Lee, D. Y. Lee, M. G. Kang, Y. Koo, T. Kim, and K.-D. Park. "Tip-enhanced photoluminescence nano-spectroscopy and nano-imaging". *Nanophotonics*. vol. 9. no. 10, pp. 3089–3110. 2020. DOI: 10.1515/nanoph-2020-0079.

[70] L. Novotny and B. Hecht. *Principles of nano-optics*. 2nd ed. Cambridge: Cambridge University Press, 2012.

[71] B. Hecht et al. "Scanning near-field optical microscopy with aperture probes. Fundamentals and applications". *The Journal of Chemical Physics*. vol. 112. no. 18, pp. 7761–7774. 2000. DOI: 10.1063/1.481382.

[72] "MF002". (2023). [Online]. Available: https://tipsnano.com/catalog/snom/snom-fiber-probes/mf002/.

[73] L. Novotny and C. Hafner. "Light propagation in a cylindrical waveguide with a complex, metallic, dielectric function". *Physical Review E*. vol. 50. no. 5, pp. 4094–4106. 1994. DOI: 10.1103/PhysRevE.50.4094.

[74] M. D. Serio, H. Mohapatra, R. Zenobi, and V. Deckert. "Investigation of the liquid–liquid interface with high spatial resolution using near-field Raman spectroscopy". *Chemical Physics Letters*. vol. 417. no. 4-6, pp. 452–456. 2006. DOI: 10.1016/j.cplett.2005.10.082.

[75]   R. Zenobi and V. Deckert. "Scanning near-field optical microscopy and spectroscopy as a tool for chemical analysis". *Angewandte Chemie International Edition*. vol. 39. no. 10, pp. 1746–1756. 2000. DOI: `10.1002/(SICI)1521-3773(20000515)39:10<1746::AID-ANIE1746>3.0.CO;2-Q`.

[76]   W. Zhang, Z. Fang, and X. Zhu. "Near-field Raman spectroscopy with aperture tips". *Chemical Reviews*. vol. 117. no. 7, pp. 5095–5109. 2017. DOI: `10.1021/acs.chemrev.6b00337`.

[77]   B. N. Tugchin et al. "Quasi-linearly polarized hybrid modes in tapered and metal-coated tips with circular apertures. Understanding the functionality of aperture tips". *New Journal of Physics*. vol. 19. no. 6. 2017. DOI: `10.1088/1367-2630/aa6feb`.

[78]   S. Haxha, F. AbdelMalek, F. Ouerghi, M. D. B. Charlton, A. Aggoun, and X. Fang. "Metamaterial superlenses operating at visible wavelength for imaging applications". *Scientific Reports*. vol. 8. no. 1. 2018. DOI: `10.1038/s41598-018-33572-y`.

[79]   Y. Lee, S. Park, H. Kim, G. H. Han, Y. H. Lee, and J. Kim. "Characterization of the structural defects in cvd-grown monolayered mMoS$_2$ using near-field photoluminescence imaging". *Nanoscale*. vol. 7. no. 28, pp. 11 909–11 914. 2015. DOI: `10.1039/C5NR02897C`.

[80]   W. Bao et al. "Mapping local charge recombination heterogeneity by multidimensional nanospectroscopic imaging". *Science*. vol. 338. no. 6112, pp. 1317–1321. 2012. DOI: `10.1126/science.1227977`.

[81]   B. G. Yacobi and D. B. Holt. *Cathodoluminescence Microscopy of Inorganic Solids*. 1990th Edition. New York: Springer, 1990.

[82]   N. Yamamoto, S. Bhunia, and Y. Watanabe. "Polarized cathodoluminescence study of inp nanowires by transmission electron microscopy". *Applied Physics Letters*. vol. 88. no. 15. 2006. DOI: `10.1063/1.2168043`.

[83]   "PILAS – picosecond pulsed diode lasers". (2023). [Online]. Available: `https://www.nktphotonics.com/products/pulsed-diode-lasers/pilas/`.

[84]   "Chameleon Ti:Sapphire". (2023). [Online]. Available: `https://www.coherent.com/lasers/oscillators/chameleon-ultra`.

[85]   "Shamrock 303i". (2016). [Online]. Available: `https://andor.oxinst.com/downloads/uploads/Andor_Shamrock-303_Manual.pdf`.

[86]   "iDus 420 CCD". (2023). [Online]. Available: `https://andor.oxinst.com/products/idus-spectroscopy-cameras/idus-420`.

[87]   "SPCM-AQRH". (2023). [Online]. Available: `https://www.excelitas.com/product/spcm-aqrh`.

[88]   "Time Tagger Series". (2023). [Online]. Available: `https://www.swabianinstruments.com/time-tagger/`.

[89]   M. V. Kovalenko, L. Protesescu, and M. I. Bodnarchuk. "Properties and potential optoelectronic applications of lead halide perovskite nanocrystals". *Science*. vol. 358. no. 6364, pp. 745–750. 2017. DOI: `10.1126/science.aam7093`.

[90]   "LiteScope AFM-in-SEM". (2023). [Online]. Available: `https://www.nenovision.com/products/litescope-afm-in-sem`.

[91]   W. Dong et al. "Wide bandgap phase change material tuned visible photonics". *Advanced Functional Materials*. vol. 29. no. 6. 2019. DOI: `10.1002/adfm.201806181`.

[92]   Y. Gutiérrez et al. "Interlaboratory study on sb2s3 interplay between structure, dielectric function, and amorphous-to-crystalline phase change for photonics". *IScience*. vol. 25. no. 6. 2022. DOI: `10.1016/j.isci.2022.104377`.

[93] "UHU super glue". (2023). [Online]. Available: https://www.uhu.cz/uhu-super-glue-minis-3-x-1-g.html.

[94] "460HP - single mode optical fiber". (2023). [Online]. Available: https://www.thorlabs.com/thorproduct.cfm?partnumber=460HP.

[95] "S425C". (2023). [Online]. Available: https://www.thorlabs.com/thorproduct.cfm?partnumber=S425C.

[96] "S120VC". (2023). [Online]. Available: https://www.thorlabs.com/thorproduct.cfm?partnumber=S120VC.

[97] "SHG Crystals". (2023). [Online]. Available: https://covesion.com/en/products/mgoppln-crystals-and-chips/shg-crystals/.

[98] M. Shahidani, S. G. Sabouri, and A. Khorsandi. "Oven segmentation scheme for pulse shape and efficiency improvement in a picosecond second harmonic generation". *Applied Physics B*. vol. 127. no. 9. 2021. DOI: 10.1007/s00340-021-07674-x.

[99] S. Farina et al. "Above pile-up fluorescence microscopy with a 32 Mc/s single-channel time-resolved SPAD system". *Optics Letters*. vol. 47. no. 1, pp. 82–85. 2022. DOI: 10.1364/OL.444815.

[100] J. E. Sorrells et al. "Computational photon counting using multithreshold peak detection for fast fluorescence lifetime imaging microscopy". *ACS Photonics*. vol. 9. no. 8, pp. 2748–2755. 2022. DOI: 10.1021/acsphotonics.2c00505.

[101] "Gwyddion". (2023). [Online]. Available: http://gwyddion.net/.

[102] "OriginLab". (2023). [Online]. Available: https://www.originlab.com/.

[103] A. S. R. Bati, Y. L. Zhong, P. L. Burn, M. K. Nazeeruddin, P. E. Shaw, and M. Batmunkh. "Next-generation applications for integrated perovskite solar cells". *Communications Materials*. vol. 4. no. 1. 2023. DOI: 10.1038/s43246-022-00325-4.

[104] R. Wang, T. Huang, J. Xue, J. Tong, K. Zhu, and Y. Yang. "Prospects for metal halide perovskite-based tandem solar cells". *Nature Photonics*. vol. 15. no. 6, pp. 411–425. 2021. DOI: 10.1038/s41566-021-00809-8.

[105] Q. A. Akkerman, G. Rainò, M. V. Kovalenko, and L. Manna. "Genesis, challenges and opportunities for colloidal lead halide perovskite nanocrystals". *Nature Materials*. vol. 17. no. 5, pp. 394–405. 2018. DOI: 10.1038/s41563-018-0018-4.

[106] S. T. Williams, F. Zuo, C.-C. Chueh, C.-Y. Liao, P.-W. Liang, and A. K.-Y. Jen. "Role of chloride in the morphological evolution of organo-lead halide perovskite thin films". *ACS Nano*. vol. 8. no. 10, pp. 10 640–10 654. 2014. DOI: 10.1021/nn5041922.

[107] J. H. Noh, S. H. Im, J. H. Heo, T. N. Mandal, and S. I. Seok. "Chemical management for colorful, efficient, and stable inorganic–organic hybrid nanostructured solar cells". *Nano Letters*. vol. 13. no. 4, pp. 1764–1769. 2013. DOI: 10.1021/nl400349b.

[108] M. Vrućinić et al. "Local versus long-range diffusion effects of photoexcited states on radiative recombination in organic–inorganic lead halide perovskites". *Advanced Science*. vol. 2. no. 9. 2015. DOI: 10.1002/advs.201500136.

[109] F. Ricci et al. "Enhanced exciton quantum coherence in single $CsPbBr_3$ perovskite quantum dots using femtosecond two-photon near-field scanning optical microscopy". *ACS Nano*. vol. 15. no. 8, pp. 12 955–12 965. 2021. DOI: 10.1021/acsnano.1c01615.

[110] L. A. Muscarella et al. "Crystal orientation and grain size. Do they determine optoelectronic properties of $MAPbI_3$ perovskite?" *The Journal of Physical Chemistry Letters*. vol. 10. no. 20, pp. 6010–6018. 2019. DOI: 10.1021/acs.jpclett.9b02757.

[111] D. W. deQuilettes et al. "Charge-carrier recombination in halide perovskites". *Chemical Reviews*. vol. 119. no. 20, pp. 11 007–11 019. 2019. DOI: 10.1021/acs.chemrev.9b00169.

[112] Y. Tong et al. "Spontaneous self-assembly of perovskite nanocrystals into electronically coupled supercrystals. Toward filling the green gap". *Advanced Materials*. vol. 30. no. 29. 2018. DOI: 10.1002/adma.201801117.

[113] E. V. Péan, S. Dimitrov, C. S. D. Castro, and M. L. Davies. "Interpreting time-resolved photoluminescence of perovskite materials". *Physical Chemistry Chemical Physics*. vol. 22. no. 48, pp. 28 345–28 358. 2020. DOI: 10.1039/D0CP04950F.

[114] J. Jiang et al. "Carrier lifetime enhancement in halide perovskite via remote epitaxy". *Nature Communications*. vol. 10. no. 1. 2019. DOI: 10.1038/s41467-019-12056-1.

[115] P. Strak et al. "Instantaneous decay rate analysis of time resolved photoluminescence (TRPL): Application to nitrides and nitride structures". *Journal of Alloys and Compounds*. vol. 823. 2020. DOI: 10.1016/j.jallcom.2020.153791.

[116] D. Zhang et al. "Reconstructing local profile of exciton–emission wavelengths across a WS_2 bubble beyond the diffraction limit". *ACS Nano*. vol. 14. no. 6, pp. 6931–6937. 2020. DOI: 10.1021/acsnano.0c01337.

[117] S. Meuret et al. "Lifetime measurements well below the optical diffraction limit". *ACS Photonics*. vol. 3. no. 7, pp. 1157–1163. 2016. DOI: 10.1021/acsphotonics.6b00212.

Symbols and abbreviations

NF   Near-field

PL   Photoluminescence

TRPL   Time-resolved photoluminescence

ERASMUS   European community action scheme for the mobility of university students

a-SNOM   Aperture-type scanning near-field optical microscopy

IPE   Institute of Physical Engineering

HOMO   Highest occupied molecular orbital

LUMO   Lowest unoccupied molecular orbital

LED   Light emitting diode

SHG   Second harmonic generation

SFG   Sum frequency generation

DFG   Difference frequency generation

QPM   Quasi-phase matching

BBO   Beta-barium borate

LBO   Lithium triborate

LN   Lithium niobate

KTP   Potassium titanyl phosphate

PPLN   Periodically poled lithium niobate

PPKTP   Periodically poled potassium titanyl phosphate

S Singlet

T Triplet

SNOM   Scanning near-field optical microscopy

CCD   Charge-coupled device

Ti:Sa   Titanium:Sapphire

CW   Continuous wave

FWHM	Full width at half-maximum
WSe$_2$	Tungsten diselenide
G-L	Gaussian-Lorentzian
CT	Charge-transfer
TCSPC	Time-correlated single photon counting
FLIM	Fluorescence lifetime imaging
LSM	Laser scanning microscopy
WFI	Wide-field illumination
TAC	Time-amplitude converter
SNR	Signal-to-noise ratio
Cl-PEAI	4-chlorophenylethylammonium iodide
F-PEAI	4-fluoro-phenylethylammonium iodide
HTL	Hole transport layer
ETL	Electron transport layer
MACl	Methylammonium chloride
PbI$_2$	Lead iodide
SEM	Scanning electron microscope
DABr	Dodecylamine hydrobromide
MSPE	2-(4-(methyl-sulfonyl)phenyl)ethylamine
FAPbI$_3$	Formamidinium lead triiodide
LMA	Liquid medium annealing
PSCs	Perovskite solar cells
PCE	Power conversion efficiency
NFOM	Near-field optical microscopy
s-SNOM	scattering-type scanning near-field optical microscopy
TERS	Tip-enhanced Raman spectroscopy

TEPL	Tip-enhanced photoluminescence
TESC	Tip-enhanced strong coupling
AFM	Atomic force microscopy
MoS$_2$	molybdenum disulfide
InP NWs	Indium phosphide nanowires
TTL	Transistor-transistor logic
Sb$_2$S$_3$	Antimony trisulfide
BUT	Brno University of Technology
CEITEC	Central European Institute of Technology
GUI	Graphical user interface
NRcoeff	Noise-reduction coefficient
PCPcoeff	Peak center position
CtsMinLv	Counts minimal level
MAPbI$_3$	Methylammonium lead iodide
CsPbBr$_3$	Cesium lead bromide